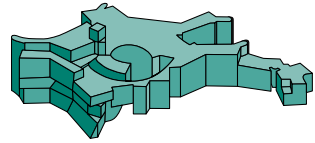




Technische Universität München



Max-Planck-Institut für Astrophysik

Gravitational waves from core-collapse supernovae

Haakon Andresen

Vollständiger Abdruck der von der Fakultät für Physik der Technischen Universität München
zur Erlangung des akademischen Grades eines

Doktors der Naturwissenschaften (Dr. rer. nat.)

genehmigten Dissertation.

Vorsitzender: Univ.-Prof. Dr.

Prüfer der Dissertation: 1. Priv.-Doz.

2. Univ.-Prof.

3. Univ.-Prof.

Die Dissertation wurde am xx.xx.2017 bei der Technischen Universität München eingereicht
und durch die Fakultät für Physik am xx.xx.2017 angenommen.

Contents

1 Supernovae	1
1.1 Classifying supernovae	1
1.2 Iron-core supernovae	2
1.2.1 Shell burning in massive stars	2
1.2.2 Iron-core collapse	3
1.2.3 Shock revival: the neutrino heating mechanism	4
1.3 The post-bounce phase	5
1.3.1 The gain layer, cooling layer and the three layers of the Proto-neutron star	5
1.3.2 The standing accretion shock instability	6
1.4 Three-dimensional simulations	7
2 Theory	9
2.1 Linearised theory	9
2.2 The transverse-traceless gauge	10
2.3 Generation of gravitational waves	12
3 Numerical simulations of core-collapse supernovae	19
3.1 PROMETHEUS	19
3.1.1 Hydrodynamics	20
3.1.2 Equation of state	21
3.1.3 Self gravity - the effective potential	21
3.2 VERTEX	21
3.3 Grid setup	23
3.3.1 Spherical polar grid	23
3.3.2 Yin-Yang grid	24
4 Signal analysis	25
4.1 Fourier analysis	25
4.1.1 Continuous and discrete Fourier transforms	25
4.2 The short-time Fourier transform	26
4.3 The Nyquist frequency and aliasing	26
4.4 The spectral energy density of a discrete time signal	27

5 First paper	29
5.1 Introduction	29
5.2 Setup and Numerical Methods	32
5.2.1 Numerical Methods	32
5.3 Structure and Origin of the Gravitational Wave Signal	33
5.3.1 Supernova Models	33
5.3.2 Gravitational Wave Extraction	36
5.3.3 Overview of Waveforms	36
5.3.4 Spatial Location of Underlying Hydrodynamical Instabilities	40
5.3.5 Origin of High-Frequency Emission	44
5.3.6 Comparison of high-frequency emission in 2D and 3D	46
5.3.7 Origin of the Low-Frequency Signal	50
5.3.8 Comparison of the exploding and non-exploding 20 solar mass models	55
5.4 Detection Prospects	57
5.4.1 General Considerations	57
5.4.2 Detection Prospects for Simulated Models	59
5.4.3 Detection Prospects with AdvLIGO	60
5.4.4 Detection Prospects with the Einstein Telescope	60
5.4.5 Interpretation of a Prospective Detection	61
5.5 Conclusions	61
6 The effects of rotation	67
6.1 Supernova Models	67
6.2 Results	72
6.2.1 Qualitative description of the gravitational wave signals	72
6.3 Excitation of gravitational waves	76
6.4 The standing accretion shock instability, rotation, and resolution	78
6.5 Detection prospects	79
6.6 Conclusion and discussion	80
Bibliography	83

1 Supernovae

The history of supernovae starts, as most astrophysical objects, with observations of strong electromagnetic events in the night sky. Supernovae are some of the most energetic events known to astronomers and throughout history, some have been clearly visible by naked eye from earth and could be seen even during the day (see Hamacher (2014) and references therein). The Crab supernova was in 1054 described by Chinese astronomers (Ho, 1962, Shen, 1969).

... it was visible by day, like Venus; pointed rays shot out from it on all sides; the color was reddish-white. Altogether it was visible for 23 days.

1.1 Classifying supernovae

In the modern era observations of supernovae continually improved. In 1941 German-American astronomer Rudolph Minkowski (Minkowski, 1941) found that not all supernovae show hydrogen lines in their spectra and he consequently divided supernovae into two types based on the presence of hydrogen (Type II) or lack of hydrogen lines (Type I). Later it was recognized that there were variations within these two classes and a set of subclasses, based on variation in the spectra and light curve. Type I supernovae were divided into type Ia, Ib, and Ic, where the nebular spectrum of types Ib and Ic was found to be similar to those of type II supernovae. Two examples of the type II sub-classes are types II-L and II-P. After reaching the maximum luminosity, the light curves of type II-P supernovae settles onto a plateau and their luminosity reminds almost constant for several months. The luminosity of Type II-L, on the other hand, decline almost linearly. For a detailed review of the classification system see Cappellaro & Turatto (2001).

The similarities between the nebular spectra of type II and type Ib/c supernovae already hints at a similar explosion mechanism. From a theoretical standpoint, one might say that a classification based on physical processes powering the supernovae is more prudent. Already in 1960 Hoyle & Fowler (1960) suggested that type II supernovae result from the implosion of stellar cores and that type I is produced by igniting degenerate stellar material. Today it is understood that that type Ia supernovae result from the thermonuclear explosions of white dwarfs. In other words, the ignition of degenerate stellar material. Furthermore, we now know that type II and type Ib/c supernovae are the result of the

gravitational collapse, the implosion, of stellar cores. The latter category are known as core-collapse supernovae. The subject of this thesis is the gravitational waves generated during the collapse and subsequent explosion of a specific sub-type of core-collapse supernova, the “Iron-core supernova”, and we, therefore, constrain our attention to this class of supernovae. The interested reader is referred to Janka (2012) for a comprehensive description of the possible explosion mechanisms.

1.2 Iron-core supernovae

1.2.1 Shell burning in massive stars

When a massive star nears the end of its life it has depleted most of the hydrogen in the central core and hydrogen burning ceases and the gravitational pull is no longer balanced by thermal and radiation pressure resulting from nuclear fusion. The consequence is that the core starts to contract, the contraction is eventually halted when the pressure and temperature in the core become large enough for helium burning to set in. The layer right outside of the helium burning core is still rich in hydrogen and so hydrogen burning develops in a layer around the core. The burning of helium in the core stabilises the star, for a while. However, the helium fuel eventually runs out and the process repeats itself, only this time the contraction continues until carbon ignites in the inner core.

The process of burning heavier and heavier elements in the core continues up to silicon. The end product of silicon burning is iron-group elements and since nuclear fusion of iron-group elements does not release any energy the cycle stops at silicon. The end result of this process is an onion like shell structure consisting of consecutive layers burning heavier and heavier elements. In the centre of this onion is ever growing core consisting of iron and nickel (henceforth referred to as the “iron-core”), it grows due to the ashes produced by the continued burning

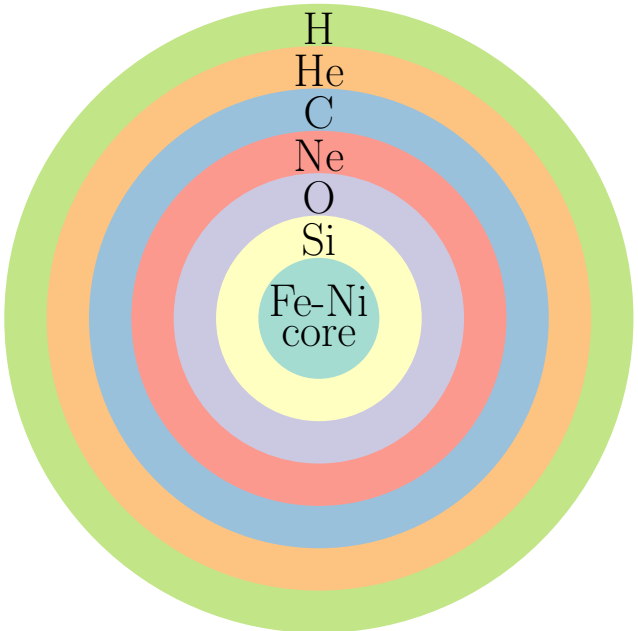


Figure 1.1: Schematic representation of the shell structure of a massive star right before the onset of core-collapse. The stellar core consists of consecutive layers burning heavier and heavier elements and an inner iron-nickel core.

of silicon in the layer above. A depiction of this shell structure can be seen in Fig. 1.1. The star remains in this state for a while, until the central iron-core has accumulated so much matter that its mass exceeds the Chandrasekhar mass and the inevitable gravitational collapse of the core begins.

1.2.2 Iron-core collapse

The collapse of the iron-core is triggered and accelerated by two processes. Firstly, rising temperatures increase the rate of photo-dissociation of iron-group nuclei. The nuclei are converted into free nucleons and alpha particles, which is a process that consumes thermal energy. Secondly, as the core density increases electron capture on heavy nuclei becomes more frequent. Free electrons are captured by protons in the nuclei and a neutrons and anti-electron neutrinos are produced:

$$p + e^- \rightarrow n + \bar{\nu}_e, \quad (1.1)$$

where p^+ , e^- , n and $\bar{\nu}_e$ represents a proton, an electron, a neutron and an anti-electron neutrino, respectively. The neutrinos escape the core and in the process carry with them energy and lepton number. Before the onset of collapse it was pressure from degenerate electrons that was supporting the core. When the lepton number decreases the pressure also decreases, and this leads to an acceleration of the collapse. Effectively what is happening is that the Chandrasekhar mass of the core is reduced.

The rapid deleptonisation of the iron-core eventually slows down and virtually stops for the duration of the collapse. At densities around 10^{12} g/cm^3 the mean free path of the neutrinos become so short that the time they need to diffuse out of the core is larger than the time-scale of the collapse. The iron-core, therefore, from this point on collapses in an adiabatic and homologous manner. The collapse continues until the central iron-core reaches nuclear densities, around $2.7 \times 10^{14} \text{ g/cm}^3$, at this point the repulsive forces between nuclei leads to a sudden stiffening of the equation of state (EoS) and the collapse of the inner iron-core comes to an abrupt halt.

However, due to its high inertia the inner core contracts beyond the equilibrium point of the gravitational pull and the new source of pressure. This leads to a recoil and as the inner region of the iron-core expands outwards it crashes into the infalling material above it. This event is the so-called core bounce and it launches a sound wave into the outer iron-core, that steepens into a shock wave when it reaches the supersonically infalling layers of the outer core.

As the shock propagates outwards through the dense stellar material it loses about 10^{51} erg of energy per $0.1 M_\odot$ of iron-core material that falls through the shock front, due to the dissociation of heavy nuclei into free nucleons. Eventually, the density ahead of the shock drops below $\sim 10^{11} \text{ g/cm}^3$ and the neutrinos behind the shock can suddenly escape. This

leads to a burst of neutrino emission and a significant loss of energy for the shock. After a few milliseconds (ms) the shock has lost so much energy that it stalls at a radius between 100 and 200 km and turns into an accretion shock.

1.2.3 Shock revival: the neutrino heating mechanism

It was initially thought that the shock would not stall, but rather propagate throughout the mantle of the star and disrupt it in the process. This mechanism is known as the bounce-shock or prompt-shock mechanism. As mentioned above, the shock only propagates outwards for a few ms before losing most of its energy and stagnating. The failure of the bounce-shock mechanism can be viewed as a consequence of its failure to account for anything else than purely hydrodynamical effects. Most of the gravitational binding energy released during the collapse is stored in the form of trapped neutrinos and tapping into this energy reservoir might provide the energy needed to revive the stalled shock. Already in 1966 Colgate & White (1966) proposed that neutrinos could be the principle actor in the drama unfolding deep within the star. Later this idea was revisited and expanded upon by Wilson (1985) who formulated the so-called “delayed neutrino-driven explosion mechanism”.

At the same time as the shock is initially launched a hot proto-neutron star (PNS) forms in the center of the star. The gravitational binding energy released during the collapse is converted into thermal energy. The PNS mainly cools through emission of neutrinos, which first slowly diffuse through the optically thick inner-core before breaking out of the so-called neutrinosphere and streaming away from the core. The neutrinosphere is defined by the radius where the core becomes optically thin to neutrinos. A secondary source of neutrinos is the matter falling through the stalled shock and accreting onto the PNS, which releases neutrinos as the material settles onto the PNS. The capture of electrons and positrons on free nuclei is the main source of neutrinos in the hot accretion layer around the PNS. This means that electron and anti-electron neutrinos make up a large fraction of the neutrino emission generated by PNS accretion.

The material falling through the shock also exerts the ram pressure that must somehow be counteracted to relaunch the shock. As neutrinos stream away from the core a small fraction of their energy is deposited into the stellar material behind the shock, because this material is not perfectly optically thin to neutrinos. It is this energy deposition that is thought to balance and eventually overcome the ram pressure of the infalling of the material, leading to the successful revival of the stalled shock.

1.3 The post-bounce phase

The phase between core bounce and shock revival is a crucial time period for the delayed neutrino-driven explosion mechanism. The focus of this thesis is to study what we can learn about core collapse supernovae by observing the gravitational wave (GW) signal they produce. Specifically this work focuses on fingerprints of hydrodynamical processes operating during the post-bounce phase. In this section we discuss our current understanding of the properties of the region behind the stalled shock front, consisting of the PNS and the region between the PNS and the shock front (known as the post-shock volume/region/layer).

1.3.1 The gain layer, cooling layer and the three layers of the Proto-neutron star

The fact that the mean free path of the neutrinos increases with radius means that neutrino diffusion more effectively carries away lepton number and entropy in the outer regions of the PNS core. This leads to the establishment of negative entropy and composition gradients, which in turn creates a convectively unstable region located between the surface and the inner PNS core (see Fig. 1.2).

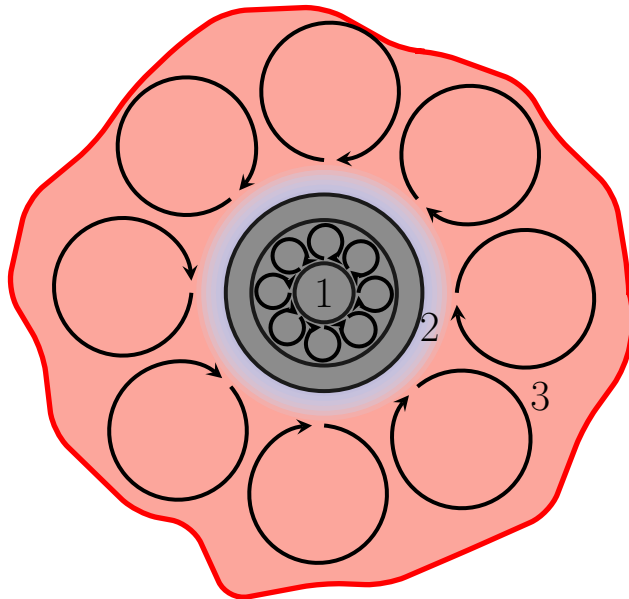
The heating of the stellar material in the post-shock region is dominated by charged-current reactions



and cooling by the corresponding inverse interactions



The neutrino-cooling rate, caused by the reactions described by Eq. 1.3, depends on the temperature to the sixth power, $\sim T^6$. Since the temperature of the convectively mixed post-shock layer drops roughly as $\sim 1/r$ (Janka, 2012) the cooling efficiency drops as $\sim r^{-6}$. The heating rate, on the other hand, drops off only as radius squared, $\sim r^{-2}$. As a result, there exists a radius where heating and cooling effects balance each other. This radius is called the “gain radius”. Below the gain radius neutrino cooling dominates and above there is a net heating by neutrinos. The neutrino heating from below makes the gain layer unstable to large scale convective activity. The high-entropy bubbles that are created by convection in pushes shock front outwards. This prolongs the time it takes for stellar matter to be advected through the layer, which enhances the heating done by neutrinos. Convection also transports heated material away from the gain radius and prevents it from falling down into the cooling layer. The end result is that the matter



1: Proto-neutron star. 2: Cooling layer. 3: Gain layer.

Figure 1.2: Schematic representation of the region behind the shock. The grey region indicates the PNS, the light blue region shows the cooling layer and the gain layer is indicated by the light red region. The dark red boundary shows the shock front with its large and small scale deformations. Circular arrows indicate the two regions that are convectively active.

falling through the shock spends considerably more time in the gain layer than it would without the development of convection. This favours the delayed neutrino-driven explosion mechanism and has been studied by several authors (see for example Herant et al. (1994), Burrows et al. (1995), Janka & Müller (1996), Foglizzo et al. (2006), Müller et al. (2012b)). In Fig. 1.2 we see a schematic depiction, not to scale, of the region behind the stalled shock. The PNS is indicated by the grey region, the cooling layer by the light blue and the light red region indicates the gain layer. The circles with arrows indicate convection. The dark red curve at the edge of the gain layer indicates the shock front, with its large and small scale deformations.

1.3.2 The standing accretion shock instability

Another instability that can develop and be beneficial for the explosion mechanism is the so-called standing accretion shock instability (SASI), which manifests itself in large-scale sloshing and spiral motions of the shock (Blondin et al., 2003, Blondin & Mezzacappa, 2006, Foglizzo et al., 2007, Ohnishi et al., 2006; 2008, Scheck et al., 2008, Guilet & Foglizzo, 2012, Foglizzo et al., 2015). The SASI develops through an advective-acoustic cycle, entropy

and vorticity perturbations from the shock are advected through the post-shock layer and when they are decelerated at the PNS surface they are converted into pressure waves that propagate out towards the shock front. Once these acoustic waves hit the stalled shock they perturb it, completing the feedback cycle. The large-scale deformation of the shock pushes the average radius outwards and therefore enhances neutrino heating.

1.4 Three-dimensional simulations

After promising results from two-dimensional (2D) simulations supernova modelers experienced initial setbacks in three-dimensional (3D) (Hanke et al., 2012; 2013). Now, however, we are starting to see the emergence of the first generation of successful 3D simulations of explosions with three-flavour multi-group neutrino transport, culminating in the recent models of the Garching and Oak Ridge groups (Melson et al., 2015a;b, Lentz et al., 2015) with their rigorous treatment of the transport and neutrino microphysics in addition to many more obtained with more approximate transport schemes, as for example the studies of Takiwaki et al. (2012; 2014), Müller (2015) and Roberts et al. (2016). Takiwaki et al. (2012; 2014) employ the isotropic diffusion source approximation (Liebendörfer et al., 2009) and use further approximations to treat heavy lepton neutrinos. Takiwaki et al. (2014) employ a leakage scheme to account for heavy lepton neutrinos and Takiwaki et al. (2012) neglect the effect of these neutrinos altogether. Müller (2015) utilises the stationary fast multi-group transport scheme of Müller & Janka (2015), which solves the Boltzmann equation at high optical depths in a two-stream approximation and matches the solution to an analytic variable Eddington factor closure at low optical depths. Roberts et al. (2016) employ a full 3D two-moment (M1) solver in general relativistic simulations, but ignore velocity-dependent terms. On the other hand, it has proven difficult to consistently relaunch the stalled supernova shock in full 3D simulations. Numerical modeling of core-supernovae is an active field of research and as of now there is no consensus of what exactly is the key to successful 3D explosions.

2 Theory

2.1 Linearised theory

One of the most straightforward ways to understand GWs is to expand the Einstein equations around Minkowski space. Mathematically this means that we write the metric tensor, $g_{\mu\nu}$, as

$$g_{\mu\nu} = \eta_{\mu\nu} + h_{\mu\nu}, \quad (2.1)$$

where $\eta_{\mu\nu}$ is the Minkowski metric tensor and $h_{\mu\nu}$ is some small perturbation satisfying

$$|h_{\mu\nu}| \ll 1. \quad (2.2)$$

The condition given by Eq. 2.2 will not hold in an arbitrary reference frame. Therefore, by imposing the smallness condition on $h_{\mu\nu}$ we implicitly chose a frame where the numerical value of the components of $h_{\mu\nu}$ is much smaller than one, in the region of space which we are interested in. In linearised theory we use the Minkowski metric tensor to lower and raise indices.

The field equations of general relativity can be written in terms of the Ricci tensor, $R_{\mu\nu}$, the Ricci scalar, R , the metric tensor, and the energy-momentum tensor, $T_{\mu\nu}$, as follows

$$R_{\mu\nu} - \frac{1}{2}g_{\mu\nu}R = \frac{8\pi G}{c^4}T_{\mu\nu}. \quad (2.3)$$

Before linearising the Einstein equations, by combining Eq. 2.1 and Eq. 2.3, we introduce some simplifying notation. Introducing the quantity

$$h = \eta^{\mu\nu}h_{\mu\nu}, \quad (2.4)$$

and

$$\bar{h}_{\mu\nu} = h_{\mu\nu} - \frac{1}{2}\eta_{\mu\nu}h, \quad (2.5)$$

will allow us to write the equations in a more compact form that is easier to work with. By inserting the expression for the metric tensor (Eq. 2.1) into Eq. 2.3 and expand to linear order in $h_{\mu\nu}$ we find the linearised version of the Einstein equations

$$\partial_\gamma\partial^\gamma\bar{h}_{\mu\nu} + \eta_{\mu\nu}\partial^\rho\partial^\sigma\bar{h}_{\rho\sigma} - \partial^\sigma\partial_\nu\bar{h}_{\mu\sigma} - \partial^\sigma\partial_\mu\bar{h}_{\nu\sigma} = -\frac{16\pi G}{c^4}T_{\mu\nu}. \quad (2.6)$$

We can simplify Eq. 2.6 by using the gauge freedom of linearised theory to impose the Lorentz gauge

$$\partial^\nu \bar{h}_{\mu\nu} = 0. \quad (2.7)$$

Under this gauge condition Eq. 2.6 reduces to a wave equation

$$\partial_\gamma \partial^\gamma \bar{h}_{\mu\nu} = -\frac{16\pi G}{c^4} T_{\mu\nu}, \quad (2.8)$$

since every term, except the first one, on the left hand side vanishes.

Eq. 2.8 further simplifies when we are outside of the sources generating GWs, in vacuum the energy-momentum tensor is zero and we get

$$\partial_\gamma \partial^\gamma \bar{h}_{\mu\nu} = 0, \quad (2.9)$$

which can be rewritten as

$$\frac{1}{c^2} \partial_t^2 \bar{h}_{\mu\nu} = [\partial_x^2 + \partial_y^2 + \partial_z^2] \bar{h}_{\mu\nu}. \quad (2.10)$$

If we compare this expression for $\bar{h}_{\mu\nu}$ to a traditional wave equation, for example that of a sound wave propagating through a fluid or an electromagnetic wave through vacuum, it becomes clear that GWs propagate through spacetime at the speed of light in a wave-like fashion.

2.2 The transverse-traceless gauge

Even though we introduced the Lorentz gauge above, we have not completely removed all non-physical degrees of freedom in the linearised field equations. In vacuum, where the energy-momentum tensor vanishes and Eq. 2.9 holds, it is possible to simplify the expression for $h_{\mu\nu}$. The transverse-traceless gauge (we will denote the transverse-traceless gauge with TT and quantities with a TT are understood to be in the TT-gauge) imposed the following conditions

$$h^{0\mu} = 0, \quad h_i^i = 0, \quad \text{and} \quad \partial^j h_{ij} = 0. \quad (2.11)$$

The solutions to Eq. 2.9 are plane wave solutions and in the TT-gauge the solution for a plane wave propagating along the z-axis is given by

$$h_{ij}^{TT} = \begin{pmatrix} h_+ & h_\times & 0 \\ h_\times & -h_+ & 0 \\ 0 & 0 & 0 \end{pmatrix}_{ij} \cos[\omega(t - z/c)]. \quad (2.12)$$

Here t denotes time, ω the angular frequency of the wave, h_+ denotes the strain of the plus-polarised mode and h_\times is the strain amplitude of the cross-polarised mode. To prove that

we can impose Eq. 2.11 we start by realising that the Lorentz gauge does not completely remove all the superfluous degrees of freedom in the theory. Consider the coordinate transformation

$$x^\mu \rightarrow x'^\mu = x^\mu + \epsilon^\mu, \quad (2.13)$$

where ϵ^μ satisfies $\partial_\gamma \partial^\gamma \epsilon^\mu = 0$, and $|\partial_\nu \epsilon_\mu|$ is at the most on the order of smallness as $|h_{\mu\nu}|$. Under an arbitrary coordinate transformation $x^\mu \rightarrow x'^\mu(x)$ the second rank tensor $h_{\mu\nu}$ transforms as

$$h_{\mu\nu} \rightarrow h'_{\mu\nu} = \frac{\partial x^\gamma}{\partial x'^\mu} \frac{\partial x^\sigma}{\partial x'^\nu} h_{\gamma\sigma}. \quad (2.14)$$

Evaluating Eq. 2.14 for the coordinate transformation given by Eq. 2.13 gives

$$h_{\mu\nu} \rightarrow h'_{\mu\nu} = h_{\mu\nu} - (\partial_\mu \epsilon_\nu + \partial_\nu \epsilon_\mu). \quad (2.15)$$

By combining Eq. 2.15 and Eq. 2.5 we find that under Eq. 2.13 $\bar{h}_{\mu\nu}$ transforms as

$$\bar{h}_{\mu\nu} \rightarrow \bar{h}'_{\mu\nu} = h_{\mu\nu} - (\partial_\mu \epsilon_\nu + \partial_\nu \epsilon_\mu - \eta_{\mu\nu} \partial_\gamma \epsilon^\gamma). \quad (2.16)$$

By applying ∂_μ to Eq. 2.13 we find

$$\partial_\mu x'^\mu = \partial_\mu x^\mu + \partial_\mu \epsilon^\mu. \quad (2.17)$$

Since we have required that $|\partial_\mu \epsilon^\mu| \ll 1$, Eq. 2.17 implies that

$$\partial_\mu x'^\mu = \frac{\partial x'^\mu}{\partial x^\mu} = 1. \quad (2.18)$$

This means that under the transformation given by Eq. 2.13 the derivatives transform as

$$\partial_\mu \rightarrow \partial'_\mu = \partial_\mu. \quad (2.19)$$

We can now calculate how the Lorentz gauge conditions (Eq. 2.7) transform under Eq. 2.13 and we find:

$$\begin{aligned} \partial^\nu \bar{h}_{\mu\nu} &\rightarrow (\partial^\nu \bar{h}_{\mu\nu})' \\ &= \partial^\nu [\bar{h}_{\mu\nu} - (\partial_\mu \epsilon_\nu + \partial_\nu \epsilon_\mu - \eta_{\mu\nu} \partial_\gamma \epsilon^\gamma)] \\ &= \partial^\nu \bar{h}_{\mu\nu} - \partial^\nu \partial_\gamma \epsilon_\mu = 0. \end{aligned} \quad (2.20)$$

Because we demanded that $\partial_\gamma \partial^\gamma \epsilon^\mu = 0$, we can now directly see that the transformation does not break the Lorentz gauge condition. In other words, we are free to perform the coordinate transformation given by Eq. 2.13.

Instead of thinking about how $\bar{h}_{\mu\nu}$ transforms under Eq. 2.13 we can also construct the functions

$$\epsilon_{\mu\nu} \equiv \partial_\mu \epsilon_\nu + \partial_\nu \epsilon_\mu - \eta_{\mu\nu} \partial_\gamma \epsilon^\gamma \quad (2.21)$$

from our four independent functions ϵ_{mu} and are free to subtract these functions from $\bar{h}_{\mu\nu}$ without breaking the gauge condition set by Eq. 2.7. The tool we use to impose these four conditions is the coordinate transform given by Eq. 2.13, with the constraints on ϵ_{mu} and its derivatives specified above. With this freedom, we can now choose the four functions such that they impose four simplifying conditions on $h_{\mu\nu}$. In the TT-gauge the four functions are chosen in such a way that the trace of $\bar{h}_{\mu\nu}$ is zero and $h^{0i} = 0$. Note that if the trace of $\bar{h}_{\mu\nu}$ vanishes $\bar{h}_{\mu\nu} = h_{\mu\nu}$, and we will usually write $h_{\mu\nu}$ instead of $\bar{h}_{\mu\nu}$ when we are in the TT-gauge. These four conditions, together with the Lorentz gauge, define the TT-gauge and result in the conditions given by Eq. 2.11.

2.3 Generation of gravitational waves

We turn now to the generation of gravitational waves. In the linearised theory framework, we start by writing down the solution of Eq. 2.8 for a generic source under the assumption that the gravitational field generated by the source is weak enough to justify the expansion around flat spacetime.

As for any wave equation, the solution of Eq. 2.8 can be found by integrating over the source

$$\bar{h}_{\mu\nu}(t, \mathbf{x}) = \frac{4G}{c^4} \int d^3x' \frac{T_{\mu\nu}(t - |\mathbf{x} - \mathbf{x}'|/c)}{|\mathbf{x} - \mathbf{x}'|}. \quad (2.22)$$

Far way from the source at a distance D , if the velocities, v , within the source are small compared to the speed of light, Eq. 2.22 reduces to the famous Einstein quadrupole formula. In the TT-gauge the quadrupole formula can be written as follows

$$h_{\mu\nu}(t, \mathbf{x}) = \frac{1}{D} \frac{4G}{c^4} \left[P_{im}P_{jn} - \frac{1}{2}P_{ij}P_{mn} \right] \ddot{Q}_{ij}(t - d/c), \quad (2.23)$$

where Q_{ij} is the mass quadrupole moment which to leading order in v/c and in Cartesian coordinates is given by

$$Q_{ij} = \int d^3x \rho(t, \mathbf{x}) \left[x_i x_j - \frac{1}{3} \delta^{ij} x_l x^l \right]. \quad (2.24)$$

$P_{ij} = \delta_{ij} - \hat{n}_i \hat{n}_j$ is the projection operator onto the plane transverse to the direction the wave is propagating, $\hat{n}_i = x_i / \sqrt{x_j x^j}$. To find the equation describing h_+ and h_\times for a wave propagating in the general direction \hat{n} we first consider a wave propagating along the z-axis in a coordinate system with Cartesian coordinates (x, y, z) and spherical polar coordinates (r, θ, ϕ) . If $\hat{n} = \hat{z}$ then P_{ij} becomes

$$P_{ij} = \begin{pmatrix} 1 & 0 & 0 \\ 0 & 1 & 0 \\ 0 & 0 & 0 \end{pmatrix}_{ij}, \quad (2.25)$$

and we find that

$$\left[P_{im}P_{jn} - \frac{1}{2}P_{ij}P_{mn} \right] \ddot{Q}_{ij} = \begin{pmatrix} (\ddot{Q}_{11} - \ddot{Q}_{22})/2 & \ddot{Q}_{12} & 0 \\ \ddot{Q}_{21} & (\ddot{Q}_{22} - \ddot{Q}_{11})/2 & 0 \\ 0 & 0 & 0 \end{pmatrix}_{ij}. \quad (2.26)$$

By comparing Eq. 2.12 and Eq. 2.28 we see that

$$\begin{aligned} h_+^{TT} &= \frac{G}{c^4 D} (\ddot{Q}_{11} - \ddot{Q}_{22}) \\ h_\times^{TT} &= \frac{2G}{c^4 D} \ddot{Q}_{12}. \end{aligned} \quad (2.27)$$

Now consider a wave propagating in the direction given by $\hat{n}' = (\sin \theta \sin \phi, \sin \theta \cos \phi, \cos \theta)$. We can view this as a wave propagating along the z' -axis of a coordinate system, with axes (x', y', z') , that has been constructed by rotating the original system about the z -axis by an angle ϕ and then about the x -axis by an angle θ . The rotation matrix R of the two consecutive rotations is

$$R = \begin{pmatrix} \cos \phi & \sin \phi & 0 \\ -\sin \phi & \cos \phi & 0 \\ 0 & 0 & 0 \end{pmatrix} \begin{pmatrix} 0 & 0 & 0 \\ 0 & \cos \theta & \sin \theta \\ 0 & -\sin \theta & \cos \theta \end{pmatrix}. \quad (2.28)$$

Since $\hat{n}' = \hat{z}'$ we can use the result from Eq. 2.27, but we have to transform the components of \ddot{Q} from the old system (x, y, z) into our new coordinate system (x', y', z') . Under the rotations described by Eq. 2.28 the quadrupole moment transforms as follows

$$\ddot{Q}_{ij} \rightarrow \ddot{Q}'_{ij} = (RQR^T)_{ij}, \quad (2.29)$$

where R^T denotes the transposed matrix R . After some straightforward, but cumbersome, algebra we arrive at

$$\begin{aligned} h_+^{TT} &= \frac{G}{c^4 D} \left[\ddot{Q}_{11}(\cos^2 \phi - \sin^2 \phi \cos^2 \theta) \right. \\ &\quad + \ddot{Q}_{22}(\sin^2 \phi - \cos^2 \phi \cos^2 \theta) - \ddot{Q}_{33} \sin^2 \theta \\ &\quad - \ddot{Q}_{12}(1 + \cos^2 \theta) + \ddot{Q}_{13} \sin \phi \sin 2\theta \\ &\quad \left. + \ddot{Q}_{23} \cos \phi \sin 2\theta \right] \end{aligned} \quad (2.30)$$

and

$$\begin{aligned} h_\times^{TT} &= \frac{G}{c^4 D} \left[(\ddot{Q}_{11} - \ddot{Q}_{22}) \sin 2\phi \cos \theta \right. \\ &\quad + \ddot{Q}_{12} \cos \theta \cos 2\phi - \ddot{Q}_{13} \cos \phi \sin \theta \\ &\quad \left. + 2\ddot{Q}_{23} \sin \phi \sin \theta \right]. \end{aligned} \quad (2.31)$$

Eq. 2.31 and Eq. 2.30 tell us how the waveforms of the emitted GW signal depend on the observers location relative to the source. If we calculate \ddot{Q}_{ij} in a given coordinate system, when dealing with simulations it is often convenient to calculate the quadrupole moment in the coordinate system of the simulations. We can then use Eq. 2.31 and Eq. 2.30 to compute the signal for an observer situated along the direction $\hat{n} = (\sin \theta \sin \phi, \sin \theta \cos \phi, \cos \theta)$.

In principle, we have all the ingredients we need to calculate the gravitational quadrupole radiation as observed by a distant observer for a slow-moving source. However, we are required to calculate the second time derivative of Q_{ij} . In theory this is not a problem, but when dealing with simulations it is difficult to achieve accurate result when performing direct numerical differentiation of the quadrupole moment. Furthermore, in Eq. 2.24 the terms $\rho x_i x_j dV$ will give large weight to slow moving low density fluid elements far away from the regions where GWs are actually produced. On the other hand, the second time derivative of these contributions will be small, because faster moving and denser matter will contribute more to the GW amplitudes. Again, this is not problematic in theory, but when numerically computing the integral and second-order time derivatives the exact cancellation of the large average value and the rate of change of the quadrupole moment is hard to achieve. We can circumvent these problems by using the Euler equations to rewrite Eq. 2.24. This allows us to eliminate the time derivatives completely and to write the quadrupole moment in terms of quantities which are more closely connected to the regions of the simulation where GWs are produced (Oohara et al., 1997, Finn, 1989, Blanchet et al., 1990).

The standard Euler equations of a self-gravitating fluid are

$$\partial_t \rho + \partial_i(\rho v^i) = 0, \quad (2.32a)$$

$$\partial_t(\rho v^i) + \partial_j(\rho v^i v^j) = -\partial_i p - \rho \partial_i \Phi, \quad (2.32b)$$

$$\partial_t(\rho \varepsilon) + \partial_i(\rho \varepsilon v^i) = -p \partial_i v^i, \quad (2.32c)$$

where p , v^i , ε , and ρ are the pressure, the velocity components, the internal energy density, and the mass density of the fluid, respectively. The Newtonian potential is denoted by Φ , and we have neglected any radiation back-reaction.

Taking the first time derivative of Eq. 2.24 yields

$$\begin{aligned} \frac{d}{dt} Q_{ij} &= \frac{d}{dt} \int d^3x \rho \left[x_i x_j - \frac{1}{3} \delta^{ij} x_l x^l \right] \\ &= \int d^3x \left[x_i x_j - \frac{1}{3} \delta^{ij} x_l x^l \right] \partial_t \rho \\ &= - \int d^3x \left[x_i x_j - \frac{1}{3} \delta^{ij} x_l x^l \right] \partial_k(\rho v^k), \end{aligned} \quad (2.33)$$

where we used Eq. 2.32a in the last line to replace $\partial_t \rho$ with $-\partial_k(\rho v^k)$. Now we integrate Eq. 2.33 by parts and use the fact that astrophysical GW sources have finite sizes to discard

the boundary terms. We find that

$$\begin{aligned}\frac{d}{dt}Q_{ij} &= \int d^3x \rho v^k \partial_k \left[x_i x_j - \frac{1}{3} \delta^{ij} x_l x^l \right] \\ &= \int d^3x \rho v^k \left[\partial_k x_i x_j - \frac{1}{3} \delta^{ij} \partial_k (x_l x^l) \right] \\ &= \int d^3x \rho \left[x_i v_j + v_i x_j - \frac{2}{3} \delta^{ij} v_l x^l \right],\end{aligned}\quad (2.34)$$

where we integrated the first line by parts to get to the second line, and when going from the second to the third line we used the fact that $\partial_k x_i = \delta^{ki}$. We have now removed the first time derivative from Eq. 2.24, and we have replaced one power of x^i with v^i which reduces the weight given to slow moving regions. Next we take the time derivative of Eq. 2.34, which yields

$$\begin{aligned}\frac{d^2}{dt^2}Q_{ij} &= \frac{d}{dt} \int d^3x \rho \left[x_i v_j + v_i x_j - \frac{2}{3} \delta^{ij} v_l x^l \right], \\ &= \int d^3x \left[x_i (\partial_t \rho v_j) + (\partial_t \rho v_i) x_j - \frac{2}{3} \delta^{ij} \partial_t (\rho v_l) x^l \right].\end{aligned}\quad (2.35)$$

Now we use Eq. 2.32b to remove $\partial_t \rho v_i$ and we get

$$\begin{aligned}\frac{d^2}{dt^2}Q_{ij} &= \int d^3x \left[x_i (-\partial_j p - \rho \partial_j \Phi - \partial_k (\rho v_j v_k)) \right. \\ &\quad + x_j (-\partial_i p - \rho \partial_i \Phi - \partial_k (\rho v_i v_k)) \\ &\quad \left. - \frac{2}{3} \delta^{ij} x^l (-\partial_l p - \rho \partial_l \Phi - \partial_k (\rho v_l v_k)) \right].\end{aligned}\quad (2.36)$$

After integrating by parts terms of the form $\partial_i p$ and $\partial_k (\rho v_i v_k)$ we are left with

$$\begin{aligned}\frac{d^2}{dt^2}Q_{ij} &= \int d^3x \rho \left[2v_i v_j - x_i \partial_j \Phi - x_j \partial_i \Phi \right. \\ &\quad \left. - \frac{2}{3} \delta^{ij} (\rho v_l v_l - \rho x_l \partial_l \Phi) \right].\end{aligned}\quad (2.37)$$

Note that the terms containing the pressure in Eq. 2.36 cancel. The last step is to write Eq. 2.37 in a slightly more compact form

$$\ddot{Q}_{ij} = \text{STF} \left[2 \int d^3x \rho (v_i v_j - x_i \partial_j \Phi) \right].\quad (2.38)$$

Here STF denotes the projection operator onto the symmetric trace-free part, $\text{STF}[A_{ij}] = \frac{1}{2} A_{ij} + \frac{1}{2} A_{ji} - \frac{1}{3} \delta_{ij} A_{ll}$. We have also adopted the notation that \dot{x} represents the first time derivative of x , \ddot{x} the second time derivative, and so on. In the end, we are left

with an expression for the second time derivative of the quadrupole moment that depends on first-order spatial derivatives of the gravitational potential and the Cartesian velocity components. These terms have larger numerical values in the regions of the simulation generating most of the GWs, which is an advantage when numerically calculating the integral in Eq. 2.38. We have also eliminated the troublesome second-order time derivatives and arrived at a formula that is much more suited for computing waveforms in numerical studies than our starting point.

Note that in axisymmetry the only independent component of $h_{\mu\nu}^{TT}$ is

$$\mathbf{h}_{\theta\theta}^{TT} = \frac{1}{8} \sqrt{\frac{15}{\pi}} \sin^2 \theta \frac{A_{20}^{E2}}{D}, \quad (2.39)$$

where D is the distance to the source, θ is the inclination angle of the observer with respect to the axis of symmetry, and A_{20}^{E2} represents the only non-zero quadrupole amplitude. In spherical coordinates A_{20}^{E2} can be expressed as follows

$$A_{20}^{E2}(t) = \frac{G}{c^4} \frac{16\pi^{3/2}}{\sqrt{15}} \int_{-1}^1 \int_0^\infty \rho [v_r^2(3z^2 - 1) + v_\theta^2(2 - 3z^2) - v_\phi^2 - 6v_r v_\theta z \sqrt{1 - z^2} + r \partial_r \Phi(3z^2 - 1) + 3\partial_\theta z \sqrt{1 - z^2} \Phi] r^2 dr dz. \quad (2.40)$$

Here, v_i and ∂_i ($i = r, \theta, \phi$) represent the velocity components and derivatives, respectively, along the basis vectors of the spherical coordinate system, and $z \equiv \cos \theta$. For details we refer the reader to Müller & Janka (1997).

In the quadrupole framework the energy, E , radiated by GWs is given by

$$E = \frac{G}{5c^5} \int dt \ddot{Q}_{ij} \ddot{Q}_{ij}, \quad (2.41)$$

and the spectral energy density of the GWs is given by

$$\begin{aligned} \frac{dE}{df} &= \frac{2G}{5c^5} (2\pi f)^2 \tilde{\dot{Q}}_{ij} \tilde{\dot{Q}}_{ij} \\ &= \frac{2c^3}{5G} (2\pi f)^2 \left[|\tilde{\dot{Q}}_{xx}|^2 + |\tilde{\dot{Q}}_{yy}|^2 + |\tilde{\dot{Q}}_{zz}|^2 \right. \\ &\quad \left. + 2(|\tilde{\dot{Q}}_{xy}|^2 + |\tilde{\dot{Q}}_{xz}|^2 + |\tilde{\dot{Q}}_{yz}|^2) \right], \end{aligned} \quad (2.42)$$

where a tilde denotes a Fourier transform, and f is the frequency. We define the Fourier transform as follows:

$$\tilde{\dot{Q}}_{ij}(f) = \int_{-\infty}^{\infty} \ddot{Q}_{ij}(t) e^{-2\pi ift} dt. \quad (2.43)$$

For a discrete time series the Fourier transform is replaced by the discrete Fourier transform (DFT). We define the DFT, \tilde{X}_k , as follows:

$$\tilde{X}_k(f_k) = \frac{1}{M} \sum_{m=1}^M x_m e^{-2\pi i k m / M}, \quad (2.44)$$

Here, x_m is the time series obtained by sampling the underlying continuous signal at M discrete times. $f_k = k/T$ is the frequency of bin k , where T is the duration of the signal.

We will repeat these definitions and discuss our Fourier analysis in detail in a later chapter.

3 Numerical simulations of core-collapse supernovae

The GW signals presented in this thesis is based on supernova simulations that were performed with the code PROMETHEUS-VERTEX. The simulations were carried out by members of the Garching-group (Hanke (2014), Melson (2016), Summa (2017)). In this chapter we described the code that was used, we will describe the details of individual models in later chapters. PROMETHEUS-VERTEX solves the combined problem of hydrodynamics and neutrino radiation transport. The code has been specifically developed for the core-collapse problem, the first version was developed in 2002 by Rampp & Janka (2002)

3.1 Prometheus

The hydrodynamics of the stellar collapse is solved with a version of the well-established PROMETHEUS code (Müller et al., 1991, Fryxell et al., 1991). It solves the non-relativistic equations of hydrodynamics for the inviscid flow of an ideal fluid in spherical coordinates (r, θ, ϕ) .

3.1.1 Hydrodynamics

In spherical coordinates the Euler equations of hydrodynamics are

$$\partial_t \rho + \frac{1}{r^2} \partial_r (r^2 \rho v_r) + \frac{1}{r \sin \theta} \left[\partial_\theta (\rho \sin \theta v_\theta) + \partial_\phi (\rho v_\phi) \right] = 0, \quad (3.1)$$

$$\begin{aligned} \partial_t (\rho v_r) + \frac{1}{r \sin \theta} & \left[\partial_\theta (\rho \sin \theta v_\theta v_r) + \partial_\phi (\rho v_\phi v_r) \right] + \\ \frac{1}{r^2} \partial_r (r^2 \rho v_r^2) - \rho & \frac{v_\theta^2 + v_\phi^2}{r} + \partial_r p = -\rho \partial_r \Phi + Q_{M_r}, \end{aligned} \quad (3.2a)$$

$$\begin{aligned} \partial_t (\rho v_\theta) + \frac{1}{r^2} \partial_r (r^2 \rho v_r v_\theta) + \frac{1}{r \sin \theta} & \left[\partial_\theta (\rho \sin \theta v_\theta^2) + \partial_\phi (\rho v_\phi v_\theta) \right] \\ + \rho & \frac{v_\theta v_r - v_\phi^2 / \tan \theta}{r} + \frac{1}{r} \partial_\theta p = -\frac{\rho}{r} \partial_\theta \Phi + Q_{M_\theta}, \end{aligned} \quad (3.2b)$$

$$\begin{aligned} \partial_t (\rho v_\phi) + \frac{1}{r \sin \theta} & \left[\partial_\theta (\rho \sin \theta v_\theta v_\phi) + \partial_\phi (\rho v_\phi^2) + \partial_\phi p \right] \\ + \frac{1}{r^2} \partial_r (r^2 \rho v_r v_\phi) + \rho & \frac{v_\theta v_\phi / \tan \theta + v_\phi v_r}{r} = -\frac{1}{r \sin \theta} \partial_\phi \Phi + Q_{M_\phi}, \end{aligned} \quad (3.2c)$$

$$\begin{aligned} \partial_t e + \frac{1}{r^2} \partial_r (r^2 v_r (e + p)) + \frac{1}{r \sin \theta} & \left[\partial_\theta (\sin \theta v_\theta (e + p)) + \partial_\phi (v_\phi (e + p)) \right] \\ = -\rho v_r \partial_r \Phi - \rho & \frac{v_\theta}{r} \partial_\theta \Phi - \frac{v_\phi}{r \sin \theta} \partial_\phi \Phi + Q_E + v_r Q_{M_r} + v_\theta Q_{M_\theta} + v_\phi Q_{M_\phi}. \end{aligned} \quad (3.4)$$

Here p is pressure, ρ is density, e is the specific total energy, Φ is the gravitational potential and v_r , v_θ , and v_ϕ are the velocity components in the spherical coordinate basis. The source terms Q_{M_r} , Q_{M_θ} , and Q_{M_ϕ} represent momentum transfer by neutrinos, in the radial, polar, and azimuthal direction, respectively. Energy transport by neutrinos is represented by the source term Q_{M_E} . These source terms are calculated by the neutrino-transport module VERTEX, which we will come back to them later in the chapter. The above equations have to be closed by an EoS, which generally will depend on density, internal energy, and the chemical composition of the stellar matter. This means that one has to track of two additional quantities, the mass fractions of different nuclear species, denoted by X_i , and the electron fraction Y_e . We, therefore, have to solve two additional conservation equations:

$$\partial_t (\rho X_i) + \frac{1}{r^2} \partial_r (r^2 \rho v_r X_i) + \frac{1}{r \sin \theta} \left[\partial_\theta (\rho \sin \theta v_\theta X_i) + \partial_\phi (\rho v_\phi X_i) \right] = \varsigma_i, \quad (3.5)$$

$$\partial_t (\rho Y_e) + \frac{1}{r^2} \partial_r (r^2 \rho v_r Y_e) + \frac{1}{r \sin \theta} \left[\partial_\theta (\rho \sin \theta v_\theta Y_e) + \partial_\phi (\rho v_\phi Y_e) \right] = Q_{Y_e}. \quad (3.6)$$

The two terms ς_i and Q_{Y_e} represents the change of composition of species i due nuclear reactions and the change in electron fraction caused by emission and absorption of electron and anti-electron neutrinos, respectively. If the fluid reaches nuclear statistical equilibrium

(NSE), then the chemical composition is fully determined by the equation of state, through the electron fraction, density, and temperature.

PROMETHEUS solves the system of equations described in the paragraph above by means of a dimensionally-split implementation of the piecewise parabolic method of Colella & Woodward (1984). The scheme is time-explicit and it is accurate to third-order in space and second-order in time. The Riemann solver exactly solves 1D Riemann problems in so-called sweeps that have been obtained from the full 3D equations by Strange-splitting (Strang, 1968). When strong shocks are encountered the solver switches to the “HLL” solver (Einfeldt, 1988). This is done in order to avoid the so-called “even-odd decoupling”, which occurs when the shocks are aligned with one of the axes of the simulation grid (Quirk, 1994, Kifonidis et al., 2003), which creates artificial oscillations. PROMETHEUS employs the consistent multi-fluid advection method of Plewa & Müller (1999) to ensure that the advection all the nuclear species is calculated accurately.

3.1.2 Equation of state

The models that this work is based on uses two different prescriptions for the EoS. A “high-density” EoS is used for the inner hot region of the core, while a “low-density” EoS is used for the low-density regions of the simulation volume. The two are separated by a density threshold, after core bounce this threshold is set to $\rho_T = 10^{11}$ g/cm³. In the high-density regime the tabular EoS of Lattimer & Swesty (1991) with a nuclear incompressibility of 220 MeV is used. Below the threshold, in the low-density regime, an EoS that describes the nuclei as classical Boltzmann gases. Electrons and positrons are described as Fermi gases with arbitrary degeneracy levels. The EoS also include the effect of photons (Janka, 1999).

3.1.3 Self gravity - the effective potential

Self-gravity is treated using the monopole approximation and the effects of general relativity are accounted for in an approximate fashion by means of a pseudo-relativistic effective potential (case A of Marek et al. (2006)). The effective potential includes general relativistic effects and takes the properties of the medium into account, such as the pressure and energy of the fluid elements. In the case of a monopole potential, the terms involving non-radial derivatives of the potential in the Euler equations vanish.

3.2 Vertex

The VERTEX code calculates the source terms on the right-hand side of the Euler equations by treating the neutrinos as a radiation field. The problem we need to solve is to find the

phase-space distribution function $f(\mathbf{r}, \mathbf{q}, t)$ of the neutrinos. Essentially we want to find the number of neutrinos momentum \mathbf{q} at position \mathbf{r} , in other words the number of particles in the phase-space volume $d\mathbf{q}d\mathbf{r}$.

It is common to work in terms of the specific intensity $\mathfrak{I}(\mathbf{r}, \hat{n}, \xi, t)$, which is defined such that the amount of energy $d\xi$ transported in the energy interval $(\xi, \xi + d\xi)$, by neutrinos propagating into the solid angle $d\Omega$ in the direction \hat{n} , through a surface with area dA , with normal vector $\hat{A} = \mathbf{r}/|\mathbf{r}|$, during the time interval dt is

$$d\xi = \mathfrak{I}(\mathbf{r}, \hat{n}, \xi, t) \hat{n} \cdot \hat{A} d\xi dA d\Omega dt. \quad (3.7)$$

The neutrino distribution function and the specific neutrino intensity is related as follows

$$\mathfrak{I}(\mathbf{r}, \hat{n}, \xi, t) = \frac{\xi^3}{h^3 c^2} f(\mathbf{r}, \hat{n}, \xi, t). \quad (3.8)$$

The evolution of the specific neutrino intensity is calculated by solving the Boltzmann equation

$$\frac{1}{c} \partial_t \mathfrak{I} + \hat{n}_i \partial_i \mathfrak{I} = \mathfrak{C}[\mathfrak{I}]. \quad (3.9)$$

The right hand side of Eq. 3.9 is a source term that describes scattering, emission and absorption of neutrinos (the so-called collision integral). $\mathfrak{C}[\mathfrak{I}]$ will in general depend on integrals of the specific neutrino intensity, which makes the problem difficult to solve numerically. A common strategy is to expand the specific neutrino intensity into angular moments

$$\mathfrak{L}(\mathbf{r}, \xi, t) \equiv \frac{1}{4\pi} \int \mathfrak{I} d\Omega \quad (0^{\text{th}} - \text{order}), \quad (3.10)$$

$$\mathfrak{H}_i(\mathbf{r}, \xi, t) \equiv \frac{1}{4\pi} \int \mathfrak{I} \hat{n}_i d\Omega \quad (1^{\text{st}} - \text{order}), \quad (3.11)$$

$$\mathfrak{K}_{ij}(\mathbf{r}, \xi, t) \equiv \frac{1}{4\pi} \int \mathfrak{I} \hat{n}_i \hat{n}_j d\Omega \quad (2^{\text{nd}} - \text{order}), \quad (3.12)$$

⋮

and then solve the equations that arises when inserting these moments into Eq. 3.9

$$\frac{1}{c} \partial_t \mathfrak{L} + \partial_i \mathfrak{H}_i = \frac{1}{4\pi} \int \mathfrak{C}[\mathfrak{I}] d\Omega, \quad (3.13)$$

$$\frac{1}{c} \partial_t \mathfrak{H}_i + \partial_i \mathfrak{K}_{ij} = \frac{1}{4\pi} \int \mathfrak{C}[\mathfrak{I}] \hat{n}_i d\Omega. \quad (3.14)$$

⋮

We see from these equations that the evolution of the k^{th} -order moment depends on $(k+1)^{\text{th}}$ -order moment.

The version of VERTEX that is implemented into PROMETHEUS-VERTEX uses the so-called “ray-by-ray-plus” approximation of Buras et al. (2006a) (see Hanke (2014) for details about the implementation). For each angular direction of the simulation grid a spherical symmetric radiation problem is solved with the “ray-by-ray-plus” method, by assuming that the radiation field is symmetric around the rays propagation direction. In other words, the code traces one “ray” per angular bin, this is what is known as the “ray-by-ray” method. In this case the angular moments of the specific neutrino intensity can be represented by scalars. Furthermore, the expansion of the specific neutrino intensity is truncated at 1st-order and closed with a variable Eddington factor method. The two Eddington factors that are needed to close the system are the ratio of the 0th-order and the 3rd-order scalar angular moments and the ratio of the 0th-order and the 4th-order scalar angular moments. The two factors are calculated from a simplified version of the Boltzmann equation in an iterative process until convergence within an acceptable error is reached. Buras et al. (2006b) found that it is necessary to take non-radial advection of neutrinos and the non-radial neutrino pressure gradients into account to avoid un-physical convection in the PNS. The inclusion of these terms is what is meant by the “plus” in “ray-by-ray plus”.

VERTEX solves the neutrino transport problem for three neutrino species, ν_e , $\bar{\nu}_e$, and a species ν_X representing all heavy flavor neutrinos. For the models that make the basis of this work, the neutrinos were binned into 12 logarithmically spaced energy bins ranging from 0 to 380 MeV. A more detail description of the numerical implementation, neutrino physics, and the VERTEX in general can be found Rampp & Janka (2002), Hanke (2014), and Melson (2016).

3.3 Grid setup

Since stars are, at least to lowest order, spherical objects it is advantageous to use a spherical grid when performing numerical simulations. PROMETHEUS-VERTEX can use two different spherical grids.

3.3.1 Spherical polar grid

The first grid available in PROMETHEUS-VERTEX is a standard spherical polar grid, with mesh points $r_n \in [0, R]$, $\theta_n \in [0, \pi]$, and $\phi_n \in [0, 2\pi]$. The grid is logarithmic space in radius and the angular points are spaced equidistantly. The structure of “standard” spherical polar (r, θ, ϕ) has a few shortcomings that can be problematic when performing numerical simulations. The grid contains coordinate singularities at the poles ($\theta = 0$ and $\theta = \pi$) and grid cells become smaller and smaller the closer one gets to the poles.

This causes strong constraints on the time step and can even lead to numerical artifacts near the poles (Wongwathanarat et al., 2010a, Müller, 2015).

3.3.2 Yin-Yang grid

To avoid the problems encountered at the poles of a standard spherical grid, Kageyama & Sato (2004) proposed to construct a grid from two geometrically identical subgrids (called Yin and Yang). The two sub-grids are both spherical and have identical local coordinates, their mesh points are defined as follows

$$r_n^Y \in [0, R], \quad (3.15)$$

$$\theta_n^Y \in [pi/4, 3\pi/4], \quad (3.16)$$

$$\phi_n^Y \in [-3pi/4, 3\pi/4]. \quad (3.17)$$

Here the superscript Y refers to either the *Yin* or *Yang*. While the two grids have identical local coordinates, they are rotated in respect to each other in such a way to cover the whole sphere. The two grids are orientated in such that if the Cartesian coordinates of the *Yin* grid are $(x^{Yin}, y^{Yin}, z^{Yin})$ then the local Cartesian coordinates of the *Yang* grid are

$$(x^{Yang}, y^{Yang}, z^{Yang}) = (-x^{Yin}, z^{Yin}, y^{Yin}). \quad (3.18)$$

The *Yang* grid is rotated 90 degrees around the x-axis and 180 degrees around the y-axis of the *Yin* grid. This corresponds to the rotation matrix

$$R = \begin{pmatrix} -1 & 0 & 0 \\ 0 & 0 & 1 \\ 0 & 1 & 0 \end{pmatrix}. \quad (3.19)$$

With this prescription we avoid the problems that arise near the poles of a normal spherical grid. For more details about the implementation of the *Yin-Yang* grid in PROMETHEUS-VERTEX see Melson (2016).

4 Signal analysis

4.1 Fourier analysis

In order to study the frequency structure of a time signal it is common to approximate the signal as a sum of trigonometric functions. Two examples of such analysis is Fourier series and Fourier transforms, in this chapter we will mainly focus on the latter and discuss the tools used for signal analysis in this thesis.

4.1.1 Continuous and discrete Fourier transforms

We define the continuous Fourier transform (FT) of a continuous time signal $x(t)$ as

$$\tilde{x}(f) = \int_{-\infty}^{\infty} x(t)e^{-2\pi ift} dt. \quad (4.1)$$

The FT transforms the signal from the time domain into the frequency (f) domain. Simply put, the Fourier transformation tells us how much an oscillation of frequency f contributes to the total signal.

If the time signal is represented by a discrete time series, as is the case with data from simulations, the integral on the right-hand side of Eq. 4.1 can be estimated by numerical integration and we can derive an expression for the corresponding discrete Fourier transform (DFT). Consider the time series x_m of duration T which has been obtained by sampling the underlying continuous signal $x(t)$ at M discrete, evenly spaced, times

$$x_m = x(t_m) = x(m \Delta t) \quad m = 0, 1, 2, 3, 4 \dots M, \quad (4.2)$$

where $\Delta t (= T/M)$ is the sampling interval. The time series x_m is by construction a periodic function with period T , regardless of the true periodicity of the underlying function. This implies that $x_M = x_0$. Since our signal has period T it means that frequency of the slowest varying oscillation we can represent is $1/T$. By the same logic the second slowest oscillation we can capture has a frequency of $1/(T - \Delta t)$ and so on. This means that the discrete signal is represented by a set of $M + 1$ frequencies

$$f_k = k/M\Delta t \quad k = 0, 1, 2, 3, 4 \dots M. \quad (4.3)$$

We now calculate the integral in Eq. 4.1 for a given frequency f_k using the trapezoidal rule and find

$$\begin{aligned} \int_{-\infty}^{\infty} x(t)e^{-2\pi if_k t} dt &\simeq \int_0^T x(t)e^{-2\pi if_k t} dt \\ &\approx \sum_{m=1}^M x_m e^{-2\pi if_k t_m} \Delta t \\ &= \sum_{m=1}^M x_m e^{-2\pi i k m / M} \Delta t \equiv \tilde{X}_k \Delta t M. \end{aligned} \quad (4.4)$$

In the last line we have defined the discrete Fourier transform (DFT) of a time series x_m

$$\tilde{X}_k(f_k) = \frac{1}{M} \sum_{m=1}^M x_m e^{-2\pi i k m / M}. \quad (4.5)$$

4.2 The short-time Fourier transform

The disadvantage of the Fourier transform is that it only gives you information about the frequency spectrum of the full-time signal. If we are analysing a signal with a varying frequency structure it will be useful to extract time-frequency information about the signal. This is done by separating the signal into shorter segments and then calculating the Fourier transform of each segment. In this way, we obtain spectral information about the signal at different times.

There are several ways to segment the signal, the method used in this thesis is to slide a time-window of length τ over the time signal, $x(t)$, in an iterative process. In each iteration, the window is shifted forward in time by $\Delta\tau$. This define a set of functions

$$S^i \equiv x(t)[H(t + i\Delta\tau) - H(t + \tau + i\Delta\tau)] \quad i = 0, 1, 2, 3, \dots, \quad (4.6)$$

where $H(t)$ is the Heaviside step function. The short-time Fourier transform (STFT) of $x(t)$ is then

$$\text{STFT}[x(t)] \equiv \int_{-\infty}^{\infty} S^i e^{-2\pi ift} dt = \tilde{S}_k^i \quad i = 0, 1, 2, 3, \dots, \quad (4.7)$$

4.3 The Nyquist frequency and aliasing

An important question when sampling a continuous time signal is how many samples are required to accurately represent the signal.

The Nyquist sampling theorem Let $x_b(t)$ be a band-limited signal, that is

$$\tilde{x}_b(f) = 0 \quad \text{iff } f > f_N, \quad (4.8)$$

where f_N is the band-limit of x_b . If x_b is sampled with a sampling frequency

$$f_s \geq 2f_N \quad (4.9)$$

then the signal is uniquely determined by its samples. The frequency f_N is referred to as the Nyquist frequency.

If a signal is sampled at a lower rate than half the Nyquist frequency then the signal will not be accurately represented and what is known as aliasing occurs. Suppose that we sample a signal which a sampling rate f_s and that the signal contains oscillations at frequencies larger than $f_s/2$. Then the DFT will not be able to distinguish between oscillations with frequencies $f_c > f_s/2$ and $f - 2f_s$. This means that oscillations at a frequency f_c will be aliased down into to the frequency

$$f_a = f_c - f_N. \quad (4.10)$$

In the case of hydrodynamic simulations, aliasing can appear when data is not saved to disk frequently enough. In large 3D simulations, it is often unfeasible to save all the hydro-data for each individual time-step. It is, therefore, common to save data to disk at a given time interval. The simulations which the GW signals presented in this work are based on saved data roughly two times per millisecond of simulated time, which results in a Nyquist frequency of 1000 Hz.

4.4 The spectral energy density of a discrete time signal

Eq. 2.42 gives the expression for the spectral energy density of a continuous time signal, it is obtained by directly applying Parseval's theorem to Eq. 2.41.

Parseval's theorem If \tilde{x} is the Fourier transform of $x(t)$ then

$$\int_{-\infty}^{\infty} |x(t)|^2 dt = \int_{-\infty}^{\infty} |\tilde{x}(f)|^2 df. \quad (4.11)$$

To derive the corresponding expression for a discrete time series, first consider the quantity

$$\Gamma = \int_{-\infty}^{\infty} g(t)^2 dt = \int_{-\infty}^{\infty} |\tilde{g}|^2 df. \quad (4.12)$$

Next we construct the time-series g_n by sampling $g(t)$ M times over a time period T . We then use the same procedure we used to derive the Eq. 4.4, that is to approximate the integral using the trapezoidal rule. This procedure yields

$$\begin{aligned}\Gamma &= \int_{-\infty}^{\infty} |\tilde{g}|^2 df \\ &\approx \sum_{k=1}^M \left| \sum_{m=1}^M x_m e^{-2\pi i km/M} \Delta t \right|^2 \Delta f \\ &= \sum_{k=1}^M |\tilde{g}_k|^2 T^2 \Delta f = \sum_{k=1}^M |\tilde{g}_k|^2 T,\end{aligned}\quad (4.13)$$

where we in the last line have used that $\Delta f = 1/T$ and $\Delta t = T/M$ (the $1/M^2$ is absorbed in to the DFT). This implies that

$$\begin{aligned}\frac{d}{df} \Gamma &= \frac{d}{df} \int_{-\infty}^{\infty} |\tilde{g}|^2 df \\ &\approx |\tilde{g}_k|^2 T^2.\end{aligned}\quad (4.14)$$

The last step is to replace the placeholder function g by \ddot{Q}_{ij} and use the fact that

$$\widetilde{x(t)} = 2\pi f \widetilde{x(t)}. \quad (4.15)$$

We then find that

$$\frac{d}{df} E \approx \left[\frac{\Delta E}{\Delta f} \right]_k = \frac{2G}{5c^5} (2\pi f_k)^2 |\widetilde{Q}^{ij}_k \widetilde{Q}^{ij}_k| T^2. \quad (4.16)$$

Here we have moved the ij subscript of Q_{ij} up for better readability.

5 First paper

5.1 Introduction

Despite impressive progress during recent years, the explosion mechanism powering core-collapse supernovae is still not fully understood. For ordinary supernovae with explosion energies up to $\sim 10^{51}$ erg, the prevailing theory is the delayed neutrino-driven mechanism (see Janka, 2012, Burrows, 2013 for current reviews). In this scenario, the shock wave formed during the rebound (bounce) of the inner core initially stalls and only propagates out to a radius of ~ 150 km. The energy needed to revitalise the shock is provided by the partial re-absorption of neutrinos emitted from the proto-neutron star (PNS).

Hydrodynamical instabilities operating behind the stalled shock front have been found to be crucial for the success of this scenario as they help to push the shock further out by generating large Reynolds Stresses (or “turbulent pressure”, see Burrows et al., 1995, Murphy et al., 2013, Couch & Ott, 2015, Müller & Janka, 2015) and transporting neutrino-heated material out from the gain radius, which then allows the material to be exposed to neutrino heating over a longer “dwell time” (Buras et al., 2006b, Murphy & Burrows, 2008b). Moreover, if the instabilities lead to the formation of sufficiently large high-entropy bubbles, the buoyancy of these bubbles can become high enough to allow them to rise and expand continuously (Thompson, 2000, Dolence et al., 2013, Fernández, 2015).

Two such instabilities have been identified in simulations, namely the more familiar phenomenon of convection driven by the unstable entropy gradient arising due to neutrino heating (Bethe, 1990, Herant et al., 1994, Burrows et al., 1995, Janka & Müller, 1996, Müller & Janka, 1997), and the so-called standing accretion shock instability (SASI), which manifests itself in large-scale sloshing and spiral motions of the shock (Blondin et al., 2003, Blondin & Mezzacappa, 2006, Foglizzo et al., 2007, Ohnishi et al., 2006; 2008, Scheck et al., 2008, Guilet & Foglizzo, 2012, Foglizzo et al., 2015). After initial setbacks in three-dimensional (3D) supernova modelling, we are now starting to see the emergence of the first generation of successful 3D simulations of explosions with three-flavour multi-group neutrino transport, culminating in the recent models of the Garching and Oak Ridge groups (Melson et al., 2015a;b, Lentz et al., 2015) with their rigorous treatment of the transport and neutrino microphysics in addition to many more obtained with more approximate transport schemes, as for example the studies of Takiwaki et al. (2012; 2014), Müller (2015) and

Roberts et al. (2016).^{*}

Our means to validate these numerical models by observations are limited. Classical photon-based observations of supernovae and their remnants (e.g. mixing in the envelope, see Wongwathanarat et al., 2015 and references therein; pulsar kicks, Scheck et al., 2006, Wongwathanarat et al., 2010b; 2013, Nordhaus et al., 2012) provide only relatively indirect constraints on the workings of these hydrodynamic instabilities in the inner engine of a supernova during the first second after the collapse. For a nearby, galactic supernova event, messengers from the core in the form of neutrinos and gravitational waves (GWs) could furnish us with a direct glimpse at the engine. Neutrinos, for example, could provide a smoking gun for SASI activity through fast temporal variations (Marek et al., 2009, Lund et al., 2010, Brandt et al., 2011, Tamborra et al., 2013; 2014a, Müller & Janka, 2014) and could even allow a time-dependent reconstruction of the shock trajectory (Müller & Janka, 2014).

Likewise, a detection of GWs could potentially help to unveil the multi-dimensional effects operating in the core of a supernova. The signal from the collapse and bounce of rapidly rotating iron cores and triaxial instabilities in the early post-bounce phase has long been studied in 2D (i.e. under the assumption of axisymmetry) and 3D (e.g. Ott et al., 2007, Dimmelmeier et al., 2007; 2008, Scheidegger et al., 2008, Abdikamalov et al., 2010). Understanding the GW signal generated by convection and the SASI in the more generic case of slow or negligible rotation has proved more difficult due to a more stochastic nature of the signal. During the recent years, however, a coherent picture of GW emission has emerged from parameterised models (Murphy et al., 2009) and first-principle simulations of supernova explosions in 2D (Marek et al., 2009, Müller et al., 2013): The models typically show an early, low-frequency signal with typical frequencies of ~ 100 Hz arising from shock oscillations that are seeded by prompt convection (Marek et al., 2009, Murphy et al., 2009, Yakunin et al., 2010, Müller et al., 2013, Yakunin et al., 2015). This signal component is followed by a high-frequency signal with stochastic amplitude modulations that is generated by forced oscillatory motions in the convectively stable neutron star surface layer (Marek et al., 2009, Murphy et al., 2009, Müller et al., 2013) with typical frequencies of 300 ... 1000 Hz that closely trace the Brunt-Väisälä frequency in this region (Müller et al., 2013). Prior to the explosion, these oscillations, tentatively identified as $l = 2$ surface g-modes by Müller et al. (2013), are primarily driven by the downflows impinging onto the neutron star, whereas PNS convection takes over as the forcing agent a few hundred milliseconds after shock revival as accretion dies down. This high-frequency contribution

^{*}Takiwaki et al. (2012; 2014) employ the isotropic diffusion source approximation (Liebendörfer et al., 2009) and use further approximations to treat heavy lepton neutrinos. Takiwaki et al. (2014) employ a leakage scheme to account for heavy lepton neutrinos and Takiwaki et al. (2012) neglect the effect of these neutrinos altogether. Müller (2015) utilises the stationary fast multi-group transport scheme of Müller & Janka (2015), which at high optical depths solves the Boltzmann equation in a two-stream approximation and matches the solution to an analytic variable Eddington factor closure at low optical depths. Roberts et al. (2016) employ a full 3D two-moment (M1) solver in general relativistic simulations, but ignore velocity-dependent terms.

dominates the energy spectrum and the total energy emitted in GWs can reach $\sim 10^{46}$ erg (Müller et al., 2013, Yakunin et al., 2015).

Since 3D supernova models have proved fundamentally different to 2D models in many respects, it stands to reason that much of what we have learned about GW emission from first-principle 2D models will need to be revised. In 2D, the inverse turbulent cascade (Kraichnan, 1967) facilitates the emergence of large-scale flow structures also in convectively-dominated models and helps to increase the kinetic energy in turbulent fluid motions in the post-shock region (Hanke et al., 2012). Furthermore, accretion downflows impact the PNS with much higher velocities in 2D than in 3D (Melson et al., 2015a) due to the inverse turbulent cascade and the stronger inhibition of Kelvin-Helmholtz instabilities at the interface of supersonic accretion downflows (Müller, 2015). In the SASI-dominated regime, on the other hand, the additional dimension allows the development of the spiral mode (Blondin & Mezzacappa, 2007, Blondin & Shaw, 2007, Fernández, 2010) in 3D, which can store more non-radial kinetic energy than pure sloshing motions in 2D (Hanke et al., 2013, Fernández, 2015), contrary to earlier findings of Iwakami et al. (2008). Such far-reaching differences between 2D and 3D cannot fail to have a significant impact on the GW signal.

While the impact of 3D effects on the GW signals from the post-bounce phase has been investigated before, all available studies have relied on a rather approximate treatment of neutrino heating and cooling such as simple light-bulb models (Müller & Janka, 1997, Kotake et al., 2009; 2011), grey neutrino transport (Fryer et al., 2004, Müller et al., 2012a), or a partial implementation of the isotropic diffusion source approximation of Liebendörfer et al. (2009) in the works of Scheidegger et al. (2008; 2010), which were also limited to the early post-bounce phase. Arguably, none of these previous studies have as yet probed precisely the regimes encountered by the best current 3D simulations (e.g. the emergence of a strong SASI spiral mode) and therefore cannot be relied upon for quantitative predictions of GW amplitudes and spectra, which are extremely sensitive to the nature of hydrodynamic instabilities, the neutrino heating, and the contraction of the PNS.

In this paper, we present GW waveforms of the first few hundred milliseconds of the post-bounce phase computed from 3D models with multi-group neutrino transport. Waveforms have been analysed for four supernova models of progenitors with zero-age main sequence (ZAMS) masses of $11.2M_{\odot}$, $20M_{\odot}$ (for which we study an exploding and a non-exploding simulation), and $27M_{\odot}$. With four simulations based on these three different progenitors, we cover both the convective regime ($11.2M_{\odot}$) and the SASI-dominated regime ($20M_{\odot}$, $27M_{\odot}$). Our aim in studying waveforms from these progenitors is twofold: On the one hand, we shall attempt to unearth the underlying hydrodynamical phenomena responsible for the GW emission in different regions of the frequency spectrum during different phases of the evolution. We shall also compare the GW emission in 3D and 2D models, which will further illuminate dynamical differences between 2D and 3D. Furthermore, with 3D models now at hand, we are in a position to better assess the detectability of GWs from the post-bounce phase in present and future instruments than with 2D models affected by

the artificial constraint of axisymmetry.

One of our key findings is that the GW signal from SASI-dominated models is clearly differentiated from convection-dominated model by strong emission in a low-frequency band around 100...200 Hz. Very recently, Kuroda et al. (2016) also studied the GW signal features (in models using grey neutrino transport) during phases of SASI activity for a $15M_{\odot}$ star, comparing results for three different nuclear equations of state. Going beyond Kuroda et al. (2016), we clarify why this signature has not been seen in 2D models and point out that the hydrodynamic processes underlying this low-frequency signal are quite complex and seem to require a coupling of SASI motions to deeper layers inside the PNS. Moreover, we show that broadband low-frequency GW emission can also occur after the onset of the explosion and is therefore not an unambiguous signature of the SASI. We also provide a more critical assessment of the detectability of this new signal component, suggesting that it may only be detectable with second-generation instruments like Advanced LIGO for a very nearby event at a distance of 2 kpc or less.

Our paper is structured as follows: We first give a brief description of the numerical setup and the extraction of GWs in Section 5.2. In Section 5.3, we present a short overview of the GW waveforms and then analyse the hydrodynamical processes contributing to different parts of the spectrum in detail. We also compare our results to recent studies based on 2D first-principle models. In Section 5.4, we discuss the detectability of the predicted GW signal from our three progenitors by Advanced LIGO (The LIGO Scientific Collaboration et al., 2015), and by the Einstein Telescope (Sathyaprakash et al., 2012) as next-generation instrument. We also comment on possible inferences from a prospective GW detection. Our conclusions and a summary of open questions for future research are presented in Section 5.5.

5.2 Setup and Numerical Methods

5.2.1 Numerical Methods

In this paper, we present and analyse the gravitational-wave signals from three 3D supernova simulations and one 2D supernova simulation. The simulations were performed with the Prometheus-Vertex code (Rampp & Janka, 2002, Buras et al., 2006a). The Newtonian hydrodynamics module PROMETHEUS (Müller et al., 1991, Fryxell et al., 1991) features a dimensionally-split implementation of the piecewise parabolic method of Colella & Woodward (1984) in spherical polar coordinates (r, θ, φ) . Self-gravity is treated using the monopole approximation and the effects of general relativity are accounted for in an approximate fashion by means of a pseudo-relativistic effective potential (case A of Marek et al. 2006). The neutrino transport module VERTEX (Rampp & Janka, 2002) solves the energy-dependent two-moment equations for three

neutrino species (ν_e , $\bar{\nu}_e$, and a species ν_X representing all heavy flavor neutrinos) using a variable Eddington factor technique. The “ray-by-ray-plus” approximation of Buras et al. (2006a) is applied to make the multi-D transport problem tractable. In the high-density regime, the nuclear equation of state (EoS) of Lattimer & Swesty (1991) with a bulk incompressibility modulus of nuclear matter of $K = 220$ MeV has been used in all cases. An initial grid resolution of $400 \times 88 \times 176$ zones in r , θ , and φ was used for the 3D model, and more radial grid zones were added during the simulations to maintain sufficient resolution around the PNS surface. **For the 2D model an initial grid resolution of 400×88 zones in r and θ was used. In both 2D and 3D, the innermost 10 km was simulated in spherical symmetry to avoid excessive limitations on the time step.**

In order to compare our results to previous 2D results, we also reanalyse the 2D model presented by Müller et al. 2013. This model was simulated with CoCoNuT-Vertex (Müller et al., 2010). CoCoNuT (Dimmelmeier et al., 2002; 2005) uses a directionally-unsplitted implementation of the piecewise parabolic reconstruction method in spherical polar coordinates. The general relativistic equations of hydrodynamics are solved in the extended conformal flatness approximation (Cordero-Carrión et al., 2009). The general relativistic 2D model was simulated with an initial grid resolution of 400×128 zones in r and θ was used. The innermost 1.6 km was simulated in spherical symmetry to time step limitations.

5.3 Structure and Origin of the Gravitational Wave Signal

The different 3D models used in our analysis probe distinctly different regimes that can be encountered in supernova cores. In this section, we will investigate how these dynamical differences are reflected in the GW signals.

5.3.1 Supernova Models

We study four 3D models based on three solar-metallicity progenitor stars with ZAMS masses of $11.2M_\odot$ (Woosley et al., 2002), $20M_\odot$ (Woosley & Heger, 2007) and $27M_\odot$ (Woosley et al., 2002):

- **s11.2:** Model s11.2 (Tamborra et al., 2014b) is based on the solar-metallicity $11.2M_\odot$ progenitor of Woosley et al. (2002). This model exhibits transient shock expansion after the infall of the Si/O shell interface, but falls slightly short of an explosive runaway. After the average shock radius reaches a maximum of ≈ 250 km at a time of ≈ 200 ms after bounce, the shock recedes and shock revival is not achieved by the

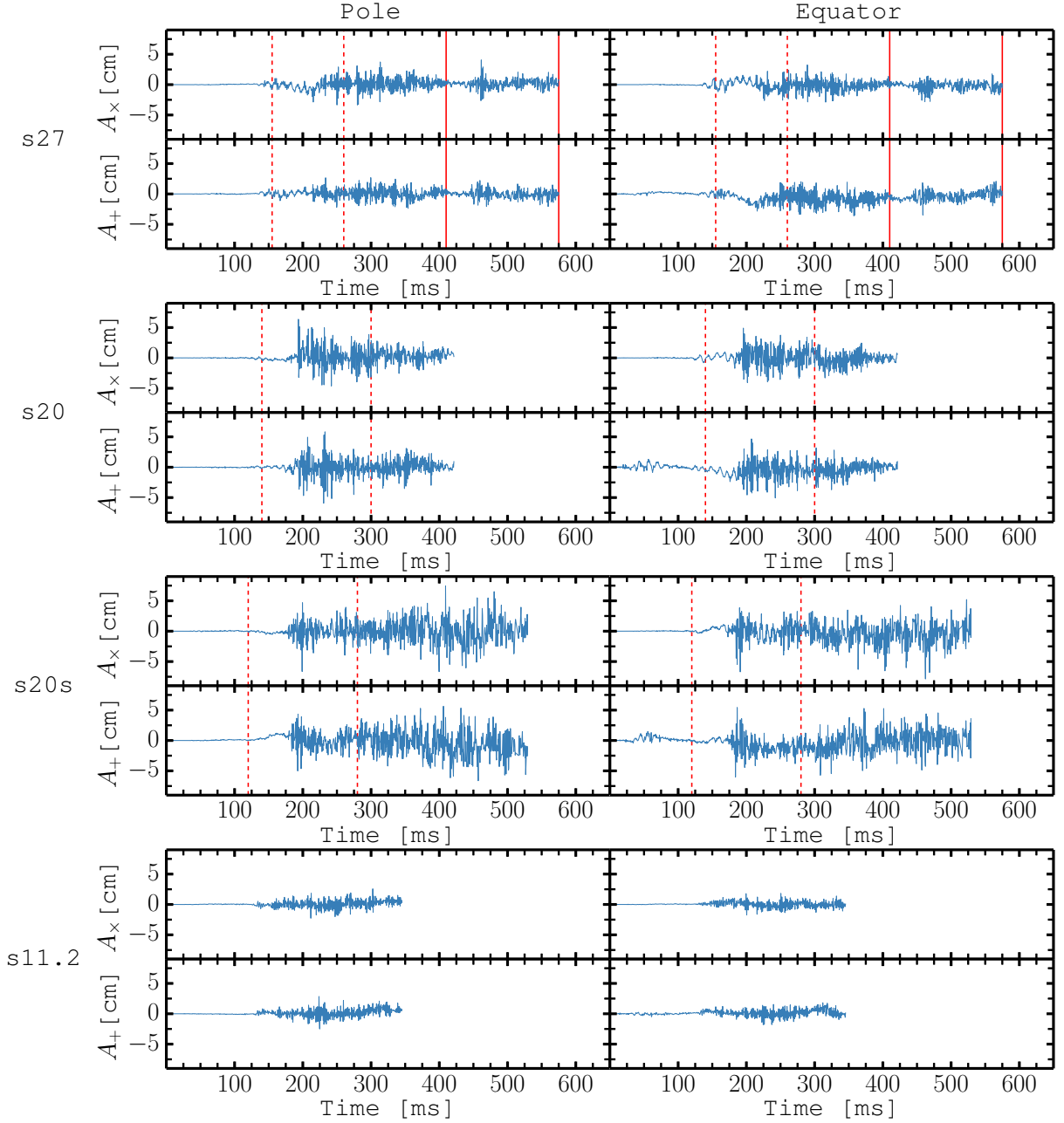


Figure 5.1: GW amplitudes A_+ and A_x as functions of time after core bounce. From the top: s27, s20, s20s, and s11, respectively. The two columns show the amplitudes for two different viewing angles: an observer situated along the z -axis (pole; left) and an other observer along the x -axis (equator; right) of the computational grid, respectively. Episodes of strong SASI activity occur between the vertical red lines; dashed and solid lines are used for model s27 to distinguish between two different SASI episodes.

end of the simulation 352 ms after core bounce. The post-shock region is dominated by buoyancy-driven convection; because of the large shock radius no growth of the SASI is observed. The convective bubbles remain of moderate scale: Even during the phase of strongest shock expansion around ~ 200 ms after bounce when the shock deformation is most pronounced and the kinetic energy in convection motions reaches its peak value, the bubbles subtend angles of no more than $\lesssim 60^\circ$.

- **s20:** Model s20 is based on the $20M_\odot$ solar-metallicity progenitor of Woosley & Heger (2007) and has been discussed in greater detail in Tamborra et al. (2013; 2014a), where quasi-periodic modulations of the neutrino emission were analysed and traced back to SASI-induced variations of the mass-accretion flow to the PNS. No explosion is observed by the end of the simulation 421 ms post bounce. There is an extended phase of strong SASI activity (dominated by the spiral mode) between 120 and 280 ms after core bounce. After a period of transient shock expansion following the infall of the Si/O shell interface, SASI activity continues, but the kinetic energy in the SASI remains considerably smaller than during its peak between 200 and 250 ms.
- **s20s:** This model is based on the same $20M_\odot$ progenitor as s20, but a non-zero contribution from strange quarks to the axial-vector coupling constant, $g_a^s = -0.2$, from neutral-current neutrino-nucleon scattering was assumed (Melson et al., 2015b). This modification of the neutrino interaction rates results in a successful explosion (Melson et al., 2015b). Shock revival sets in around 300 ms after bounce. Prior to shock revival, the post-shock flow is dominated by large-scale SASI sloshing motions between 120 and 280 ms post-bounce. By the end of the simulation 528 ms post-bounce, the average shock radius is ≈ 1000 km, and a strong global asymmetry stemming from earlier SASI activity remains imprinted onto the post-shock flow. Asymmetric accretion onto the PNS still continues, but the accretion rate is reduced by a factor of ~ 2 compared to model s20.
- **s27:** Our most massive model is based on the $27M_\odot$ solar-metallicity progenitor of Woosley et al. (2002) and has been discussed in greater detail in Hanke et al. (2013) and, for SASI-induced neutrino emission variations, by Tamborra et al. (2013; 2014a). Shock revival did not occur by the end of the simulation 575 ms after bounce. There are two episodes of pronounced SASI activity that are interrupted by a phase of transient shock expansion following the infall of the Si/O interface. The first SASI phase takes place between 120 and 260 ms post-bounce and the second period sets in around 410 ms post-bounce and lasts until the end of the simulation.

In addition to the 3D models, we also analyse two 2D models based as the same progenitor as s27. The first 2D model is simulated with the same numerical setup as s27.

- **s27-2D:** The 2D version of s27 is based on the same $27M_\odot$ solar-metallicity progenitor of Woosley et al. (2002) and has been presented in Hanke et al.

(2013). SASI activity sets in about 150 ms after core bounce. Between 220 ms and 240 ms after bounce the accretion rate drops significantly, after the Si/O shell interface reaches shock. The low accretion rate leads to shock expansion and around 300 ms post bounce shock revival occurs.

- **G27-2D:** We also reanalyse the gravitational wave signal from a general relativistic 2D model (Müller et al., 2012c) presented by Müller et al. 2013 and compare our results to this model. This model is based on the same $27M_{\odot}$ solar-metallicity progenitor as s27 and s27-2D (Woosley et al., 2002). An analysis of the gravitational waves from this model can be found in Müller et al. (2013). The model is characterized by strong post-shock convection for the first 50 ms after core bounce. The post-shock convection is followed by a phase of strong SASI activity. Around 120 ms after core bounce the average shock radius starts to steadily increase. The criteria for run away shock expansion is met approximately 180 ms after bounce and ~ 209 ms post bounce the shock has been successfully revived.

5.3.2 Gravitational Wave Extraction

In order to extract the GW signal from the hydrodynamical simulations, we post-process our simulations using the quadrupole stress formula (Finn, 1989, Nakamura & Oohara, 1989, Blanchet et al., 1990). Here, we only give a concise description of the formalism and refer the reader to Müller et al. (2012a)* for a full explanation.

In this work, we disregard the contribution of anisotropic neutrino emission (Epstein, 1978) to the GW signal. Due to its low-frequency nature, it is of minor relevance for the detectability and does not affect the waveforms appreciably in the frequency range $\gtrsim 50$ Hz that is of primary interest to us in this work.

5.3.3 Overview of Waveforms

Waveforms

Amplitudes for GWs generated by asymmetric mass motions are shown in Fig. 5.1. For each progenitor, we show two panels representing the cross and plus polarisation for two different observer positions. The two columns show the amplitudes for two different viewing angles, the right and left column representing observers situated along the z-axis (pole) and

* Note, however, that the description of the formalism in Müller et al. (2012a) contains some typos: Their Eq. (24) is incomplete. The superscript TT is missing from \ddot{Q}_{ij} , as is also the case in Eq. (22) and (23), and, more importantly, the trace term is missing.

x-axis (equator) of the computational grid, respectively. * Since our (nonrotating) models do not exhibit a signal from a rotational bounce, and since (EoS-dependent) prompt post-shock convection is weak, the waveforms exhibit an initial quiescent phase. This is followed by a rather stochastic phase with amplitudes of several centimetres once convection or the SASI have fully developed. The correlation of stronger GW emission with the onset of strong, non-linear SASI activity in model s20, s20s, and s27 is illustrated by dashed and solid lines bracketing phases of particularly violent SASI oscillations.

The signal from early SASI activity triggered by prompt convection a few tens of milliseconds after bounce, which is typically rather prominent in 2D (Marek et al., 2009, Murphy & Burrows, 2008a, Yakunin et al., 2010, Müller et al., 2013, Yakunin et al., 2015), is thus strongly reduced in 3D. It is only clearly visible in the waveforms of s20 and s20s, while s11.2 and s27 only show traces of this component in some directions. The stochastic modulation of the later signal is reminiscent of 2D models, but the amplitudes are significantly lower ($\lesssim 4$ cm) compared to several tens of cm in first-principle 2D models (Marek et al., 2009, Yakunin et al., 2010, Müller et al., 2013, Yakunin et al., 2015). The reduction in 3D is far stronger than could be expected from a mere projection effect (in agreement with parameterised models of Müller et al. 2012a).

Prior to a post-bounce time of ~ 200 ms, the waveforms for the three SASI-dominated models are clearly dominated by a low-frequency signal (in very much the same fashion as for early SASI activity a few tens of milliseconds after bounce in 2D). This already indicates that the relative importance of the low- and high-frequency components of the signal during the accretion phase is different in 3D compared to 2D, where low-frequency emission (triggered by prompt convection) only dominates for the first tens of milliseconds.

In the exploding model s20s with $g_a^s = -0.2$, we observe a tendency towards somewhat higher peak amplitudes than during the accretion phase well after the onset of the explosion (~ 300 ms). This tendency is, however, much less pronounced than in 2D models. The monotonous “tail” in the matter signal from anisotropic shock expansion (Murphy et al., 2009, Yakunin et al., 2010) is noticeably absent, although no undue importance should be attached to this because it may take several hundreds of milliseconds for the tail to develop (Müller et al., 2013).

Energy Spectra

Time-integrated energy spectra for each of the models are shown in Fig. 5.2. These are computed according to Eq. 2.42.

*In our post-processing we chose to sample the GW signal at observer directions corresponding to cell centres of the simulation grid and as a consequence the two directions do not exactly correspond to the north pole ($\theta = 0, \phi = 0$) and the equator ($\theta = \pi, \phi = 0$), but are offset by half of the angular resolution. Hence, the coordinates of the polar and equatorial observer become $(\pi/176, \pi/176)$ and $(\pi - \pi/176, \pi/176)$, respectively.

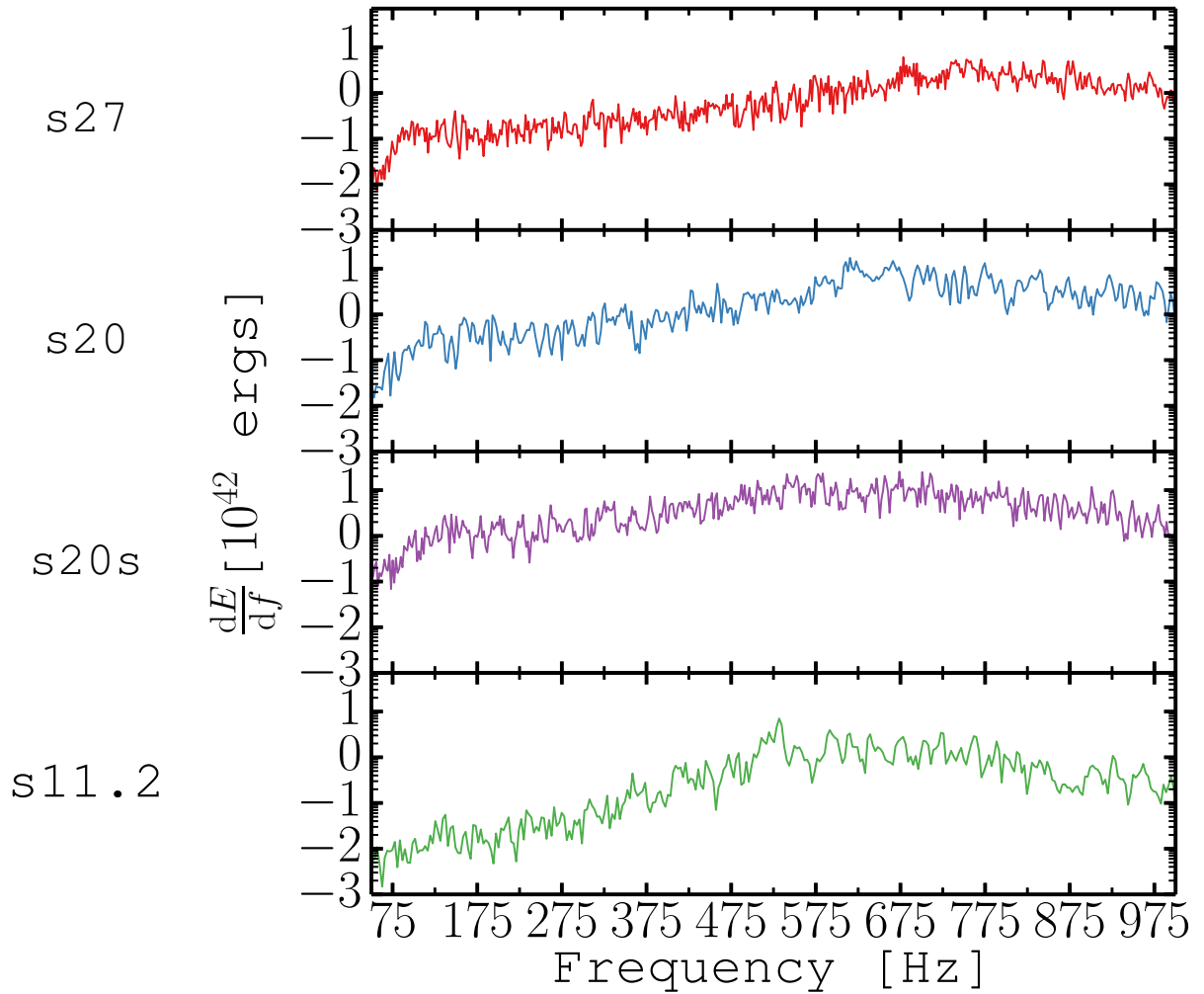


Figure 5.2: Time-integrated GW energy spectra dE/df for models s27, s20, s11.2, and s20s (top to bottom). The spectra are computed from the Fourier transform of the entire waveform without applying a window function. The y-axis is given in a logarithmic scale.

Model m15fr shows a rather flat spectrum, with strong emission over a wide range of frequencies, but the model has a clear peak around $\sim 75 - 100$ Hz. The slower rotating model m15r, which does not develop strong SASI oscillations, peak is visible in the more slowly rotating model m15r. The peak is, however, much weaker.

The Signal in the Time-Frequency Domain

In order to dissect the signal further, we apply a short-time Fourier transform (STFT) to our waveforms. For a discrete time series the STFT is obtained by applying the discrete Fourier transform (DFT) to the signal with a sliding window. In this work, we define the DFT, \tilde{X}_k , as follows:

$$\tilde{X}_k(f_k) = \frac{1}{M} \sum_{m=1}^M x_m e^{-2\pi i k m / N}, \quad (5.1)$$

Here, x_m is the time series obtained by sampling the underlying continuous signal at M discrete times. $f_k = k/T$ is the frequency of bin k , where T is the duration of the signal.

The resulting amplitude spectrograms for a sliding window of 50 ms are shown in Fig. 5.3. The spectrograms show the sum of the squared Fourier components of the cross and plus polarisation modes, $|\tilde{A}_+|^2 + |\tilde{A}_\times|^2$. Before applying the DFT we convolve the signal with a Kaiser window with shape parameter $\beta = 2.5$. Frequencies below 50 Hz and above 1100 Hz are filtered out of the resulting DFT. The amplitude spectrograms are computed for the same two observer directions as before.

All of the models exhibit the distinct high-frequency (here defined to be emission at frequencies greater than 250 Hz) component familiar from 2D models with a slow, secular increase in the peak frequency.

The SASI-dominated models stand apart from model s11.2 in that they show an additional low-frequency component (below 250 Hz) at late times (i.e. *not* associated with prompt convection). No such distinct low-frequency emission has been observed in spectrograms from 2D models (Murphy et al., 2009, Müller et al., 2013). The low-frequency component is clearly separated from the high-frequency emission by a “quiet zone” in the spectrograms. The frequency structure of the low-frequency component is rather complicated, and especially for models s20 and s20s it is rather broad-banded. There is also a directional dependence as can be seen, for example, from the later onset of low-frequency emission in the polar direction compared to the equatorial direction, in model s20 (second row in Fig. 5.3).

During the explosion phase, we find increased power in the high-frequency band corresponding to the increased peak amplitudes discussed in Section 5.3.3. However, the most conspicuous change after the onset of the explosion consists in a considerable increase of broadband power at low frequencies. Close inspection of Fig. 5.1 shows that the enhanced

low-frequency emission can also be seen directly in the amplitudes: The amplitude “band” defined by stochastic high-frequency oscillations is clearly not centred at zero amplitude, but exhibits a significant low-frequency modulation.

Typical frequencies of the order of 100 Hz as well as a vague temporal correlation of the low-frequency emission with periods of strong sloshing/spiral motions suggest a connection with SASI activity. However, model s27 (top row in Fig. 5.3) also shows low-frequency emission during the phase between 280 ms and 350 ms after bounce when the SASI is relatively quiet. If the signal were directly due to the SASI, one would expect the phases of strong SASI and strong low-frequency emission to coincide. There may also be correlations between the low- and high-frequency emission as suggested by the fact that model s20 with the strongest low-frequency emission also exhibits the strongest high-frequency signal. Moreover, the source of enhanced low-frequency emission after shock revival is not immediately intuitive since the SASI no longer operates during this phase. This calls for a closer investigation of the hydrodynamic processes responsible for the emission of the two signal components.

5.3.4 Spatial Location of Underlying Hydrodynamical Instabilities

Which regions of the simulation volume contribute to the different GW components? The emission of GWs cannot be strictly localised, but one can nonetheless still partition the computational volume in the quadrupole formula (??) into different regions, and consider the formal contributions of each of these to the total signal. While this may not amount to a strict localisation of GW emission as coming from a specific region, such a partitioning nevertheless helps to detect fluid motions with the required temporal and frequency structure to account for different components of the signal.

In this work, we divide the integration volume into three layers A, B, and C (see Fig. 5.4). The PNS is split into two layers, the “convective layer” (layer A) and the convectively stable “surface layer” (layer B). The convectively stable inner core ($r < 10$ km) is not considered in our analysis because it is simulated in spherical symmetry and consequently does not contribute to the GW emission. A third layer (layer C) comprises the region between the outer boundary of the PNS (defined by a density of 10^{10} g cm $^{-3}$) and the outer boundary of the grid. We refer to this region as “post-shock” region because only motions in the post-shock region and the deceleration of matter at the shock effectively contribute to the signal from this layer.

The boundary between layer A and layer B is defined based on a horizontal averaging scheme from the stellar convection literature, see, e.g., Nordlund et al. (2009) and Viallet et al. (2013). We define volume-weighted horizontal averages (denoted by angled brackets) of any quantity X such as velocity, density, or pressure as follows,

$$\langle X \rangle = \frac{\int X d\Omega}{\int d\Omega}. \quad (5.2)$$

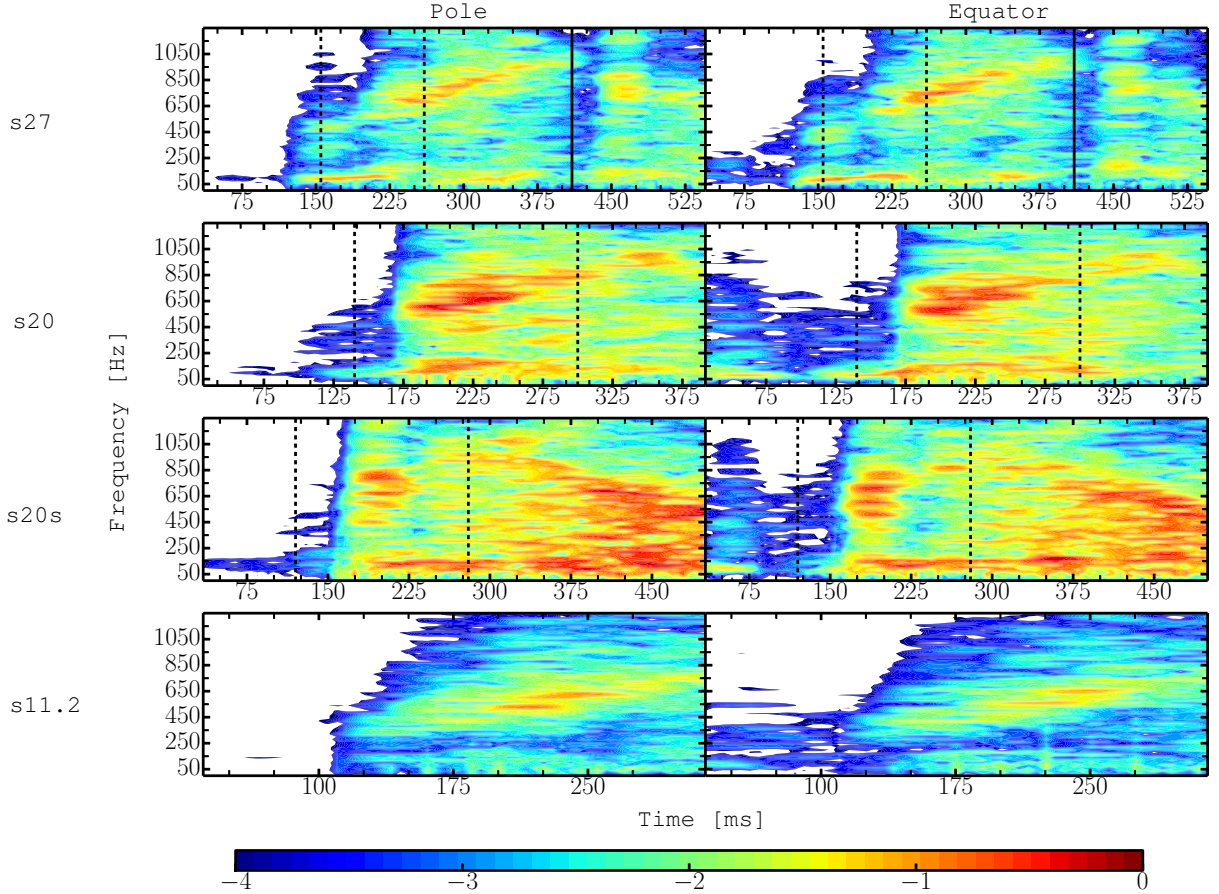


Figure 5.3: Amplitude spectrograms for a sliding window of 50 ms and two different observer directions, summed over the two polarisation modes ($|\tilde{A}_+|^2 + |\tilde{A}_x|^2$). The different rows show the results for models s27, s20, s20s, and s11.2. (top to bottom). The two columns shows the spectrograms for two different viewing angles, the right and left column represent observers situated along the z-axis (pole) and x-axis (equator) of the computational grid, respectively. The time is given in ms after core bounce. Vertical lines bracket SASI episodes. All panels have been normalised by the same global factor. The colour bar is given in a logarithmic scale.

The quantity X is then decomposed into a mean and a fluctuating component,

$$X = \langle X \rangle + X'. \quad (5.3)$$

For defining the boundary between the convective region and the stable surface region, we consider the turbulent mass flux f_m ,

$$f_m = \langle \rho' v'_r \rangle. \quad (5.4)$$

Inside the convective region, heavier fluid is advected downwards while fluid that is lighter than average rises upwards. The turbulent mass flux will, therefore, always be negative in the convective layer. In the overshooting layer outside the PNS convection zone the situation is reversed, and f_m is positive as the overshooting, outward-moving plumes, are denser than their surroundings. In our calculations we include the overshooting region in layer A. To capture properly both the convective zone and the region of overshooting, we define the boundary between layer A and layer B as the radius where

$$f_m = 0.1 f_m^{\max} |_{r > r_{\max}}, \quad (5.5)$$

where f_m^{\max} and r_{\max} are the maximum value of the turbulent mass flux and the radius at which we find f_m^{\max} , respectively. This definition can be more easily understood with the help of a radial profile of f_m as shown in Fig. 5.5 for model s27 at a post-bounce time of 192 ms. Where necessary, we further distinguish between the convective layer (layer A1) and the overshooting layer (layer A2), which are separated by the radius where $f_m = 0$.

In Fig. 5.6 we plot the Fourier amplitudes of the GW amplitudes arising from each individual layer; these amplitudes are calculated from the full-time signal and for an observer situated at the pole, corresponding to the left column in Fig. 5.3. This figure has to be analysed with some care. Since we plot the square of the Fourier coefficients one can not add the values of layers A, B, and C together and recover the value for the total signal. In addition, artefacts can arise due to effects at the boundaries between layers, as in the case of model s20 (top right panel of Fig. 5.6). There is an artificially strong peak at 160 Hz, particularly from layer B. We have confirmed that shifting the boundary between layers A and B inwards reduces this peak significantly. The exact values of the low-frequency amplitudes are sensitive to the boundary definition, but the fact that all three layers contribute to emission below 250 Hz is robust. The high-frequency component is less affected by such artefacts since the high-frequency emission is mostly confined to layer A.

The results of this dissection of the contributions to the integral in Eq. (??) are somewhat unexpected. The high-frequency emission mostly stems from aspherical mass motions in layer A and there is only a minor contribution from layer B, which has been posited as the crucial region for GW emission during the pre-explosion phase in works based on 2D simulations (Marek et al., 2009, Murphy et al., 2009, Müller et al., 2013). Aspherical mass motions in layer C hardly contribute to this component at all.

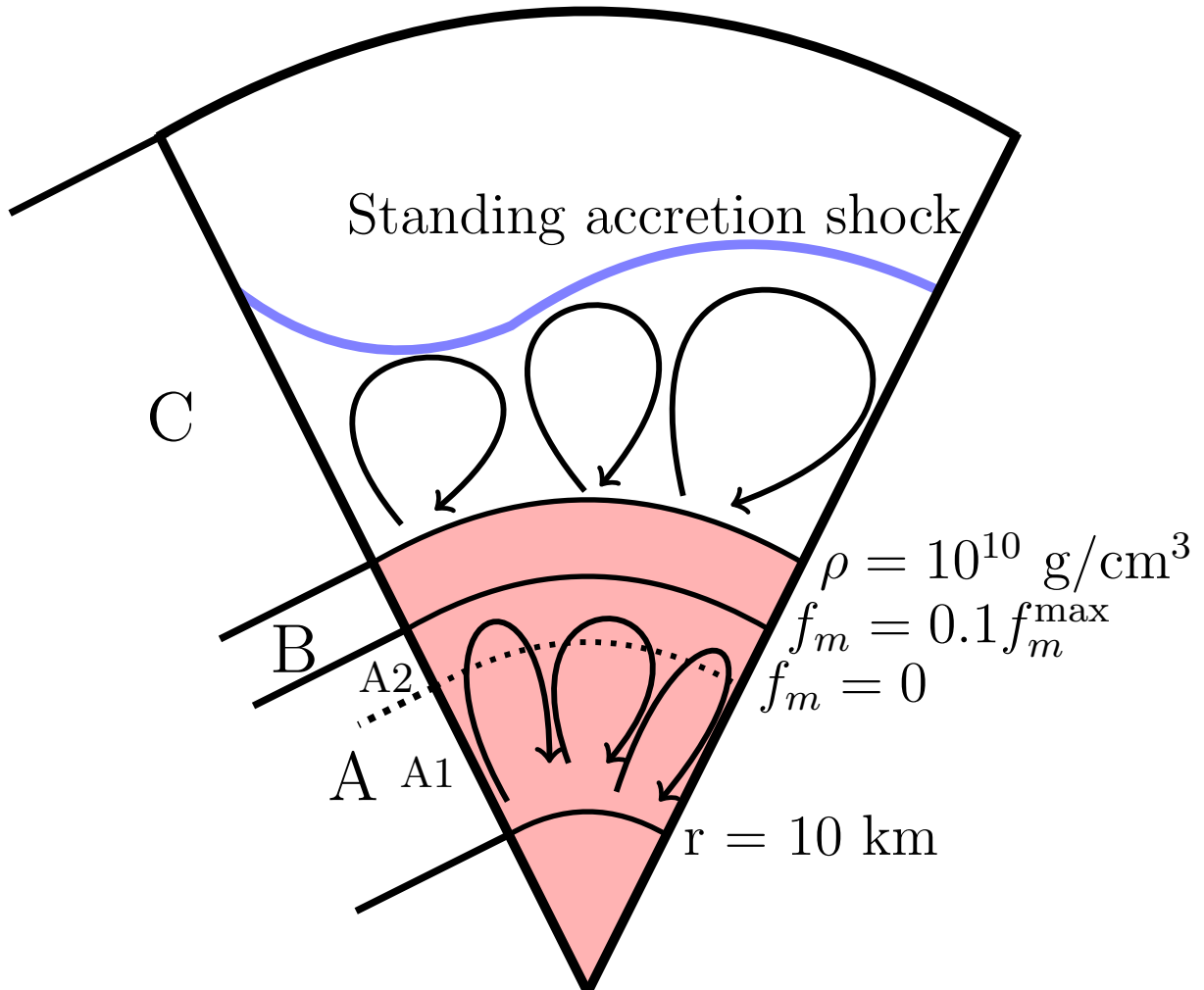


Figure 5.4: Schematic overview of the regions of hydrodynamical activity. In Section 5.3.4 we investigate the contribution to the total GW signal from three different layers. The PNS, indicated by the shaded red area, is divided into two layers: Layer A includes the convectively unstable region in the PNS (layer A1) and the overshooting layer A2 directly above it. The boundary between the convective layer and the overshooting layer is indicated by a dashed curve within layer A. The second layer, layer B, extends from the top of the overshooting region and out to the PNS surface, defined by a fiducial density of $10^{10} \text{ g cm}^{-3}$. Layer C extends from the PNS surface to the outer boundary of our simulation volume. Layer C therefore includes the post-shock region, the standing accretion shock (indicated by the blue line), and the pre-shock region. Formal definitions of the boundaries between layers are given on the right hand side, see Section 5.3.4 for details.

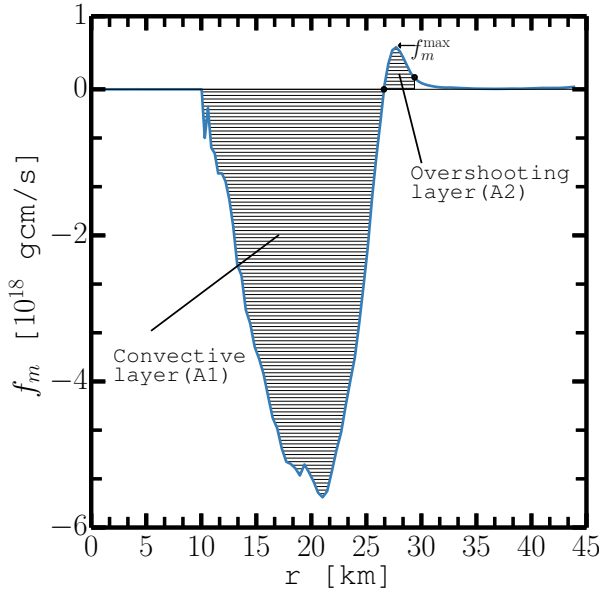


Figure 5.5: Turbulent mass flux f_m (blue curve) for model s27, calculated 192 ms after core bounce. The shaded region indicates the convectively unstable region and the overshooting layer, which are lumped together as layer A (see Fig. 5.4).

By contrast, *all three regions* contribute to the low-frequency signal (i.e. emission at frequencies lower than 250 Hz) to a similar degree. This is also surprising if the dominant frequency of this component appears to be set by the SASI as speculated before. In this case, one might expect that the fluid motions responsible for GW emission are propagating waves in layer C and perhaps layer B, where the conversion of vorticity perturbations into acoustic perturbations occurs in the SASI feedback cycle.

5.3.5 Origin of High-Frequency Emission

What do these findings imply about the physical mechanisms that give rise to GW emission and determine their frequency? Let us first address the high-frequency signal. Recent 2D studies have connected GW emission at $\gtrsim 500$ Hz to oscillatory modes (g-modes) excited either in the PNS surface (layer B) from above by downflows impinging onto the PNS (Marek et al., 2009, Murphy et al., 2009, Müller et al., 2013), or from below by PNS convection (Marek et al., 2009, Müller et al., 2012a; 2013). Prior to shock revival, the excitation of oscillations by mass motions in the gain layer was found to be dominant, with PNS convection taking over as the dominant excitation mechanism only after the onset of the explosion (Müller et al., 2012a; 2013). The typical angular frequency of such processes is roughly given by the Brunt-Väisälä frequency, N , in the convectively stable

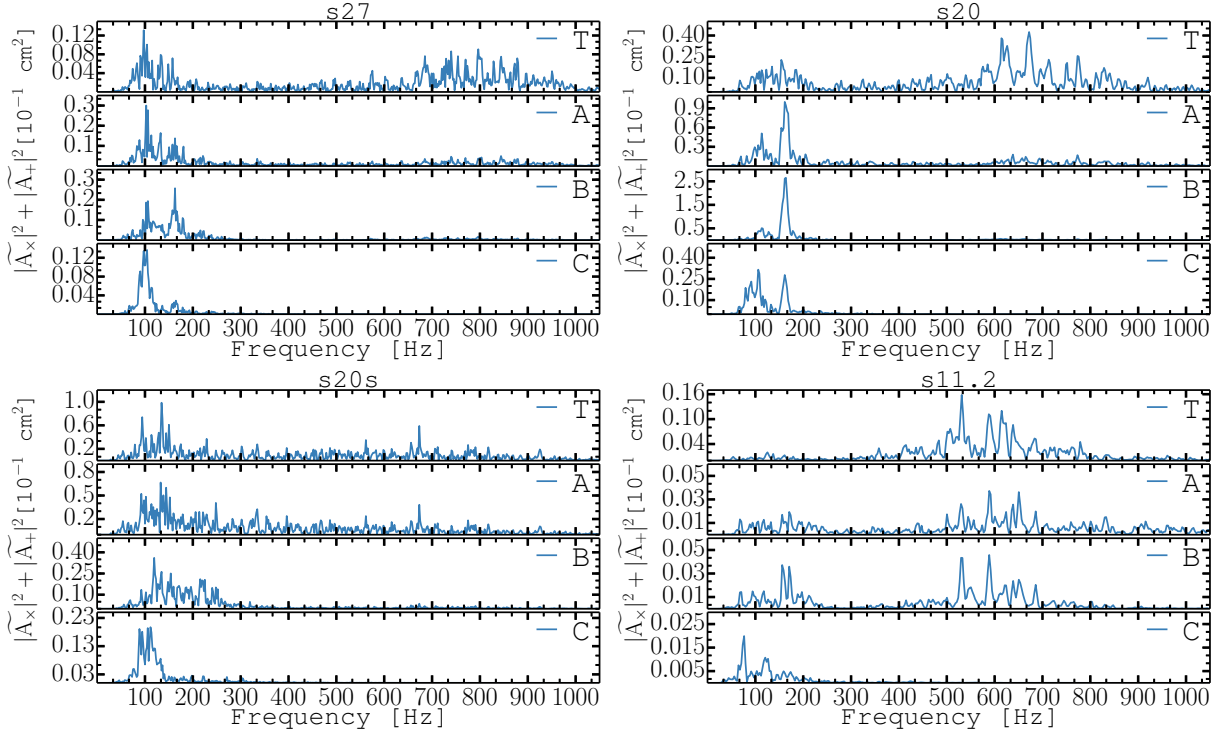


Figure 5.6: Squared Fourier amplitudes of the total volume-integrated GW signal and of the signal contributions arising from the three different layers of the simulation volume. From the top: Total signal (T), the PNS convective region and the overshooting layer (A), the PNS surface layer (B), and the volume between the PNS surface and the outer grid boundary (C). Top row: the left and right columns show the results for models s27 and s20, respectively. Bottom row: the left and right columns show the results for models s20s and s11.2. See Fig. 5.4 for a sketch of the three regions used for this analysis. The Fourier amplitudes are calculated according to Eq. (5.1), Eq. (??) and Eq. (??).

region between the gain region and the PNS convection zone,

$$N^2 = \frac{1}{\rho} \frac{\partial \Phi}{\partial r} \left[\frac{1}{c_s^2} \frac{\partial P}{\partial r} - \frac{\partial \rho}{\partial r} \right], \quad (5.6)$$

where c_s is the sound speed. Müller et al. (2013) further investigated the dependence of this frequency on the mass M , the radius R , and the surface temperature T of the PNS to explain the secular increase of N during the contraction of the PNS and a tendency towards higher frequencies for more massive neutron stars.

Our results confirm that the peak frequency of the high-frequency GW emission is still set by the Brunt-Väissälä frequency in 3D and therefore point to a similar role of buoyancy forces in determining the spectral structure of the high-frequency component. As shown in Fig. 5.7 for model s27, we find very good agreement between the peak GW frequency, f_{peak} ,

and the Brunt-Väisälä frequency, N , calculated at the outer boundary of the overshooting layer (the boundary between layers A and B). Here, f_{peak} denotes the frequency with the highest Fourier amplitude above 250 Hz. Superficially, there appears to be a discrepancy at post-bounce times later than 400 ms, where f_{peak} seems to decrease again. This, however, is purely an artefact of the sampling rate of 0.5 ms in the simulations, which results in a Nyquist frequency of 1000 Hz. The peak frequency is therefore aliased into the region below 1000 Hz. If this is taken into account, there is in fact good agreement between the Brunt-Väisälä frequency of ~ 1300 Hz and the aliased peak GW frequency of ~ 700 Hz at the end of the simulation.

The dominant excitation mechanism for these oscillatory motions in layers A and B is, however, remarkably different from previous 2D models. While allowing for a minor contribution from PNS convection to the total signal during the pre-explosion phase, most of the signal in 2D is found to originate from oscillations in layer B that are excited by convective plumes and/or the downflows of the SASI (Marek et al., 2009, Murphy et al., 2009, Müller et al., 2013). In this case, one would expect that the excited oscillation modes have large amplitudes mostly in the surface layer and that this layer contributes significantly to the GW signal. This is not the case in 3D as shown by Fig. 5.6. The dominant contribution from layer A rather suggests that oscillatory modes are predominantly excited from below by aspherical mass motions in the PNS convection zone and are confined mostly to the overshooting layer, which acts as frequency stabiliser.

To confirm the crucial role of layer A2, we excluded this region from our analysis and found a large reduction of the energy carried away by high-frequency GWs,

$$E_{\text{GW}} \sim \int_{250 \text{ Hz}}^{1100 \text{ Hz}} \frac{dE}{df} df. \quad (5.7)$$

For model s27, we find a reduction of the GW energy by roughly a factor of two when excluding the overshooting layer A2. It is remarkable that the deeper regions of the PNS convection zone (layer A1) nonetheless contribute to the high-frequency signal with similar frequencies: There is no apparent reason for a correlation between the convective overturn time T_{conv} (which sets the natural frequency for GWs from the bulk of the PNS convection zone as $1/T_{\text{conv}}$) and the Brunt-Väisälä frequency in the overlying stable region.

5.3.6 Comparison of high-frequency emission in 2D and 3D

To further illustrate the differences between previously published 2D waveforms and our 3D results, we re-analyse the GW signal from model G27 (G27-2D) of Müller et al. (2013) using the STFT and the decomposition of the computational volume into three different regions. G27-2D is a 2D model based on the same $27M_{\odot}$ progenitor used in our simulations, with the same equation of state and the same neutrino treatment, the only major difference being the treatment of GR: In G27-2D, the equations of radiation hydrodynamics in the

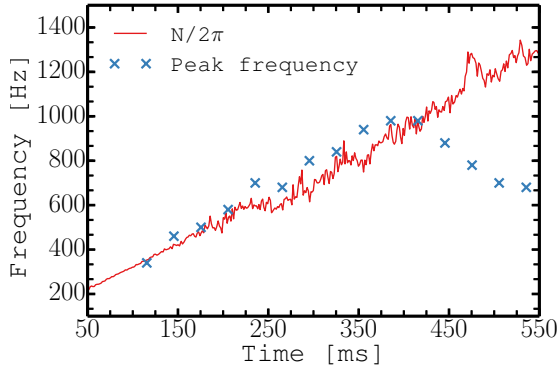


Figure 5.7: Frequency of strongest GW emission above 250 Hz in the spectrogram of model s27 as a function of time (blue crosses). We also plot the expected characteristic frequency of GW emission excited by buoyancy effects in the PNS surface layer B and the overshooting layer A2 (red curve, see definition in Eq. (5.6)). The exact value of N depends on the radius where Eq. (5.6) is evaluated, but we find similar numerical values within layers B and A2. Note that the trends seen for model s27 are common to all our models.

ray-by-ray-plus approximation are solved in their general relativistic formulation assuming a conformally flat metric, whereas the pseudo-Newtonian approach of Marek et al. (2006) was used for model s27 in 3D. The bottom row of Fig. 5.8 shows the GW signal and amplitude spectrogram for model G27-2D. Fourier amplitudes for the signal from the three regions are shown in right panel of Fig. 5.9.

Comparing the spectrograms of model G27-2D with those of the 3D models (Figs. 5.3 and 5.8), we find that the “quiet zone” between the high-frequency and low-frequency components of the signal is not present in model G27-2D, which is in agreement with the wavelet analysis of Müller et al. (2013) who also found a more broad-banded signal during phases of strong SASI and convection, with the Brunt-Väisälä frequency providing more of an upper limit rather than a sharply defined peak frequency during such phases. In model G27-2D, there is strong emission between 250 Hz and 750 Hz, and the relative contribution of the low-frequency signal below 250 Hz is smaller (which will be discussed in more detail in Section 5.3.7). The decomposition of the integration volume into three layers (Left panel of Fig. 5.9) reveals that the main contribution to the high-frequency signal stems from the PNS surface (layer B). In addition to the broadband emission between 250 Hz and 750 Hz, there are also two narrow emission peaks centred around 800 Hz and 900 Hz. This emission is the result of oscillations deep in the PNS core that are excited by PNS convection.

Compared to model G27-2D and other recent 2D models found in the literature (Marek et al., 2009, Murphy et al., 2009, Müller et al., 2013) a 2D version of model s27 (s27-2D) more closely resembles the 3D models presented in our study. Model s27-2D was simulated by Hanke et al. (2013) with Prometheus-Vertex. The spectrogram of model s27-2D (top left panel of Fig. 5.8) show

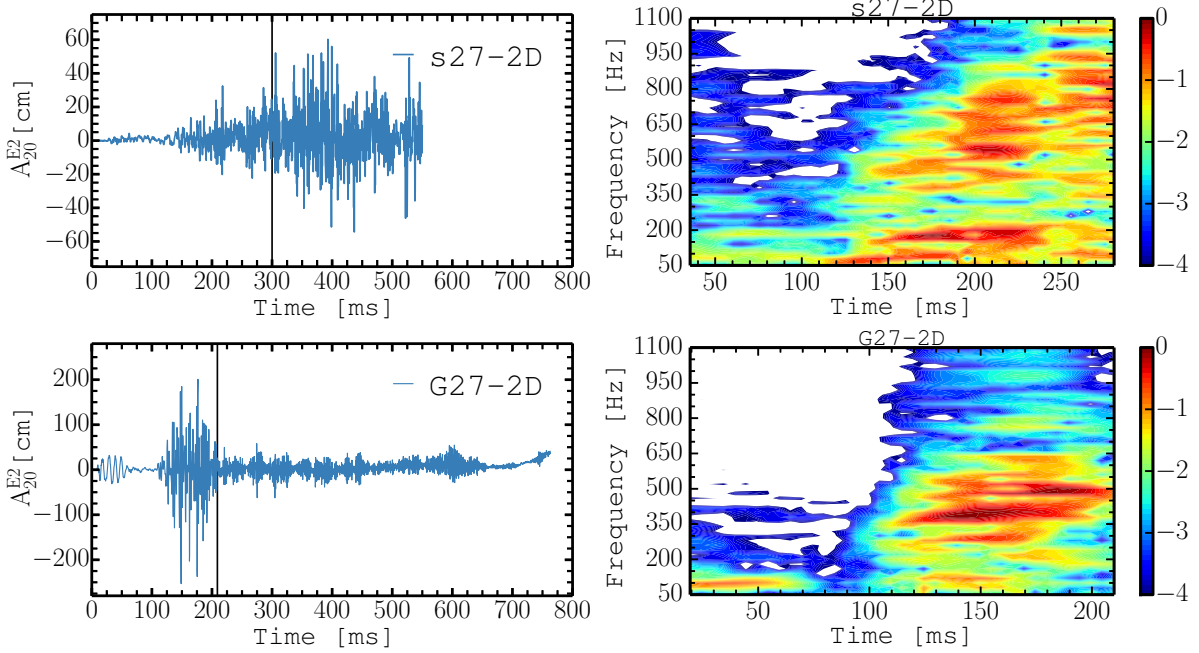


Figure 5.8: The GW amplitude, A_{E2}^{20} , as a function of time after bounce (left) and amplitude spectrograms in logarithmic scale (right) for the two 2D models s27-2D (top row) and G27-2D (bottom row). For a useful comparison with the corresponding non-exploding 3D model, we only show the spectrograms for the time between bounce and the onset of the explosion.

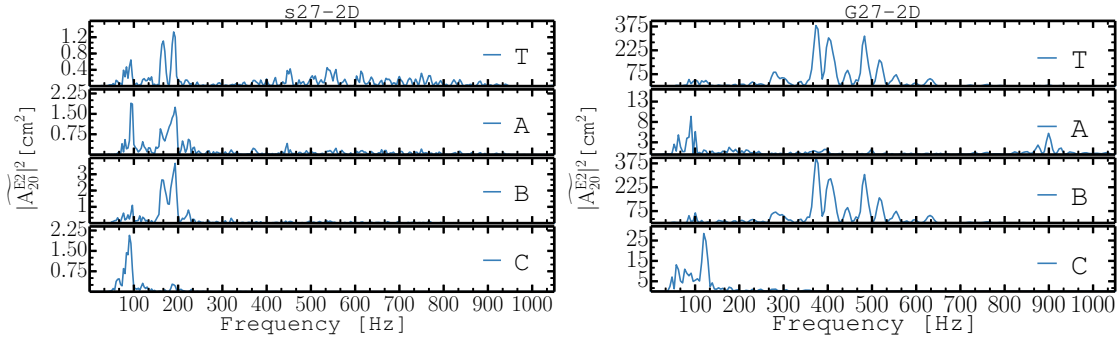


Figure 5.9: Squared Fourier amplitudes of the total volume-integrated GW signal and of the signal arising from the three different layers of the simulation volume, for the 2D model G27-2D of Müller et al. (2013) (right) and s27-2D (left). From the top: total signal (T), layer A, layer B, and layer C. The Fourier amplitudes, $\widetilde{|A_{E2}^{20}|^2}$, are calculated based on Eq. (5.1) and Eq. (2.40).

the same two signal components as we found in our 3D models. There is a high-frequency, a low-frequency component, and a frequency band where the emission is much weaker (between 250 and 350 Hz) separating the two components. The relative contributions, to the total signal, from layer A, B, and C are roughly the same in model s27 and s27-2D, see the left panel of Fig. 5.9 and the top left panel of Fig. 5.6. The most noteworthy difference between models s27 and s27-2D is an all over reduction of the GW signal when going from 2D to 3D. The signal strength is about 10 times greater in model s27-2D than in s27.

There are presumably several reasons why the excitation of oscillations in the PNS surface layer is more efficient **G27-2D (and other recent 2D studies) than in 3D**. First, the inverse turbulent cascade (Kraichnan, 1967) and the suppression of the Kelvin-Helmholtz instability at the edge of supersonic downflows (see Müller 2015 and references therein) lead to an artificial accumulation of the turbulent energy on large scales in 2D supernova simulations (Hanke et al., 2012, Abdikamalov et al., 2015) and higher impact velocities of the downflows (Melson et al., 2015a, Müller, 2015). Thus, both the amplitudes as well as the mode overlap of the forcing with the excited $l = 2$ oscillation modes are higher in 2D. However, while the excitation of g-modes in the surface layer is strongly suppressed in 3D, there is still some residual g-mode activity (Melson et al., 2015a, Müller, 2015). To fully understand the absence of high-frequency emission from the surface layer, we must also consider the frequency structure of the forcing. Fig. 5.10 shows considerable high-frequency emission from layer C in 2D, which is indicative of violent large-scale (i.e. with an $l = 2$ component) mass motions on time-scales considerably *shorter* than the SASI period or the convective overturn time-scale. The lack of such high-frequency GW activity from layer C in 3D indicates that the downflows in 3D are not as strongly distorted by intermediate-scale eddies and that they vary less on short time-scales. Fig. 4 of Melson et al. (2015a), which shows 2D and 3D simulations of a successfully exploding $9.6M_{\odot}$ model, further illustrates this difference between the frequency structure of the post-shock flow in 2D and 3D: In 3D the angle-averaged radial velocity profiles of the infalling material appear smooth. On the other hand, intermediate-scale eddies with fast time variations are clearly visible in 2D. With a typical time scale on the order of $t \sim 1 \dots 10$ ms, corresponding to a frequency range of $f \sim 100 \dots 1000$ Hz, the eddies in 2D cause a more “impulsive” forcing with a broad frequency spectrum. The different frequency structure of the forcing in 2D and 3D is then reflected in the excited PNS surface oscillations: In 2D, where the frequency spectrum of the forcing overlaps with the natural g-mode frequency, we see *resonant* excitation of free (high-frequency) g-mode oscillations. This is not the case in 3D, but we still see strong *non-resonant* excitation of forced g-modes at low frequencies in the PNS surface (see Section 5.3.7).

One particular aspect of model G27-2D is the very early development of strong SASI activity. Large-scale deformation of the shock already occurs ~ 50 ms after bounce, without a preceding phase of hot-bubble convection (Müller et al., 2013). This is different from

model s27-2D. At early times the average shock radius is \sim 20–30 km larger in model s27-2D than in model G27-2D. Since a larger shock radius favours neutrino-driven convection, model s27-2D shows an initial phase of convection before SASI activity sets in when the shock starts to retract \sim 100–150 ms after bounce. Due to the early development of SASI activity in model G27-2D at a time when the accretion rate is high, particularly strong downflows onto the PNS develop. These downflows effectively perturb the PNS surface (layer B) and excite g-modes that in turn lead to GW emission. On the other hand, in model s27-2D downflows take longer to develop and are weaker, since the accretion rate has decreased by the time they form.

The differences in the post-shock conditions of models G27-2D and s27-2D are reflected in the GW signal (Fig. 5.8). In model s27-2D the high-frequency GW emission from g-modes excited by downflows striking the PNS surface (layer B) is drastically reduced compared to model G27-2D (although it is still roughly as strong as the emission from layer A), and the reduction in emission from layer B leads to an overall decrease of the GW amplitude. Unlike for model G27-2D, we can clearly see a low-frequency component in the amplitude-spectrogram of model s27-2D. This emission component is also present in the GW signal from model G27-2D. In fact, Fig. 5.9 shows GW emission at similar frequencies in layers A and C. However, in model G27-2D this signal component is small compared to the GW emission from the resonantly excited surface g-modes of layer B.

A possible reason for stronger and earlier SASI activity in model G27-2D is that, in contrast to model s27-2D, model G27-2D exhibits a phase of strong *prompt* post-shock convection (between a few ms after bounce and about 50 ms after bounce), which leaves the shock appreciably deformed with $|a_1|/a_0 \sim 0.01 - 0.02$ as shown in Fig. 7 of Müller et al. (2012c). Therefore the SASI amplitude only needs to grow by a factor of \sim 30 to reach the non-linear regime. In Hanke et al. (2013, Fig. 2) the $l = 1$ amplitude is much smaller at early times. Such differences in the post-bounce evolution can have a variety of reasons. Besides the pure stochasticity of simulations, the initial perturbations may also play a role: Model G27-2D was simulated in 2D from the onset of core collapse, while model s27-2D was started from a spherical model with seed perturbations imposed 15 ms after core bounce. The presence or absence of strong prompt post-shock convection also depends on the details of the entropy and electron fraction profiles, which are determined by the exact shock dynamics during the first milliseconds after core bounce. Without a very careful analysis of all the differences between the two simulations, we are not able to localise the origin of the differences between model G27-2D and model s27-2D in the different gravity treatment or any of the other aforementioned aspects.

5.3.7 Origin of the Low-Frequency Signal

The strong low-frequency signal seen in the more massive models (s20, s20s, s27) is apparently closely connected to SASI activity. Note that the convection-dominated s11.2 model

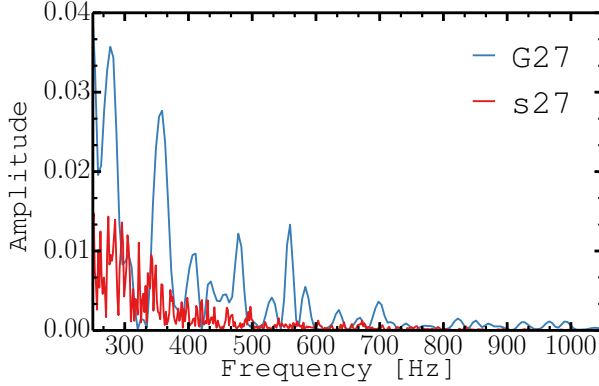


Figure 5.10: Normalised Fourier amplitudes of the GW signal from layer C for the 2D model G27-2D and the 3D model s27. Each curve is normalised by its respective maximum to account for the difference in magnitude between 2D and 3D. Note that the maxima lie outside of the frequency domain shown in this figure.

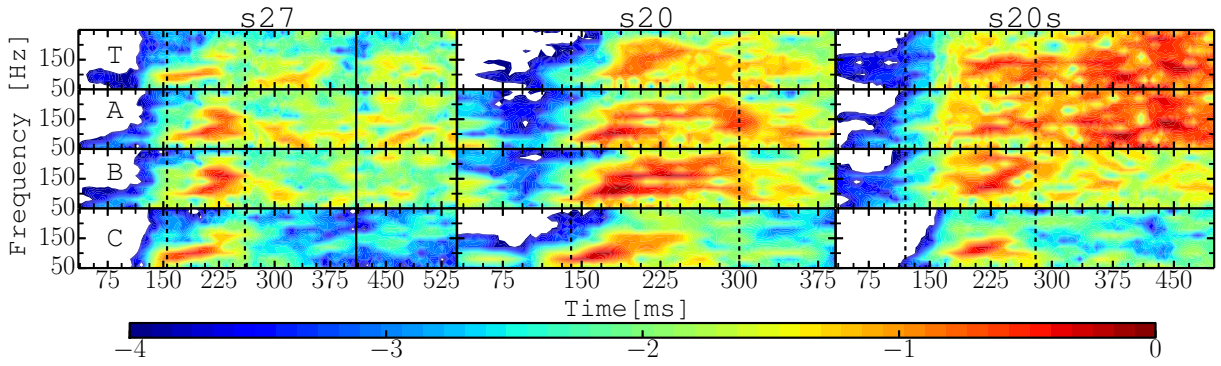


Figure 5.11: Amplitude spectrograms, for a sliding window of 50 ms, of the low-frequency GW signal arising from the three different layers, summed over the two polarisation modes ($|\tilde{A}_+|^2 + |\tilde{A}_\times|^2$). From the top: total signal (T), layers A, B, and C. Columns are ordered by progenitor (left: s27, middle: s20, right: s20s). See Fig. 5.4 for a sketch of the three regions. The observer is chosen to be the north pole in the computational grid. As in Fig. 5.1 and Fig. 5.3, strong SASI episodes are bracketed by vertical lines. The colour scale is logarithmic and all panels have been normalised by the same global factor that has also been used for Fig. 5.3.

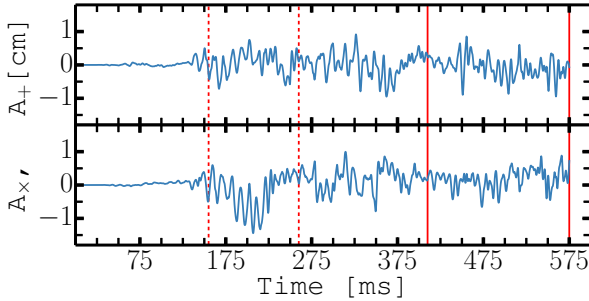


Figure 5.12: The GW amplitudes A_+ and A_x of model s27, for an observer situated along the z-axis of the computational grid, after a low-pass filter has been applied. The time axis indicates time since core bounce.

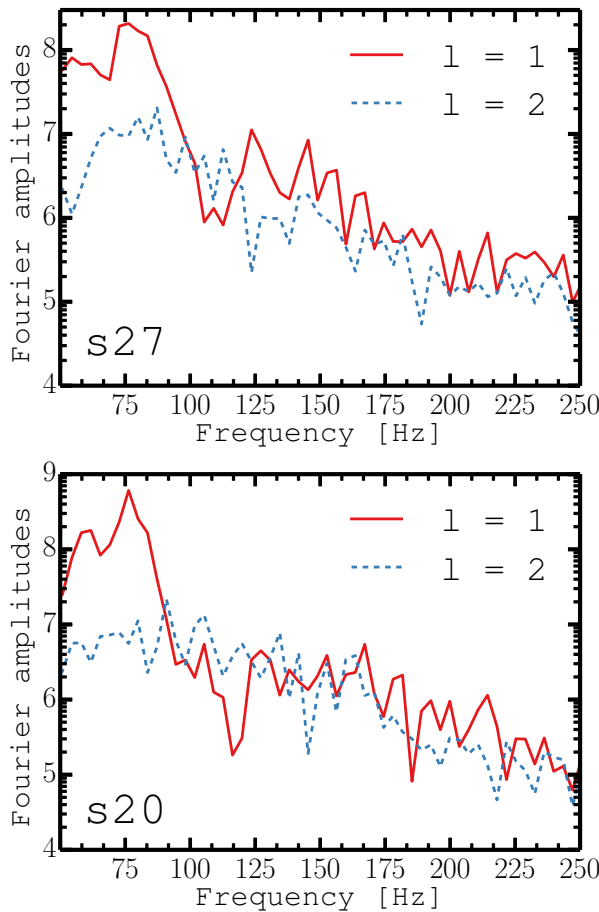


Figure 5.13: Squared Fourier amplitudes, in logarithmic scale, for the $l = 1$ and $l = 2$ components of the expansion of the shock position into spherical harmonics. The Fourier amplitudes have been calculated for the time window between 100 ms and 350 ms after core bounce. The upper panel shows model s27 and the bottom panel the results for model s20. The curves in both panels have been normalised by the same factor.

show some stochastic low-amplitude GW emission at low frequencies (see Fig. 5.3), which is, however, much less pronounced compared to the high-frequency component. To address the origin of the low-frequency component, we show spectrograms of the GW signal below 250 Hz from each of the three analysis regions for models s20, s20s, and s27 in Fig. 5.11.

The apparent temporal correlation of the low-frequency emission with the SASI suggests the following plausible mechanism responsible for this component: Violent SASI involves the development of large-scale, large-amplitude density perturbations with the same temporal dependence as the shock oscillations. Such density perturbations $\delta\rho$ will directly contribute to the signal through the term $\rho x_i \partial_j \Phi$ in the integrand of the quadrupole formula (??) if the density perturbations $\delta\rho$ have an $l = 2$ (quadrupole) component $\delta\rho_2$.^{*} Even $l = 1$ sloshing and spiral motions will develop a sizeable quadrupole component $\delta\rho_2$ in the non-linear phase. The frequency of the emitted signal will trace the frequency of the underlying SASI mode, but with frequency doubling for the $l = 1$ mode since the SASI-induced perturbation of the quadrupole moment will repeat itself after half a period as the integrand in Eq. (??) is invariant to a rotation by π in any direction. The contribution of the $l = 1$ and $l = 2$ modes (and possibly their overtones) explains the double-peak structure of the low-frequency signal in Figs. 5.3, 5.6 and 5.11. The amplitude arising from the term $\rho x_i \partial_j \Phi$ will be of order

$$A \sim \frac{G}{c^4} \int r \delta\rho_2 \frac{\partial\Phi}{\partial r} dV \sim \frac{G}{c^4} \int \delta\rho_2 \frac{GM}{r} dV. \quad (5.8)$$

The integral is essentially the potential energy stored in $l = 2$ density perturbations during SASI oscillations. Equating the potential energy with the kinetic energy in SASI motions and taking into account that there is only a finite overlap with $l = 2$, we find

$$A \lesssim \frac{G}{c^4} E_{\text{kin,SASI}}. \quad (5.9)$$

With $E_{\text{kin,SASI}} \sim 10^{49}$ erg, we obtain $A \lesssim 0.8$ cm, which is roughly compatible with the amplitudes (see Fig. 5.12).

The anisotropic modulation of the accretion by the SASI is further communicated to the PNS as material is advected downwards and settles onto the PNS surface (something which may also be viewed as on-resonant excitation of g-modes far below their eigenfrequency). As matter seeps deeper into the outer layer of the PNS (layer B) and then even further down into the interior of the PNS (layer A), it will still emit GWs if the density and entropy perturbations are not washed out completely by neutrino cooling. We have verified that relatively large density fluctuations on the percent level are maintained even in the cooling region. Since these density fluctuations still retain a temporal modulation set by the SASI, they emit GWs in a similar, albeit somewhat broader frequency range. For the same reasons as detailed above, the GWs amplitudes produced by such a non-resonant excitation

^{*}Velocity perturbations will, in principle, also contribute in Eq. (??). Empirically, we find that their contribution to the GW amplitude is minimal, however.

of g-modes will be related to the kinetic energy stored in the mode and even a small kinetic energy $\gtrsim 10^{48}$ erg in aspherical mass motions below the gain region is sufficient to account for the amplitudes.

The fact that the low-frequency signal from layer C is *weaker* than that from both layer A and layer B is not in conflict with this explanation because of cancellations in the integral of $\rho(v_i v_j - x_i \partial_j \Phi)$ over the region outside the PNS, e.g. the overdensities in the downflows can be compensated by the smaller shock radius above them.* Furthermore, we surmise that density perturbations from the $l = 1$ contribute more strongly to the GW signal as they settle deeper into the PNS, because the pure $l = 1$ angular dependence of the perturbations in the post-shock region develops a larger $l = 2$ component during the process of settling.

The crucial role of the SASI in providing a slow, non-resonant forcing of the outer regions of the PNS is also reflected in the frequency structure of the signal. In Fig. 5.13 we plot the Fourier amplitudes of the $l = 1$ and $l = 2$ components of the spherical harmonics decomposition of the shock position for the period between 100 ms and 350 ms after bounce. More precisely Fig. 5.13 shows

$$\sum_{m=-l,l} |\tilde{a}_l^m(t)|^2 \quad (l = 1, 2), \quad (5.10)$$

where $\tilde{a}_l^m(t)$ is the Fourier transform of

$$a_l^m(t_n) = \frac{(-1)^{|m|}}{\sqrt{4\pi(2l+1)}} \int r_{\text{sh}}(\theta, \phi, t) Y_l^m d\Omega. \quad (5.11)$$

Here, r_{sh} is the shock position (given by the Riemann-solver in our code) and Y_l^m is the spherical harmonic of degree l and order m . Details about the shock can be found in Hanke et al. (2013) for model s27, in Hanke (2014) for models s11.1 and s20 and in Melson et al. (2015b) for model s20s. The typical frequency for the $l = 1$ mode (50...100 Hz) and the $l = 2$ mode (100...160 Hz) of the shock are compatible with the range of low-frequency emission seen in the GW spectrograms, especially if we account for the fact that the GW signal from forced $l = 1$ motion will exhibit frequency doubling.

Since the Fourier spectra of the $l = 1$ and $l = 2$ modes as well as the GW spectrogram point towards a complicated frequency structure with peak frequencies shifting in time (due to the variation of the shock radius which sets the SASI frequencies) and contributions from different phases interfering with each other in the time-integrated spectrum, we refrain from a precise one-to-one identification of the underlying modes.

It is noteworthy that the effect of anisotropic accretion manifests itself even down to the PNS convective layer. Apparently, the eigenfunctions of the excited modes reach down

* Immediately outside the minimum shock radius, the densities of unshocked material above the downflows are *lower* than in the shocked material inside the high-entropy bubbles *at a given radius*, i.e. overdensities behind the shock correspond to underdensities at larger radii.

quite deep through the entire surface of the PNS (layer B). However, the fact that even the deeper region of layer A (below the overshooting region) contributes to low-frequency GW emission suggests that $l = 1$ and $l = 2$ surface motions can trigger convective motions (e.g. by providing density perturbations that are then quickly amplified once they are advected into the convectively unstable region). Contrary to the mirror problem of wave excitation at convective boundaries (Goldreich & Kumar, 1990, Lecoanet & Quataert, 2013), such a coupling between the accretion flow, the surface layer, and the PNS convection has as yet been poorly explored.

While the SASI is particularly effective at generating a modulation of the accretion flow with a sizeable $l = 2$ component, large-scale convective motions in the hot-bubble region can also act as a substitute for the SASI during periods of transient shock expansion (because the typical scale of convective eddies is set by the width of the unstable region, cp. Chandrasekhar, 1961, Foglizzo et al., 2006). The result is a somewhat weaker and less sharply defined low-frequency signal, which is what we observe during the SASI-quiet periods in models s20s, s20, and s27 and also in model s11.2 (cf. Fig. 5.3).

With large-scale fluid motions in the gain region as the ultimate agent responsible for low-frequency GW emission (through forced PNS oscillations), the temporal structure of this signal component finds a natural explanation. Generally, episodes of strong SASI activity correlate with strong low-frequency GW activity. Large amplitudes of the shock oscillations are not sufficient, however; the determining factor is the kinetic energy contained in large-scale motions. For that reason, there is hardly any low-frequency emission component during the second SASI episode in model s27. During this phase, less mass is involved in SASI motions and the SASI amplitude is significantly smaller. The lack of large-scale motions with a significant $l = 2$ component also explains the weak low-frequency GW activity in model s11.2, where the post-shock flow is dominated by smaller convective bubbles and the kinetic energy in non-radial fluid motions is typically smaller than for the more massive progenitors.

5.3.8 Comparison of the exploding and non-exploding 20 solar mass models

The exploding model s20s differs only in details from its non-exploding counterpart during the accretion phase. After the onset of shock expansion strong low-frequency emission is sustained until the end of the simulation (see Fig. 5.11). This emission is connected to mass motions with a strong $l = 2$ component in layer A. In Fig. 5.14 we plot for models s20 and s20s,

$$\alpha_l = \sum_{m=-l}^l |\alpha_l^m(t)|^2 , (l = 1, 2), \quad (5.12)$$

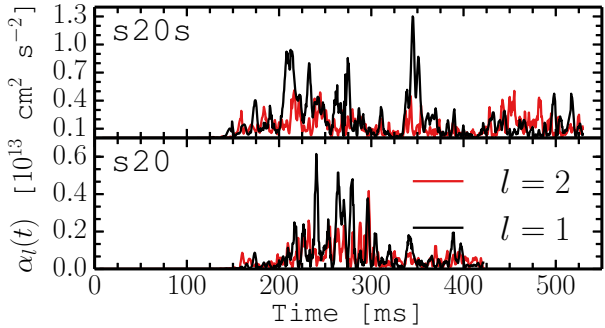


Figure 5.14: The $l = 2$ and $l = 1$ components of the radial velocity sampled in the unstable PNS layer for the $20M_\odot$ models. The radial velocity has been sampled at a radius R given by $\rho(R) = 9.5 \times 10^{13} \text{ g cm}^{-3}$. The top panel shows the exploding model s20s, and the bottom panel shows the non-exploding model s20, which was only calculated to 421 ms after core bounce.

with

$$\alpha_l^m(t) = \frac{(-1)^{|m|}}{\sqrt{4\pi(2l+1)}} \int v_r(\theta, \phi, t) Y_l^m d\Omega, \quad (5.13)$$

where v_r is the radial velocity at a radius R corresponding to an spherically averaged density of $\rho(R) = 9.5 \times 10^{13} \text{ g cm}^{-3}$.

In the exploding model, the $l = 2$ mode is generally stronger than in the non-exploding model and it remains strong throughout the simulation in contrast to the non-exploding model, where the $l = 2$ mode decreases in strength after the SASI-dominated phase ends. After a period of decreasing strength around 400 ms, the quadrupole mode in model s20s increases in strength and reaches amplitudes similar to those seen during the pre-explosion phase. At the same time, there is a shift in the relative strength of the $l = 1$ and $l = 2$ mode after the onset of shock expansion. While the quadrupole mode increases in strength, the dipole is relatively weak at late times. This transition into a flow pattern that is dominated by an $l = 2$ mode resonates better with the quadrupole nature of GW emission. We therefore see an increase in low-frequency emission from the unstable layer within the PNS. Such a change in the spectrum of eddy scales after shock revival could result from changes in the asymmetric accretion flow onto the PNS, or from changes in the stratification of entropy and electron fraction, but for the purpose of interpreting the GW emission, the ultimate reason is immaterial and left to more detailed future studies of the hydrodynamics of PNS convection. Aliasing of high-frequency emission may also be partly responsible for the enhanced low-frequency emission after shock revival. However, since the spectrograms in Fig. 5.3 show broadband emission, it is unlikely that the low-frequency emission we see after shock revival is caused by aliasing effects alone.

Table 5.1: Signal-to-noise ratio (SNR) for all four models. Values are given for two different frequency domains, 20...250 Hz (low-frequency) and 250...1200 Hz (high-frequency). The table shows values for two different detectors, AdvLIGO and the Einstein Telescope. For the latter we calculate the SNR for two different modes of operation (ET-B and ET-C). SNRs have been computed for a source at a distance of 10 kpc. For model s20s we only show the SNR for the low-frequency band since the high-frequency band is somewhat contaminated by aliasing effects. For s27, s20, and s11.2 we also give the ratio of the band-limited SNRs in the low- and high-frequency bands to quantify the “colour” of the GW signal.

	s27				s20				s20s	
	Low	High	Total	Low/High	Low	High	Total	Low/High	Low/High	Low
AdvLIGO	3.7	4.5	8.8	0.82	5.3	7.7	9.4	0.82	0.32	10.2
ET-C	50.0	64.0	81.3	0.78	73.9	109.3	131.9	0.83	0.36	139.7
ET-B	78.5	73.7	107.7	1.07	113.9	127.0	170.6	0.74	0.42	217.3

5.4 Detection Prospects

With the prominent high-frequency component of the signal in 2D largely muted in 3D, it is evidently necessary to reconsider the prospects of detecting a Galactic supernova. Detailed detectability studies based on 2D waveforms (Logue et al., 2012) may now well be too optimistic after the update of the waveform predictions. While an elaborate statistical machinery is required to reliably determine signal detectability and possible inferences about core-collapse supernova physics (Logue et al., 2012, Hayama et al., 2015), we can already draw some conclusions for the waveforms presented in this paper.

5.4.1 General Considerations

The detectability of the GW signal from a core-collapse supernova has often been assessed using the signal-to-noise ratio (SNR) for matched filtering. Assuming an optimally-orientated detector and a roughly isotropic frequency spectrum for different observer directions, the SNR for matched filtering is formally given by (Flanagan & Hughes, 1998, cp. their Eq. (5.2) for the second form),

$$(\text{SNR})^2 = 4 \int_0^\infty df \frac{|\tilde{h}(f)|^2}{S(f)} = \int_0^\infty df \frac{h_c^2}{f^2 S(f)}, \quad (5.14)$$

where

$$h_c = \sqrt{\frac{2G}{\pi^2 c^3 D^2} \frac{dE_{\text{GW}}}{df}} \quad (5.15)$$

is the characteristic strain, $S(f)$ is the power-spectral density of the detector noise as a function of frequency f , and dE_{GW}/df is the spectral energy density of the GWs. Note that

the second expression for the SNR in Eq. (5.14) has been obtained under the assumption of isotropic GW emission so that one can express the (formally) direction-dependent squared amplitudes in terms of the GW energy spectrum dE_{GW}/df .

Since the GW signal of a core-collapse supernova is, however, *not amenable to matched filtering* because of its stochastic character, the SNR formally defined by Eq. (5.14) must be interpreted with care.

The SNR still remains a useful quantity as it measures the excess power during the time of integration, as can be seen by re-expressing Eq. (5.14) in terms of the expectation value for the Fourier coefficients $\tilde{n}(f)$ of the noise over a finite time-interval Δt (the integration time for the signal), which obey (cp. Logue et al., 2012)

$$\langle \tilde{n}(f)\tilde{n}^*(f)\Delta f \rangle = S(f)/2, \quad (5.16)$$

where the factor 1/2 appears because $S(f)$ is defined as the one-sided power spectral density of the time-dependent strain noise $n(t)$. Note that the frequency spacing Δf is given by $\Delta f = 1/\Delta t$ and that Δt can be set to the length of the signal in consideration in our case. For a finite time series, where the integral in Eq. (5.14) can be replaced with a sum over the Fourier modes at discrete frequencies $f_k = k/\Delta t$ (with integer k), we then obtain,

$$(\text{SNR})^2 = 8 \sum_k \frac{|\tilde{h}(f_k)|^2 \Delta f}{\langle |\tilde{n}(f_k)|^2 \rangle \Delta f} = 8 \sum_k \frac{|\tilde{h}(f_k)|^2}{\langle |\tilde{n}(f_k)|^2 \rangle}. \quad (5.17)$$

For uncorrelated Gaussian noise in each frequency bin, the SNR of a prospective signal obtained from the summation over N_{bins} frequency bins is thus related to the χ^2 -value for this signal as

$$\chi^2 \sim N_{\text{bins}} + \text{SNR}^2/2, \quad (5.18)$$

where the additional term N_{bins} comes from the contribution of the noise in each bin. Sufficiently high values of χ during a prospective supernova event (with an integration interval Δt defined by a coincident neutrino signal)* can be attributed to a physical signal; e.g. to exclude stochastic fluctuations as a source of the excess power at a confidence level of 95%, one needs

$$\text{SNR}^2/8 = \chi^2 - N_{\text{bins}} \gtrsim 2.3\sqrt{N_{\text{bins}}} \quad (5.19)$$

for large N_{bins} . For a signal with power excess in a frequency band with bandwidth δf and $N_{\text{bins}} = \delta f/\Delta f = \delta f \Delta t$, this implies the requirement

$$\text{SNR} \gtrsim 4.3 (\delta f \Delta t)^{1/4}, \quad (5.20)$$

for a detection of a signal in this band. This roughly corresponds to the results obtained by Flanagan & Hughes (1998) for noise monitoring in Section IIB of their paper.

*This is crucial because it is always possible to find short intervals with power excess comparable to a physical signal if the integration time is sufficiently long.

Prior knowledge of the signal structure can help to identify signals with even lower SNR; Logue et al. (2012), for example, showed that a detection and identification can be possible already for $\text{SNR} \sim 10$ with the help of a principal component analysis of template waveforms provided that the signal structure is not too dissimilar from the template. This is in line with the weak dependence of Eq. (5.20) on the bandwidth δf .

If properly interpreted, the SNR thus remains a useful measure for the detectability of our predicted signals within the scope of this paper. Its inherent limitations provide justification for neglecting the effect of the detector orientation and the precise directional dependence of the signal by computing the SNR from the energy spectrum dE/df instead of a direction-dependent Fourier spectra of the strain. We have verified that the SNR for the low-frequency band does not vary by more than $\sim 20\%$, and the SNR for the high-frequency signal depends even less on the observer direction.

5.4.2 Detection Prospects for Simulated Models

We calculate the SNR from Eq. (5.14) for the zero-detuning-high power configuration of Advanced LIGO (LIGO Laboratory & Shoemaker, 2010) and the B (Hild et al., 2008) and C (Hild et al., 2010) configurations for the Einstein telescope. We refer to these configurations as AdvLIGO, ET-B and ET-C. In order to better assess the detectability and possible inferences from the signal structure, we compute SNRs quantifying the excess power in a low-frequency band (SNR_{low} for $20 \text{ Hz} \leq f < 250 \text{ Hz}$, i.e. $\delta f = 230 \text{ Hz}$) and a high-frequency band (SNR_{high} for $250 \text{ Hz} \leq f < 1200 \text{ Hz}$, i.e. $\delta f = 950 \text{ Hz}$). SNRs for all models in those two bands for events at a distance of 10 kpc are presented in Table 5.1. Using Eq. (5.20), we obtain a detection threshold of $\text{SNR}_{\text{low}} \gtrsim 11$ for the low-frequency band and $\text{SNR}_{\text{high}} \gtrsim 15$ for the high-frequency band assuming $\Delta t = 0.5 \text{ s}$. Since the critical SNR depends weakly on Δt , these fiducial values can be used for all models. SNRs for arbitrary distances can easily be obtained since the SNR is inversely proportional to the distance.

Regardless of the precise detector configuration, the SASI-dominated models s20 and s27 are clearly distinguished from the convective model s11.2 through a higher ratio $\text{SNR}_{\text{low}}/\text{SNR}_{\text{high}} > 0.65$ compared to $\text{SNR}_{\text{low}}/\text{SNR}_{\text{high}} < 0.42$. SASI-dominated models thus appear “redder” in GWs before the onset of the explosion. Based on our small sample, they also appear to be characterised by a higher SNR, but this might be incidental. More massive progenitors with stronger neutrino heating in the gain region, stronger cooling above the PNS convection, and a larger mass in the gain region could produce a stronger GW signal, even in the absence of strong SASI activity. The ratio $\text{SNR}_{\text{low}}/\text{SNR}_{\text{high}}$, on the other hand, should be a robust indicator for the presence or absence of large-scale SASI motions.

Note that since model s20s suffers most severely from aliasing effects, the SNR in the high-frequency domain might be inaccurate. We therefore refrain from giving values for SNR_{high}

and the total SNR. The low-frequency band, on the other hand, should be unaffected by aliasing artefacts and SNR_{low} is significantly higher than in the non-exploding models. It is possible that the enhanced low-frequency emission from the convectively unstable region of the PNS is a general feature in exploding models and we hypothesise that shock revival will be followed by GW emission with *excess power in the low-frequency band*. This is in contrast to previous studies in 2D (Murphy et al., 2009, Müller et al., 2013) where shock expansion is typically followed by an *increase in the high-frequency emission band*. If shock revival generally leads to enhanced low-frequency emission, this would obviously complicate the interpretation of a high value of $\text{SNR}_{\text{high}}/\text{SNR}_{\text{low}}$, which could *either* indicate SASI activity or the transition to an explosion.

5.4.3 Detection Prospects with AdvLIGO

For a supernova at a distance of 10 kpc, it is evident that *none* of the four models could be detected by AdvLIGO based on excess signal power. Given the reduction of the typical amplitudes by a factor of ~ 10 in 3D compared to 2D, this is not surprising. Using an approach based on simulated noise and a principal component analysis of the signal, Logue et al. (2012) and Gossan et al. (2016) already found that AdvLIGO is only marginally able to identify waveforms from 2D supernova simulations for events at distances of a few kpc.

For the SASI-dominated models (s20, s27, s20s), the excess power in the low-frequency band would become detectable at 95% confidence level at the distance of the Crab supernova (~ 2 kpc), as would the high-frequency component of model s20. Model s11.2, on the other hand, would not show a statistically significant power excess.

5.4.4 Detection Prospects with the Einstein Telescope

The situation will change drastically with the Einstein Telescope. For either configuration considered here, the excess power in both bands ought to be detectable for an event at a distance of 10 kpc, although the low-frequency component of model s11.2 would barely make it above the detection threshold for ET-C. The high SNR in both bands would permit a measurement of $\text{SNR}_{\text{low}}/\text{SNR}_{\text{high}}$ as an indicator for the GW “colour” with some confidence. Even at a distance of 20 kpc, the excess power in both the high- and low-frequency bands would still remain detectable and quantifiable in the SASI-dominated models. For the more modest goal of a mere detection, the SNR for model s20s would be high enough to observe events throughout the entire Milky Way and even out to the Large Magellanic Cloud (~ 50 kpc).

5.4.5 Interpretation of a Prospective Detection

Without a more sophisticated analysis of the time-frequency structure of a prospective detection event, only limited conclusions about the supernova core could be drawn from excess power measured by GW detectors during specific time windows. Nonetheless, a GW detection with the Einstein Telescope would be valuable for corroborating our understanding of hydrodynamic instabilities in the core in conjunction with the observed neutrino signal.

A high value of $\text{SNR}_{\text{low}}/\text{SNR}_{\text{high}}$ concurrent with a periodic modulation of the neutrino signal (Marek et al., 2009, Lund et al., 2010, Brandt et al., 2011, Tamborra et al., 2013, Müller & Janka, 2014, Tamborra et al., 2014a) would furnish solid evidence for SASI activity, and strong low-frequency emission concurrent with modulations of the neutrino signal below ~ 50 Hz would strongly indicate that shock revival is already underway during the time window in question. While these conclusions could likely be drawn on the basis of the neutrino signal alone for nearby supernovae with a suitable orientation of the SASI spiral plane or sloshing mode, the detection of modulations in the neutrino signal for non-optimal orientations becomes difficult at distances $\gtrsim 10$ kpc (Müller & Janka, 2014). In such cases, combining the GW and neutrino signal would likely allow stronger conclusions.

When SASI-induced modulations of the neutrino signal are not detectable due to distance, orientation, or unfavourable neutrino flavor oscillations, a detection of strong GW power in the low-frequency band would still provide evidence for *either* SASI activity (since this signal component is more robust against orientation effects than modulations of the neutrino signal) *or* the onset of strongly asymmetric accretion after shock revival. If the SNR is sufficiently high to localise the GW power excess in time relative to the onset of the neutrino signal (which roughly marks the time of bounce), it may be possible to decide between those two alternatives.

Late GW power excess after $\gtrsim 0.5$ s will likely indicate the onset of the explosion without prior SASI activity, since the SASI typically reaches non-linear saturation well before this point, and since the decreasing mass in the gain region does not allow for strong late-time GW emission due to the SASI (as shown by models s20 and s27).

5.5 Conclusions

We have studied the GW signal from the accretion phase and the early explosion phase of core-collapse supernovae based on four recent 3D multi-group neutrino hydrodynamics simulations. We considered four models based on three progenitors with ZAMS masses of $11.2 M_{\odot}$, $20 M_{\odot}$, and $27 M_{\odot}$. The three non-exploding models enabled us to study the phase between bounce and shock revival. We covered both the SASI-dominated regime (model

s20, Tamborra et al., 2014a; model s27, Hanke et al., 2013), as well as the convection-dominated regime (model s11.2, Tamborra et al., 2014b). Additionally, the exploding $20M_{\odot}$ model s20s (Melson et al., 2015b, with a modified axial-vector coupling constant for neutral current scattering) illustrates changes in the GW signal in exploding models. Since our treatment of the microphysics and the neutrino transport is on par with previous works on the GW signal from 2D simulations (Marek et al., 2009, Yakunin et al., 2010, Müller et al., 2013, Yakunin et al., 2015), we were in the position to conduct a meaningful comparison of GW emission in 2D and 3D during the accretion and explosion phase for the first time. To this end, we included the $27M_{\odot}$ 2D models of Müller et al. (2012c) and Hanke et al. (2013) in our study.

Our analysis showed differences between the GW emission in 2D and 3D. The prominent, relatively narrow-banded emission at high-frequencies that is characteristic of 2D models is significantly reduced. With the reduction of the high-frequency emission, distinctive broadband *low-frequency* emission in the range between 100 Hz and 200 Hz emerges as a characteristic feature during episodes of SASI activity and during the explosion phase of model s20s. The low-frequency emission does also exist in the 2D models, but it is completely overwhelmed by the high-frequency emission. This conclusion is somewhat model dependent, because in one of our 2D models, s27-2D, high-frequency GW emission is low and the low-frequency component becomes very prominent.

We discussed these differences extensively from two vantage points: On the one hand, we investigated the underlying hydrodynamic processes responsible for GW emission and showed how the changes in the GW signal in 3D are related to critical differences in flow dynamics in 3D compared to 2D. On the other hand, we outlined the repercussions of these changes for future GW observations and sketched possible inferences that could be drawn from the detection of a Galactic event by third-generation instruments.

With regard to the hydrodynamic processes responsible for GW emission, our findings can be summarised as follows:

1. There is a high-frequency signal component that closely traces the buoyancy frequency in the PNS surface region in 2D and 3D, i.e. the roughly isothermal atmosphere layer between the PNS convection zone and the gain region acts as frequency stabiliser for forced oscillatory motions in both cases. However, the high-frequency component mostly stems from aspherical mass motions in and close to the overshooting region of PNS convection in 3D, whereas it stems from mass motion close to the gain radius in 2D. This indicates that quasi-oscillatory mass motions at high frequencies are instigated *only by PNS convection in 3D* even during the pre-explosion phase, whereas forcing by the SASI and convection in the gain region is dominant in 2D. The resulting *amplitudes of the high-frequency component are considerably lower in 3D than in 2D*.
2. We ascribe the strong excitation of high-frequency surface g-mode oscillations in 2D to several causes: The inverse turbulent cascade in 2D leads to larger impact velocities

of the downflows and creates large flow structures that can effectively excite $l = 2$ oscillations that give rise to GW emission. Braking of downflows by the forward turbulent cascade and fragmentation into smaller eddies strongly suppress surface g-mode excitation in 3D. Moreover, the spectrum of turbulent motions does not extend to high frequencies in 3D both in SASI-dominated and convection-dominated models so that the resonant excitation of the $l = 2$ surface g-mode at its eigenfrequency becomes ineffective.

3. In 3D, low-frequency GW emission in the pre-explosion phase ultimately stems from the global modulation of the accretion flow by the SASI. Because of frequency doubling and/or the contribution from the $l = 2$ mode, the typical frequencies of this component are of the order of 100...200 Hz, i.e. somewhat higher than the typical frequency of the $l = 1$ modes of the SASI. Mass motions in the post-shock region, the PNS surface region and the PNS convection zone all contribute to this low-frequency component, which indicates that the modulation of the accretion flow is still felt deep below the gain radius as the accreted matter settles down onto the PNS. Moreover, our analysis of the detection prospects shows that *the low-frequency component of the signal at $\gtrsim 100$ Hz becomes a primary target in terms of detectability* in contrast to previous 2D results.
4. By contrast, convective models characterised by mass motions of intermediate- and small-scale like s11.2 show very little GW emission at low frequencies. The high-frequency emission, on the other hand, is excited primarily by PNS convection and is therefore less sensitive to the dominant instability (convection or SASI) in the post-shock region. *Thus, the ratio of high-frequency to low-frequency GW power can potentially be used to distinguish SASI- and convection-dominated models in the pre-explosion phase.*
5. However, strongly enhanced low-frequency emission can also occur due to a change of the preferred scale of the convective eddies in the PNS convection zone as exemplified by model s20s, where the dominant mode shifts from $l = 1$ to $l = 2$ late in the simulation. Since this does not occur in the corresponding non-exploding model s20, one can speculate that this behaviour is due to changes in the accretion flow and neutron star cooling associated with shock revival. If this behaviour is generic for exploding models enhanced GW emission may still remain a fingerprint of shock revival as it is in 2D (Murphy et al., 2009, Müller et al., 2013). With only one explosion model available to us, this conclusion does not rest on safe ground; more 3D explosion models are needed to check whether enhanced low-frequency GW emission after shock revival is indeed a generic phenomenon.

It is obviously of interest whether future GW observations will be able to discriminate between models with such distinctively different behaviour as the ones presented here. Without an elaborate statistical analysis, only limited conclusions can be drawn concerning this point. In this paper, we confined ourselves to rough estimates based on the expected excess

power in second- and third-generation GW detectors in two bands at low ($20 \dots 250$ Hz) and high ($250 \dots 1200$ Hz) frequency. Due to the reduction of the signal amplitudes compared to 3D, the prospects for second-generation detectors appear rather bleak; even the SASI-dominated models s20, s20s, and s27 could not be detected out further than ~ 2 kpc with AdvLIGO at a confidence level of 95%. Third-generation instruments like the Einstein Telescope, however, could not only detect all of our models at the typical distance of a Galactic supernova (~ 10 kpc) and strong GW emitters like s20s out to 50 kpc; the expected signal-to-noise ratios could even be high enough to distinguish models with enhanced low-frequency emission due to SASI from convective models based on the “colour” of the GW spectrum. In conjunction with timing information and the neutrino signal, it may also be possible to distinguish enhanced low-frequency emission from the SASI from enhanced GW emission after shock revival as in model s20s.

However, more work is obviously needed to fully exploit the potential of GWs as a probe of the supernova engine in the case of “ordinary”, slowly rotating supernovae for which PNS convection and the SASI are the dominant sources of GW emission. Desiderata for the future include a much broader range of 3D explosion models to determine to what extent the aforementioned features in the GW signal are generic. With waveforms from longer explosion simulations, the prospects for detecting a Galactic supernova in GWs with second generation instruments may also appear less bleak than they do now based on our biased selection that includes only one explosion model evolved to 200 ms after shock revival.

Furthermore, it is conceivable that much more information can be harvested from the GW signals than our simple analysis suggests. Several authors (Logue et al., 2012, Hayama et al., 2015, Gossan et al., 2016) have already demonstrated the usefulness of a powerful statistical machinery in assessing the detectability of supernovae in GWs and distinguishing different waveforms (e.g. from rotational collapse and hot-bubble convection, Logue et al., 2012). Peeling out the more subtle differences between SASI- and convection dominated models from GW signals in the face of greatly reduced signal amplitudes certainly presents a greater challenge, but third-generation instruments will nonetheless make it an effort worth undertaking.

The GW analysis presented in this work is based on three nonrotating progenitors. However, it is known that rotation can have an impact on the GW signal. In rapidly rotating models there is a strong GW burst associated with the rebound of the core (Müller, 1982). During the post-bounce phase rotation can lead to a bar-like deformation of the core (Rampp et al., 1998, Shibata & Sekiguchi, 2005) or the development of low-mode spiral instabilities (Ott et al., 2005, Kuroda et al., 2014, Takiwaki et al., 2016). These flow patterns in turn lead to strong GW emission at frequencies determined by the rotational frequency. In addition, rotation can modulate processes already present in nonrotating models, for example prompt convection or the SASI. In the models presented by Dimmelmeier et al. (2008) and Ott et al. (2012) only models with moderate rotation rates (and nonrotating models) exhibit prompt convection. The coupling between rotation and SASI activity can

lead to an enhanced growth rate of the spiral SASI mode (Blondin & Mezzacappa, 2007, Yamasaki & Foglizzo, 2008, Iwakami et al., 2009, Kazeroni et al., 2016, Janka et al., 2016). Whether a significant proportion of supernova progenitors have moderately rotating (let alone rapidly rotating) cores is unclear. Stellar evolution models that include the effects of magnetic fields predict rather slowly rotating pre-collapse cores (Heger et al., 2005). Furthermore, the angular momentum loss due to stellar winds seems to be underestimated by stellar evolution models, compared to results from asteroseismology (Cantiello et al., 2014). Predictions of the initial rotation rate of pulsars, based on their current spin-down rate and age, suggest that a large fraction of the pulsar population is born with rotation periods of the order of tens to hundreds of milliseconds (Popov & Turolla, 2012, Noutsos et al., 2013).

There is also the issue of starting the simulations from spherically symmetric progenitor models. It has been found that asymmetries in the burning shells of the progenitor can influence the shock dynamics and even help to ensure a successful explosion (Burrows & Hayes, 1996, Fryer et al., 2004, Arnett & Meakin, 2011, Couch & Ott, 2013, Müller & Janka, 2015). Any change in the initial conditions that leads to a significant change in the dynamics of the supernova core should be expected to impact the GW signal. Therefore, it will be important to keep improving the predicted GW signals, in hand with the improvement of core collapse models.

6 The effects of rotation

In this chapter we study the effects rotation have on the GW signal. We present three models based on the same progenitor, two rotating models and one non-rotating. This allows us to study how the signal GW is effected by rotation.

6.1 Supernova Models

We present the GW signal from three models based on the progenitor of Heger et al. (2005), which is a solar-metallicity star with a ZAMS mass of $15M_{\odot}$. The progenitor was developed, taking into account the effects of magnetic fields and rotation, from ZAMS to the onset of iron-core collapse. The inclusion of magnetic fields lead to an overall reduction of the final rotation rate of the iron core, compared to a star evolved without magnetic fields. The main difference between the three models is their rotation profiles. One of the models uses the profile of the progenitor (m15r), an other has a enhanced rotation profile (m15fr), in the last model the rotation rate has been set to zero throughout the star (m15nr) In Fig. 6.1 we show the rotation profiles of m15fr and m15r.

- **m15fr:** The rotation profile of model m15fr has, by hand, been set to a constant rotation rate of 0.5 rad/s throughout the inner core of the star. At a radius of 1731 km the rotation profile changes to a linearly decaying profile (Fig. 6.1). The model was simulated using the Yin-Yang grid, the two grid patches had an initial resolution of 400 cells, 56 cells and 144 cells in the radial, polar and azimuthal directions, respectively. This corresponds to a 2 degree angular resolution. After the initial shock expansion halts around 60 ms post bounce the average shock radius decreases slightly. Between $\sim 80 - 160$ ms post bounce the shock front is on average more or less stationary. The shock starts to expand roughly 160 ms after core bounce and soon after shock revival sets in. The average shock reaches 2000 km around ~ 330 ms after core bounce. In the time before shock revival, the post-shock flow is dominated by a strong spiral SASI mode. The SASI sets in around ~ 100 ms post bounce.
- **m15r:** The initial rotation profile of model m15r is exactly that of the progenitor (Heger et al., 2005), without any artificial changes made by hand. The rotation profile as a function of radius can be seen in Fig. 6.1. The model was simulated using the Yin-Yang grid, the two grid patches had an initial resolution of 400 cells,

56 cells and 144 cells in the radial, polar and azimuthal directions, respectively. This corresponds to a 2 degree angular resolution. For the first ~ 80 ms after bounce, the evolution of the average shock radius of model m15r closely resembles the one seen in model m15fr. However, around 100 ms the average shock radius starts to decrease. Unlike model m15fr, strong SASI activity does not develop in model m15r, the flow in the post-shock region is instead dominated by hot-bubble convection. There is, however, some low amplitude dipole deformation of the shock front (see Fig. ??). The average shock radius continue until ~ 200 ms post bounce when the Si-O shell interface falls through the shock. The decrease density in front of the shock leads to decreased ram pressure and a transient period of shock expansion. At ~ 240 ms post bounce the expansion subsides and the shock front once more begins to retreat, a trend which continues until the end of the simulation.

- **m15nr:** In model m15nr the initial rotation rate was set to zero at all radii. The model was simulated using the Yin-Yang grid, the two grid patches had an initial resolution of 400 cells, 28 cells and 72 cells in the radial, polar and azimuthal directions, respectively. Which means that model m15nr was simulated with an angular resolution that is two times coarser than the other two models (4 degrees). Initially the shock expands and reaches a local maximum around 60 ms after bounce, from this point the shock radius steadily decreases until the Si-O shell interface falls through the shock. The decreased accretion rate leads to a transient period of shock expansion, until the shock eventually starts to recede once more. Except for the fact that the average shock radius is generally larger in model m15nr, model m15nr is similar to model m15r in terms of the evolution of the average shock radius. However, unlike model m15r, model m15nr develops strong SASI activity. In this model the SASI activity is dominated by the sloshing mode. The mode develops around ~ 120 ms after core bounce and peaks around ~ 230 ms post bounce. After the peak in activity the SASI mode gradually decays towards the end of the simulation.

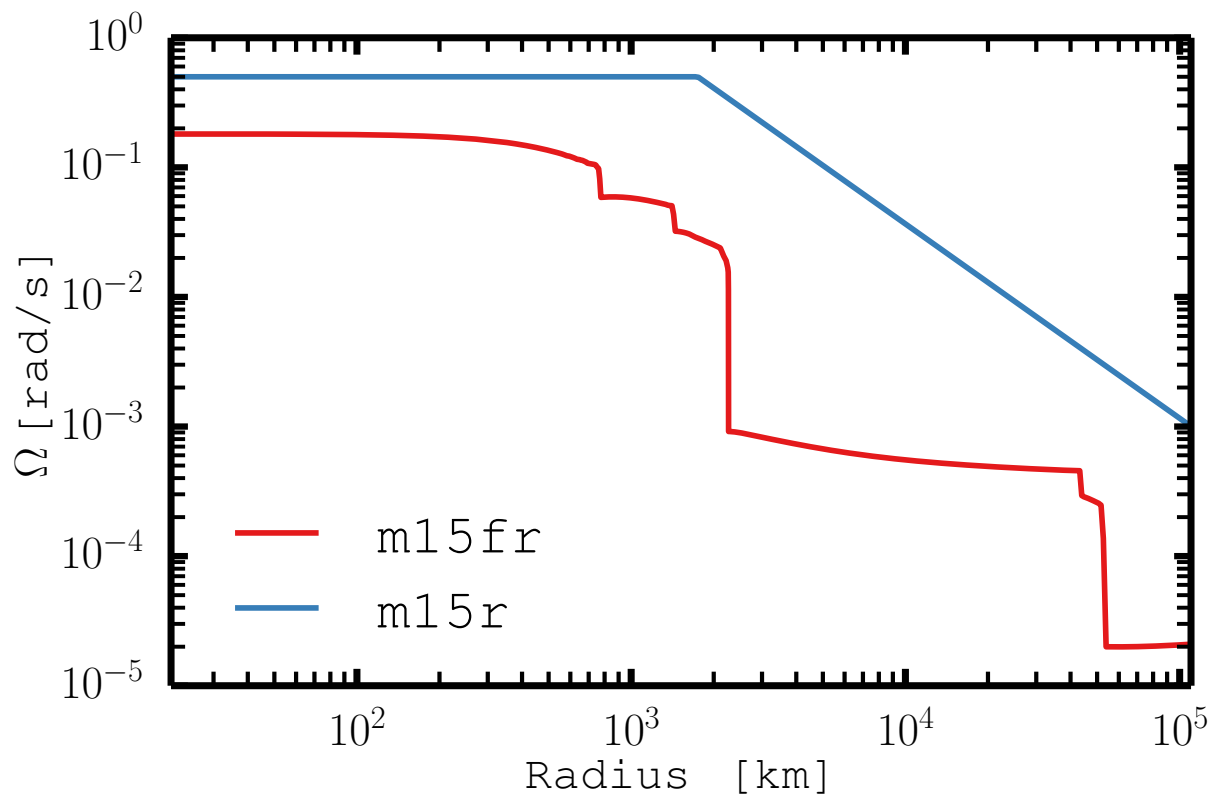


Figure 6.1: The radial rotation profiles for the two rotating models. The red line represents model m15fr and the blue line represents m15r.

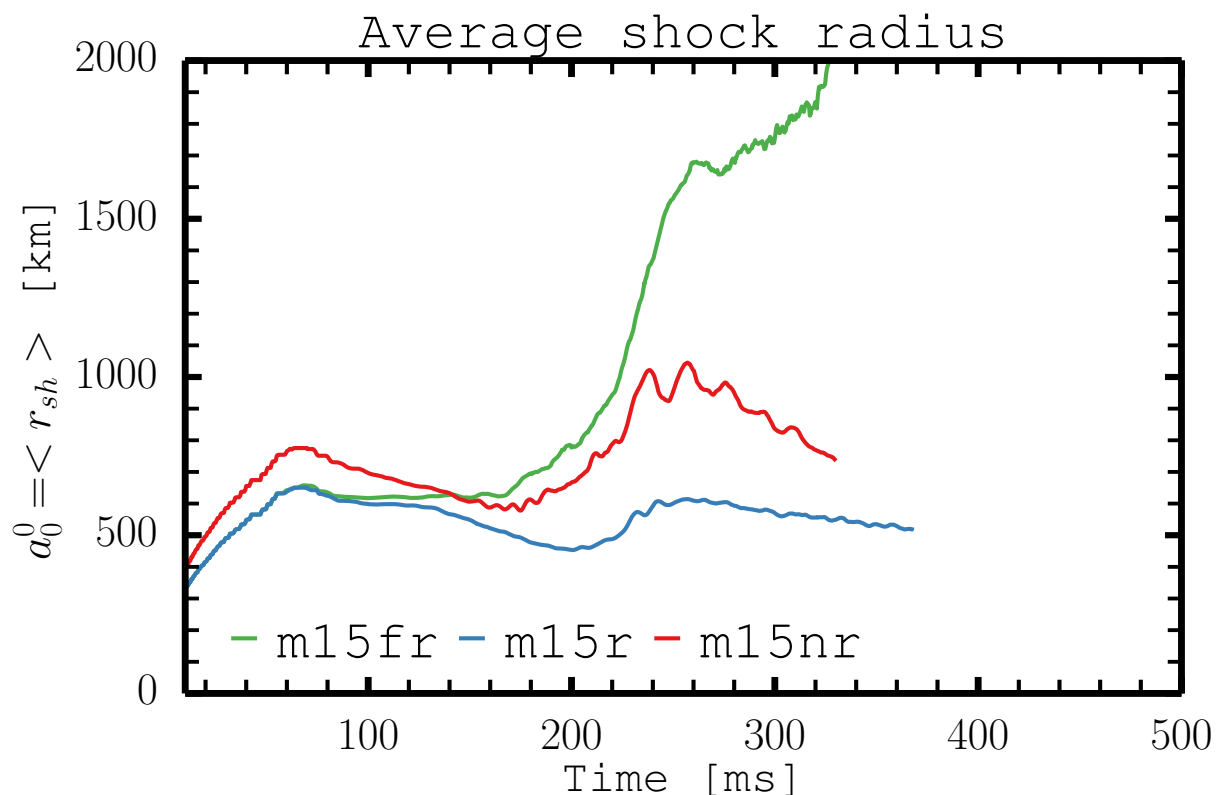


Figure 6.2: Average shock radius for model m15fr (green), m15r (blue), and m15nr (red) as a function of time after core bounce. The average shock radius is defined as the $(l, m) = (0, 0)$ expansion coefficient of the shock surface into spherical harmonics (Eq. 5.11).

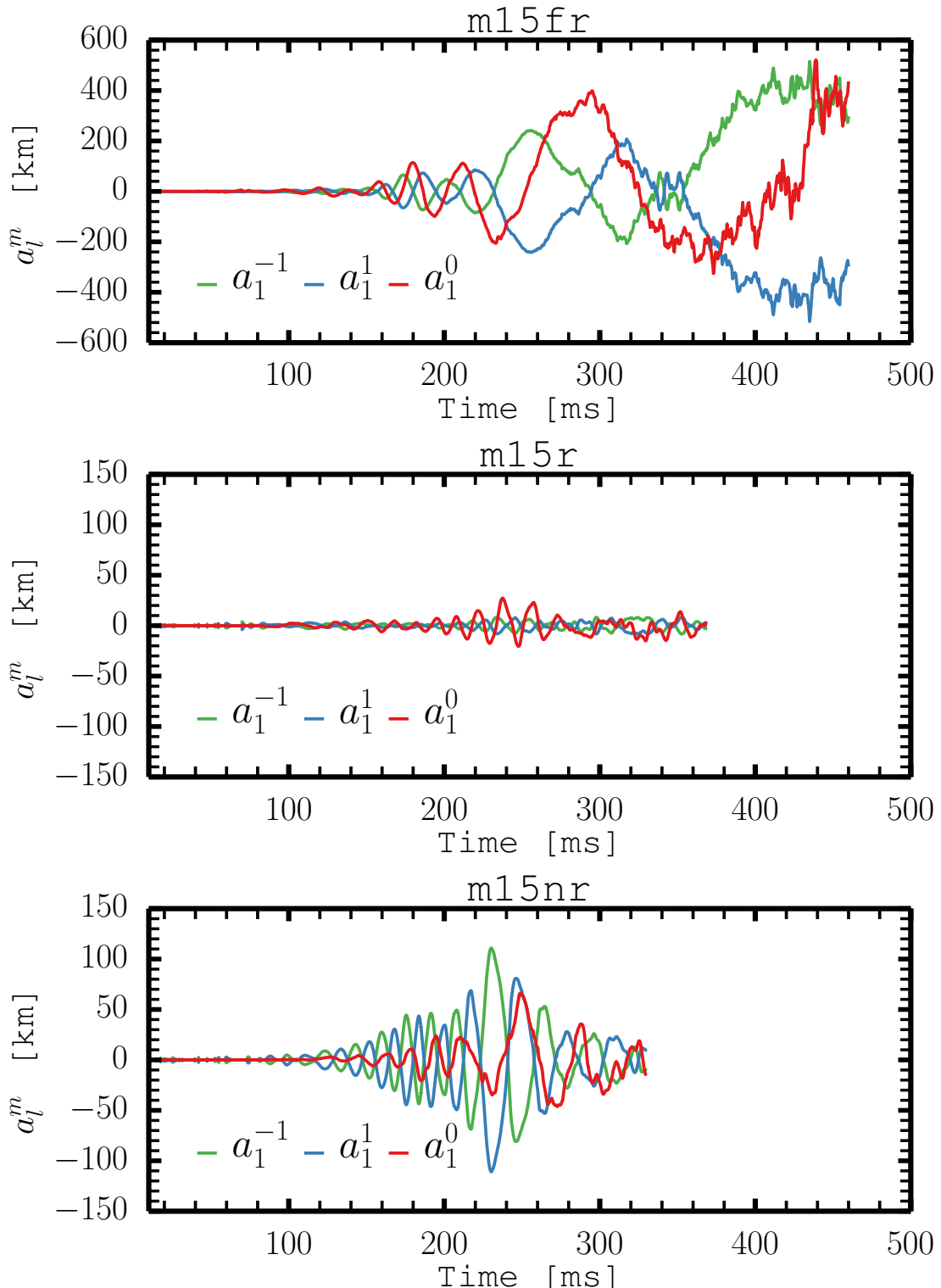


Figure 6.3: The $(l, m) = (1, 0)$, $(1, 1)$, and $(1, -1)$ coefficients of the decomposition of the shock surface into spherical harmonics as a function of time after bounce, see Eq. 5.11. From the top to bottom: Model m15fr, model m15r, and model m15nr.

6.2 Results

6.2.1 Qualitative description of the gravitational wave signals

The GW signals from the rotating models do not qualitatively differ significantly from the signals presented in chapter 5. In Fig. 6.4 we show the GW amplitudes generated by asymmetric mass motions for models m15fr, m15r and m15nr. The two columns shows the amplitudes for two different observer orientations, the right and left Colon represent observers situated along the x-axis (equator) and z-axis (pole) of the Yin grid-patch, respectively. The rows are order by progenitor, in order of decreasing initial rotation, and from the top shows m15fr, m1fr and m15nr. Vertical lines indicates episodes of strong SASI activity. The corresponding amplitude spectrograms (see Eq. 4.7) for a sliding window of 50 ms are shown in Fig. ???. The spectrograms show the sum of the squared Fourier components of the cross and plus polarisation modes, $\text{STFT}[A_+]^2 + \text{STFT}[A_\times]^2$. Before applying the DFT we convolve the signal with a Kaiser window with shape parameter $\beta = 2.5$. Frequencies below 50 Hz and above 1100 Hz are filtered out of the resulting spectrograms.

In all three models, an initial phase of quiescence is followed by a phase of rather stochastic emission, during with the typical amplitudes are on the order of a few cm. Model m15fr have the largest amplitude, of the three models, but at the same time the non-rotating model (m15nr) show larger amplitudes than the moderately rotating model (m15r). There seems to be no clear correlation between the strength initial rotation rate and the strength of the GW emission. The spectrograms (Fig. ?? show the familiar low-frequency and a high-frequency components that we saw in the four models presented in chapter 5.

During the SASI phase of m15fr, we see a low-frequency signal component in addition to the high-frequency stochastic component. Both strong low-frequency and high-frequency emission is visible in the upper row of Fig. 6.5. Both signal components are broader in model m15fr than in the other two models, to the point where the two components almost overlap. After the shock starts to expand the overall GW amplitudes are strongly reduced, but both low-frequency and high-frequency emission continues until the end of the simulation.

Of the three models, model m15r produces the weakest GW signal. The GW amplitudes never exceeds 1.5 cm, for both observer directions. Furthermore, the signal is strongly reduced in the time period between 180 and 250 ms post bounce. During this time high-frequency emission completely subsides and only very weak low-frequency emission is present in the signal. Around ~ 250 ms post bounce high-frequency emission sets in once more, at the same time the low-frequency emission ceases.

The non-rotating model (m15nr) is characterised by a relatively long initial quiescent phase, compared to the two rotating models. Low amplitude low-frequency GW emission set in around ~ 125 ms after bounce. The low-frequency signal component increases in strength

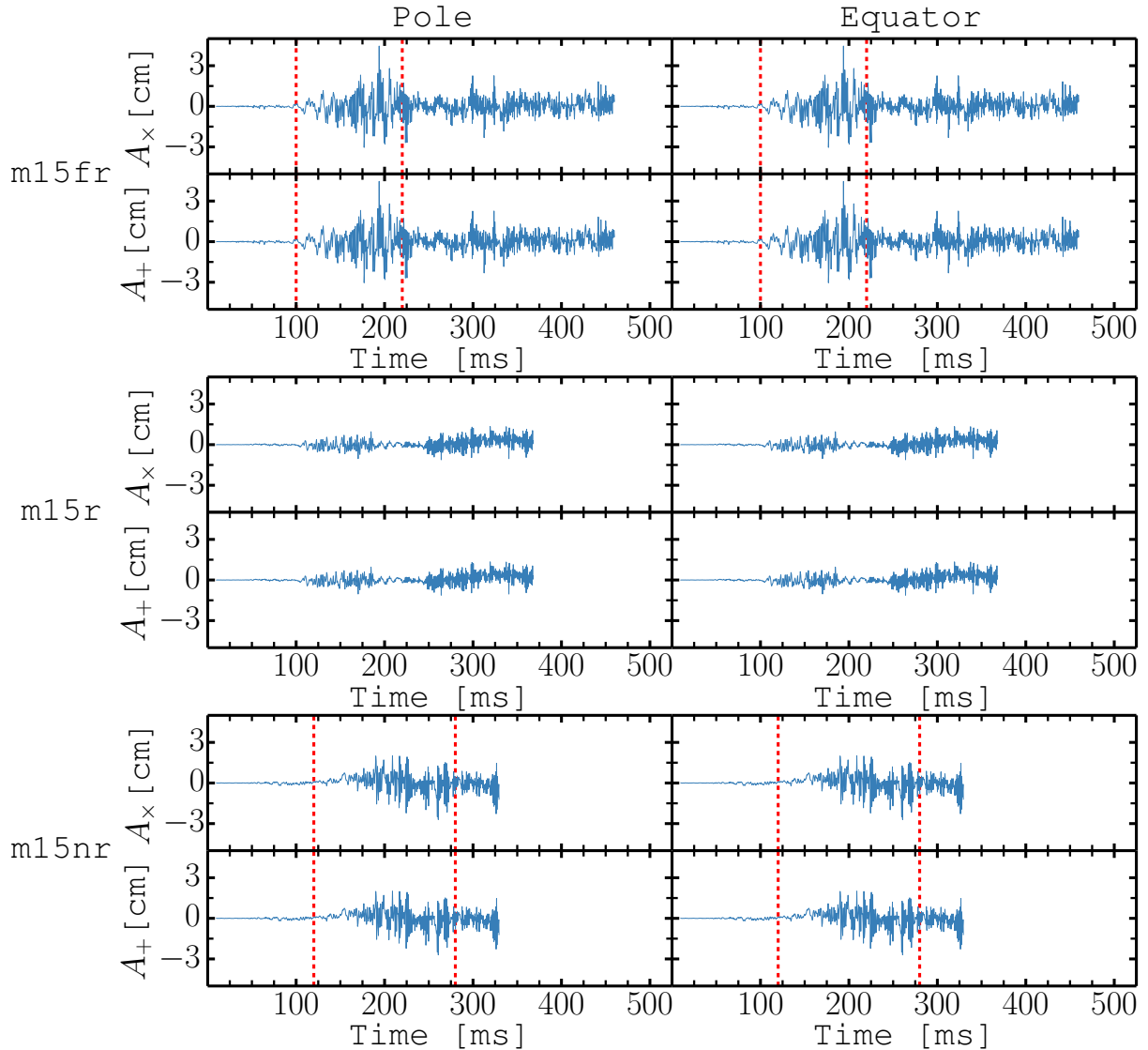


Figure 6.4: GW amplitudes A_+ and A_x as functions of time after core bounce. From the top: m15fr, m15r, and m15nr, respectively. The two columns show the amplitudes for two different viewing angles: an observer situated along the z -axis (pole; left) and an other observer along the x -axis (equator; right) of the Yin grid patch, respectively. Episodes of strong SASI activity occur between the vertical red lines.

until reaching a maximum around 175 ms after core bounce. Approximately 25 ms after the onset of low-frequency emission, high-frequency emission develops around ~ 150 ms after core bounce. After they developed, the two signal components persists, varying in strength, until the end of the simulation.

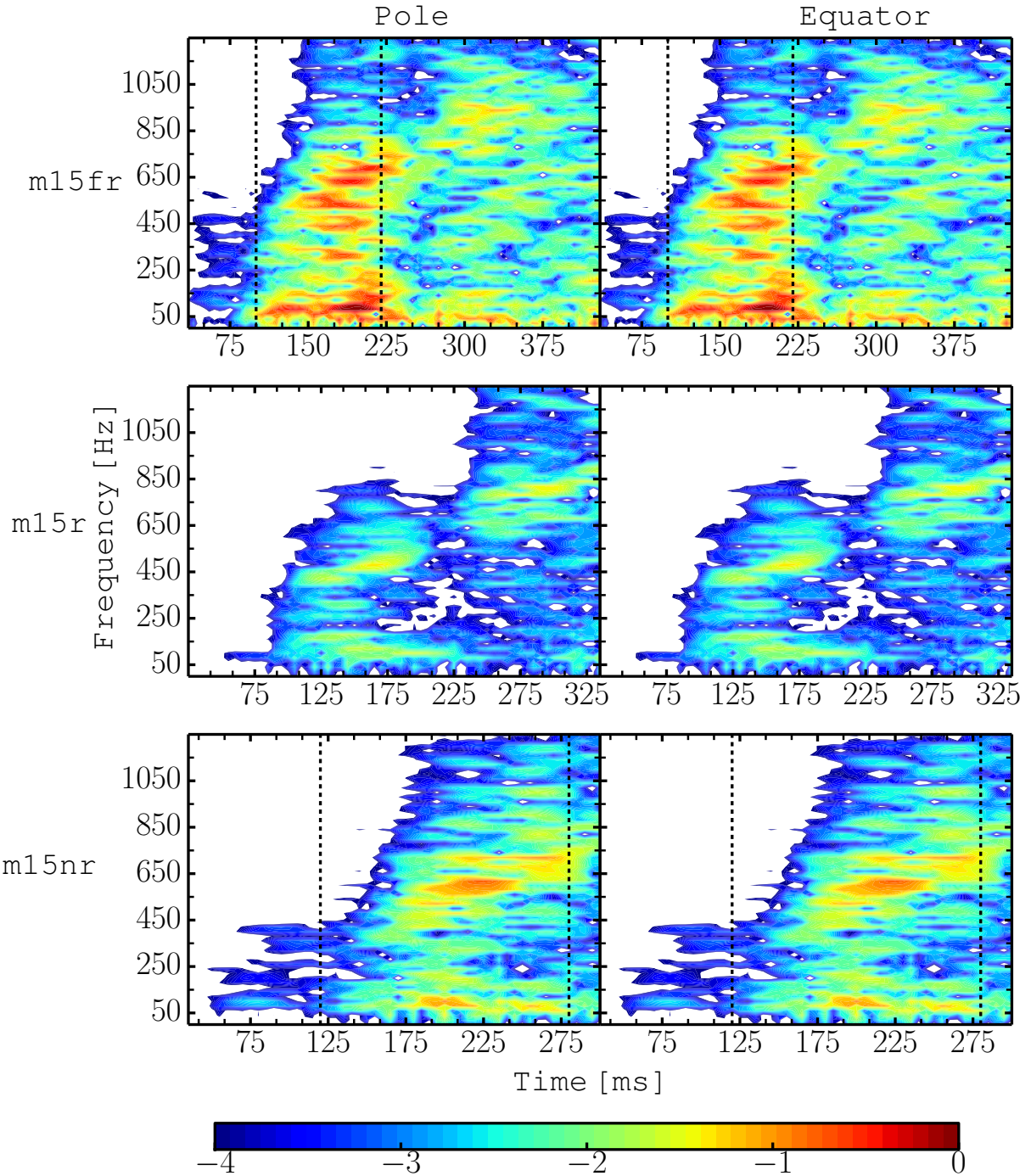


Figure 6.5: Amplitude spectrograms for a sliding window of 50 ms and two different observer directions, summed over the two polarisation modes ($|\tilde{A}_+|^2 + |\tilde{A}_\times|^2$). The different rows show the results for models m15fr, m1fr, and m15nr. (top to bottom). The two columns shows the spectrograms for two different viewing angles, the right and left column represent observers situated along the z-axis (pole) and x-axis (equator) of the Yin grid, respectively. The time is given in ms after core bounce. Vertical lines bracket SASI episodes. All panels have been normalised by the same global factor. The colour bar is given in a logarithmic scale.

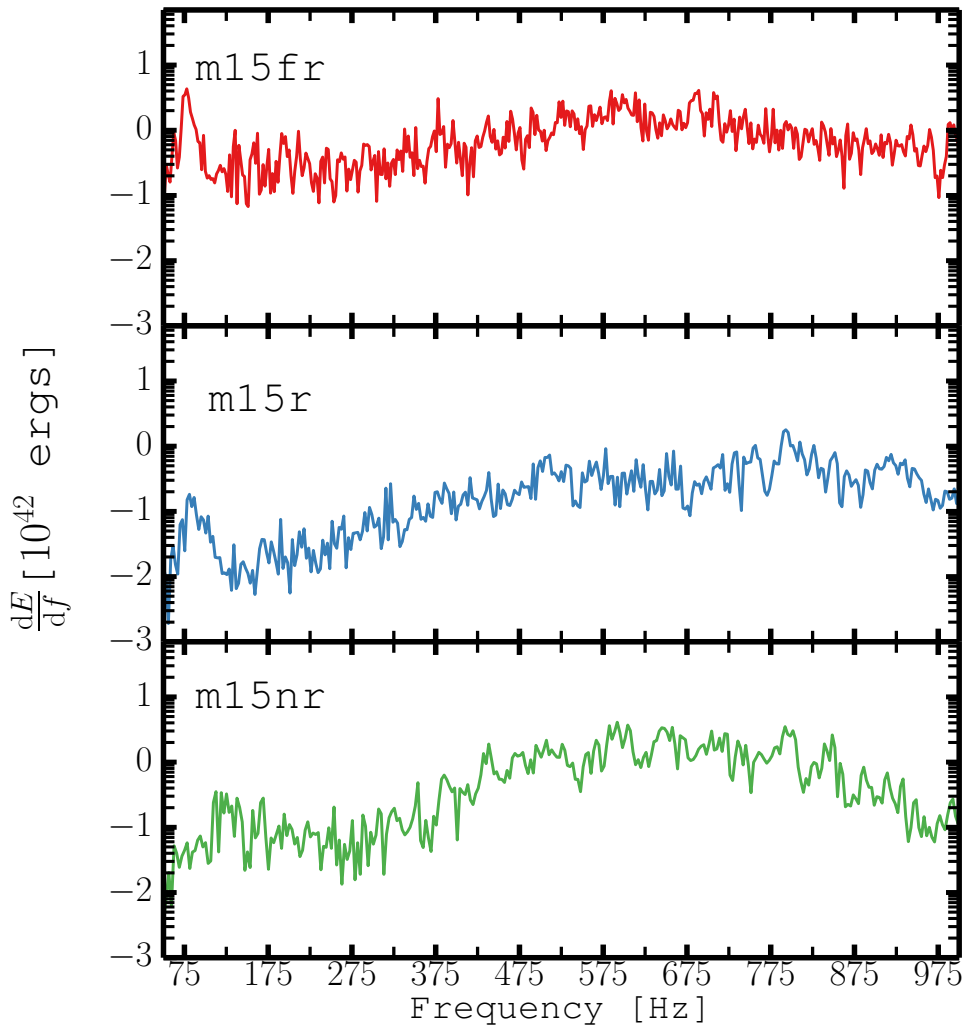


Figure 6.6: Time-integrated GW energy spectra dE/df for models m15fr, m15r, and m15nr (top to bottom). The spectra are computed from the Fourier transform of the entire waveform without applying a window function. The y-axis is given in a logarithmic scale.

Time-integrated energy spectra

Time-integrated energy spectra for each of the models are shown in Fig. 6.6. These are computed from the Cartesian components of the mass quadrupole tensor, according to Eq. 2.42 and .

Model m15fr shows a rather flat spectrum, with strong emission over a wide range of frequencies, but the model has a clear peak around $\sim 75 - 100$ Hz. The slower rotating model m15r, which does not develop strong SASI oscillations, emits much less energy at low frequencies. However, this model also exhibits a peak in the energy spectrum at frequencies

similar to $\sim 75 - 100$ Hz, but this peak is much weaker than the one seen in model m15fr. The energy spectrum of model m15nr is a hybrid between the spectrum of the two previous models. As model m15fr, there is a significant amount of energy radiated away by GWs below 300 Hz, but the spectrum is not as flat as the one of model m15fr.

6.3 Excitation of gravitational waves

In chapter 5 we studied the hydrodynamical instabilities responsible for GW emission in detail. We found that GWs are mainly excited in four ways. SASI activity leads to low-frequency by inducing an asymmetric mass distribution in the post-shock and by exciting forced non-resonant g-modes in the PNS. The forced g-modes are excited due to the SASI modulated accretion flow onto the PNS and their frequency is set by the SASI frequency. High-frequency emission is caused by the propagation of resonant g-modes in the PNS surface layer, the typical frequency of these oscillations is given by the Brunt-Väisälä-frequency in the PNS surface layer. Resonant g-modes are excited in two ways. Firstly, by downdrafts from the post-shock layer impinge the PNS surface. Strong downflows can be created by SASI activity and overturn of convective plumes. Resonant g-modes are also excited, in the PNS surface layer, as plumes from the unstable layer beneath overshoot into the surface layer. For the four models presented in chapter 5, we found that PNS convection was the main driver of this process and that downflows, while downflows from the post-shock layer provided a secondary and smaller contribution (with model dependent variations in relative importance of the two).

These conclusions hold true for the three models presented in this chapter as well, with one notable exception. In the two rotating models, model m15fr and model m15r, the GW signal generated by PNS convection is significantly reduced. When rotation is added to the simulations the PNS initially develops a positive angular momentum gradient in the PNS convection layer, which acts as a stabiliser and weakens PNS convection (Janka et al., 2001). The basic physical picture is that, when a buoyant plume propagates outwards its rotation rate is less than that of the surrounding medium and it, consequently, experiences a weaker centrifugal force. The effect of rotation is, therefore, to exact a force acting against the outwards propagation of the plume. Angular momentum transfer by convection will eventually flatten the rotation profile within the PNS and the stabilising effect provided by rotation will gradually decrease with time.

Based solely on the stabilising effects rotation have on PNS convection we would expect an overall reduction of high-frequency GW emission in the two rotating models. However, the picture is not so simple. We have to consider how well the Brunt-Väisälä-frequency in the PNS surface overlaps with the typical SASI and convective timescales. The compactness of the PNS tends to increase with progenitor mass, which results in a higher Brunt-Väisälä-frequency (Müller et al., 2013). SASI activity and neutrino driven convection in the post-shock layer operates at relatively long time-scales. Consequently, the

spectrum of the forcing and the natural g-mode frequency will overlap better in model based on a low mass progenitor, with a less compact PNS, than a more massive model. This is in fact reflected in the four models we study in chapter 5, the contribution to the high-frequency emission by convective plumes striking the PNS from above is relative high in model s11.2 (see Fig. 5.6).

We also have to consider the effects of the spiral SASI mode. The strong influence exerted by the spiral mode on the PNS, through a coherent large scale modulation of the accretion flow onto the PNS, not only effectively perturbs the surface, but can also reaches into the interior of the PNS and influence the convective layer of the PNS. A strong spiral SASI mode induces mass motions in the PNS at a set of different frequencies, which is reflected in the GW signal as “broadening” of both the low-frequency and high-frequency emission component. Model s27, which is dominated by the sloshing mode of the SASI, has a cleaner emission spectrum than for example the spiral SASI dominated model s20 (see Fig. ??). Cleaner, in the sense that the emission is concentrated in narrow bands. The same behavior is seen in model m15fr and model m15r. A particular strong spiral SASI mode develops in m15fr and this model emit GWs at a wider range of frequencies than model m15nr and model m15r. The reduction of high-frequency GW emission generated by PNS convection can clearly be seen in model m15r. Between 180 and 250 ms post bounce hot-bubble convection subsides and model m15r emits virtually no high-frequency GWs. The shock front reaches a minimum around 200 ms post bounce, after a 70 ms long period of recession (Fig. 6.2). The small average shock radius favours SASI activity over neutrino driven convection, and we see the development of low amplitude shock oscillations, see the middle panel of Fig. 6.3. Convection, on the other hand, is quenched. Fig. 6.7 shows the entropy per baryon of model m15r, in the xy-plane of the Yin-grid. The three panels show snapshots taken 167 (top left panel), 210 (top right panel), and 343 (bottom panel) ms after core bounce. The top left and the bottom panel show the typical hot bubbles that are characteristic of neutrino driven convection, but in the top right panel no such bubbles can be seen. The growth of low amplitude SASI activity and the suppression of convection in the post-shock layer is reflected in the GW signal as weak emission at low frequencies and a complete absence of the high-frequency signal component.

The reduction of GWs emitted from the PNS can also be seen in model m15fr. After the onset of shock revival the accretion rate onto the central object decreases and the violent downflows created by strong SASI activity ceases to exist. At the same time there is a strong reduction in the GW signal. This indicates that excitation of surface g-modes from above is the main source of high-frequency GW emission. This is in strong contrast to model s20s, where activity within the PNS increased after the onset of shock revival and consequently led to a strong increase of the GW signal.

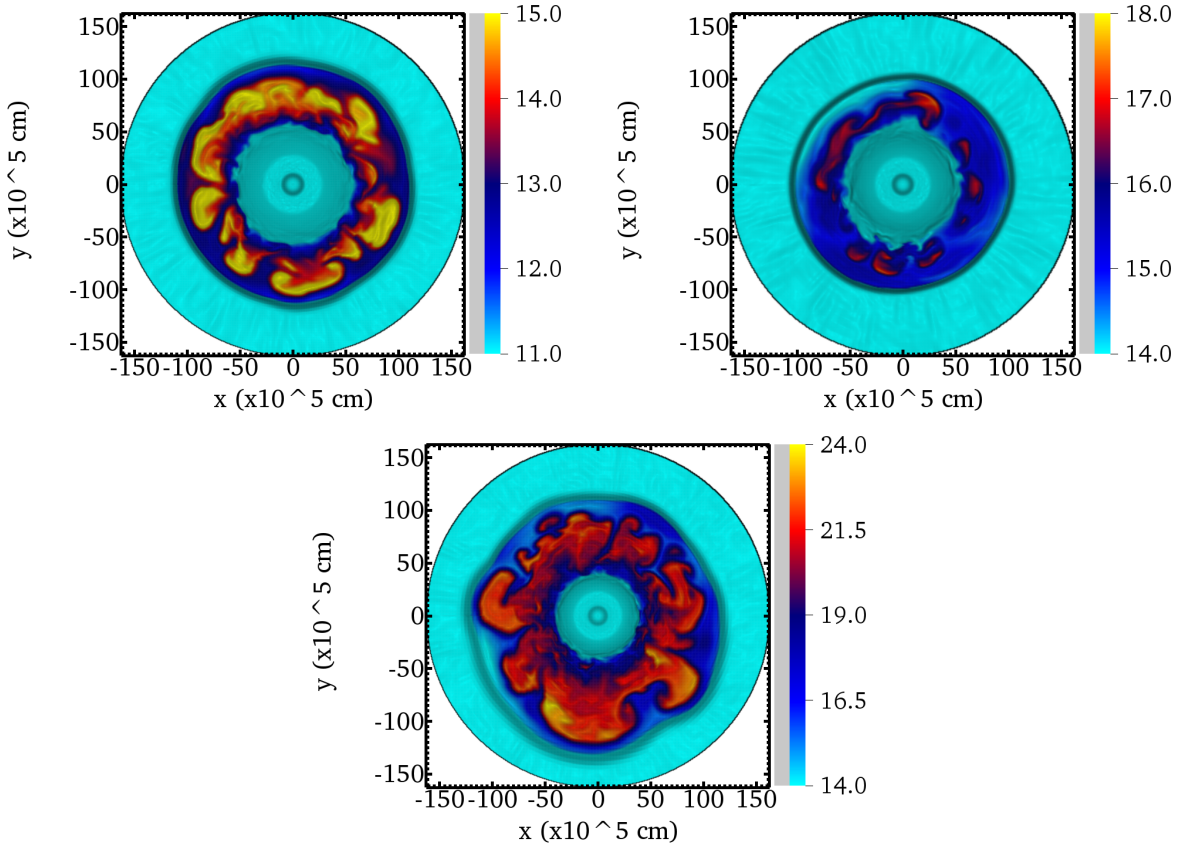


Figure 6.7: The entropy per baryon in the xy-plane of the Yin-grid for model m15r. Shown at 167 (top left panel), 210 (top right panel), and 343 (bottom panel) ms post bounce. The entropy is given in units of Boltzmann's constant k_b .

6.4 The standing accretion shock instability, rotation, and resolution

There is no clear connection between development of SASI activity and the progenitor's initial rotation rate, in the models we discuss in this chapter. Model m15r, in which the rotation profile is in accord with the stellar evolution calculations, does not develop strong SASI activity. In both model m15nr and model m15fr, however, a strong spiral SASI mode emerges.

Exactly how rotation influences the SASI growth rate and saturation does not seem to be a simple function of progenitor rotation rate. Recently Blondin et al. (2017) studied the effects of rotation by means of idealised hydrodynamic simulations of a standing accretion shock (in 2D and 3D). The results of Blondin et al. (2017) are in good agreement with the perturbative study of Yamasaki & Foglizzo (2008), which found that the linear growth rate of non-axisymmetric SASI modes is an increasing function of the progenitor rotation

rate. However, in the non-linear regime Kazeroni et al. (2017) does not find a monotonic connection between the rotation and the saturation amplitude of the SASI. In fact Fig.3 of Kazeroni et al. (2017) indicates that SASI activity may decrease with increasing rotation rate, at least at low to moderate rotation rates.

An additional complication comes from the fact that model m15nr was simulated with half the angular resolution of the other two models. Lower resolution has been found to favour the growth SASI activity, because energy accumulates at larger scales (Hanke et al., 2012). However, Abdikamalov et al. (2015) finds the opposite, and conclude that increasing the angular resolution reduces the SASI oscillations. They perform a set of general relativistic 3D hydrodynamic simulations of a $27 M_{\odot}$ progenitor with a neutrino leakage scheme to study the phase between bounce and shock revival.

Whether rotation suppresses the growth of SASI activity in model m15r or if SASI activity develops artificially in model m15nr because of insufficient angular resolution, the absence of strong SASI activity in model m15r reduces the over all strength of the GW signal.

6.5 Detection prospects

Following the procedure laid out in section 5.4, we calculate the possibility of detecting models m15fr, m15r, and m15nr. In order evaluate the possible of differentiating models with and without strong SASI activity (strong low-frequency emission) the GW signal, we compute SNRs in three frequency bands. The three bands are: the low-frequency band ($f \in [20, 250]$, $\delta f = 230$), the high-frequency band ($f \in [250, 1200]$, $\delta f = 950$), and the whole frequency range ($f \in [20, 1200]$, $\delta f = 230$). For the three bands we find, by inserting δf to Eq. 5.20 and assuming that the signal length $\Delta t \sim 0.5$, detection thresholds of $\text{SNR}_{\text{low}} \gtrsim 11$, $\text{SNR}_{\text{high}} \gtrsim 15$, $\text{SNR}_{\text{whole}} \gtrsim 20$ for the low-frequency band, the high-frequency band, and “whole-frequency” band, respectively. As in chapter 5, we calculate the SNR from Eq. (5.14) for the zero-detuning-high power configuration of Advanced LIGO (LIGO Laboratory & Shoemaker, 2010) and the B (Hild et al., 2008) and C (Hild et al., 2010) configurations for the Einstein telescope. These configurations are referred to as AdvLIGO, ET-B and ET-C.

In the low-frequency band the SNR of model m15fr is roughly equal to that of model s20s in the low-frequency band, for all the three detector configurations. The strong spiral SASI activity and the reduced high-frequency emission, due to dampening of PNS convection by rotation, leads to a high ratio between the SNR_{low} and SNR_{high} . Model m15r shows that one has to be careful when interpreting the ratio $\text{SNR}_{\text{low}}/\text{SNR}_{\text{high}}$. The reduction of the high-frequency emission and the presents of, due to intermediate and weak SASI activity, leads to ratios of $\text{SNR}_{\text{low}}/\text{SNR}_{\text{high}}$ which are $\sim 15 - 25$ higher than those of model m15nr, for all three detector configurations. However, model m15nr clearly develops much stronger SASI activity than model m15r.

Table 6.1: Signal-to-noise ratio for models m15fr, m15r, and m15nr. Values are given for two different frequency domains, 20...250 Hz (low-frequency), 250...1200 Hz (high-frequency), and for the whole frequency domain, 20...120. The table shows values for two different detectors, AdVLIGO and the Einstein Telescope. For the latter we calculate the SNR for two different modes of operation (ET-B and ET-C). The table show SNRs for a source at a distance of 10 kpc. The three tables show SNRs for model m15fr, model m15r, and model m15nr (from top to bottom).

m15fr	Low	High	Total	Low/High
AdVLIGO	10.8	4.9	11.9	2.20
ET-C	133.2	67.6	149.4	1.97
ET-B	224.6	83.5	239.6	2.69

m15r	Low	High	Total	Low/High
AdVLIGO	2.6	2.4	3.5	1.08
ET-C	32.2	34.4	47.1	0.93
ET-B	53.7	41.1	67.7	1.30

m15nr	Low	High	Total	Low/High
AdVLIGO	3.5	4.3	5.5	0.81
ET-C	46.5	59.3	75.2	0.78
ET-B	74.0	72.0	103.2	1.02

At a distance of 10 kpc, none of our models would be detectable with AdVLIGO. For the Einstein telescope the situation is significantly better. We estimate that model m15fr should be debatable out to distances of 75 kpc, while model m15nr and model m15r could be detected at ~ 20 kpc and ~ 30 kpc, respectively. The B configuration of the detector shows the most promise and can effectively increase those numbers by $\sim 35 - 60\%$.

6.6 Conclusion and discussion

In this chapter we studied progenitor rotation affects the GW signal of core collapse supernovae. We have not studied rapidly rotating models, but we have rather focus the regime of moderate progenitor rotation. Our main findings are:

1. Moderate rotation does not change the frequency structure of the GW signal, compared to the signal from non-rotating models. We see the familiar two-component structure with a high-frequency and a low-frequency signal component.
2. We find that the high-frequency emission instigate by PNS is weaker in the rotating models. This is because rotation has a stabilising effect on PNS convection and

decreases the amount kinetic energy in the convective layer of the PNS. This becomes particular apparent in model m15r, in this model we find a strong reduction of the GW amplitudes during a period of time when post-shock convection is weak. The generally weak amplitudes in this model reaffirms the fact that post-shock convection is a weak source of GW excitation, compared to PNS convection and SASI activity.

3. Of the three models presented in this chapter the fastest rotating model emits the strongest GW signal, this is because this model develops the strongest spiral SASI mode. Based on the models presented here one should not conclude that the strength of the signal will increase with increasing progenitor rotation rate. The conclusion should instead be that the stronger the spiral mode of the SASI is the larger the amplitudes of the GW signal are. However, it is not clear that stronger rotation leads to stronger SASI activity.
4. It should be emphasised that model m15r, where the rotation rate is exactly in accordance with the stellar evolution calculations of the $15 M_{\odot}$ progenitor these three models are based on, shows the weakest GW signal.
5. Unlike model s20s, the GW signal of model m15fr decreases after the onset of shock revival. This reduction is due to the small contribution to the total signal from mass motions instigated by PNS convection, which is reduced in strength due to rotation.

The GW signal from rapidly rotating models have been studied by several authors (Müller, 1982, Rampp et al., 1998, Shibata & Sekiguchi, 2005, Ott et al., 2005, Scheidegger et al., 2010, Kuroda et al., 2014, Takiwaki et al., 2016). A common feature of these studies is that they tend to predict rather strong emission of gravitational rotation. During the post-bounce phase rapid rotation can lead to the development of novel flow patterns that are not observed in slow/non-rotating models. Rampp et al. (1998) and Shibata & Sekiguchi (2005) found that very rapid rotation can lead to a bar-like deformation of the central core. In the somewhat slower rotating models of Ott et al. (2005), Kuroda et al. (2014), and Takiwaki et al. (2016) the development of a low-mode spiral instability was found. These asymmetric and rapidly rotating structures lead to strong GW emission.

Because of the strong and fairly monochromatic GW emission predicted by these models, it is predicted that such events should be detectable even at large distance. (Gossan et al., 2016) found that the most extreme case would be detectable with Advance-LIGO at a distance of over 3 Mpc. On the other, hand the models presented in this thesis would be with Advance-LIGO at distances of a few kpc. It is, however, not likely that a large part of the core collapse supernovae progenitors have rapidly rotating, or even moderately rotating, cores. Observations of pulsars put strong constraints on the rotation rate of core-collapse progenitors. It has been estimated that most pulsars are formed with rotation periods of a few tens to hundreds of milliseconds (Vranešević et al., 2004, Popov & Turolla, 2012, Noutsos et al., 2013). The recent study of Kazeroni et al. (2017) concludes that the one armed-spiral instability (Ott et al., 2005, Kuroda et al., 2014, Takiwaki et al., 2016) is not

able to spin down the PNS enough to make rapidly rotating progenitors compatible with the spin rate of young pulsars. Additionally stellar evolution models which includes the effects of magnetic fields predicts slowly rotating stellar cores (Heger et al., 2005). Recent results from asteroseismology Beck et al. (2012), Mosser et al. (2012) indicates that the cores low-mass red giants rotate slower than what was expected from stellar evolution (Cantiello et al., 2014, Deheuvels et al., 2014). According to results from asteroseismology, angular momentum loss due to stellar winds seems to be play a bigger role than they currently do in stellar evolution calculations (Cantiello et al., 2014).

The rotation rates of the two rotating models studied here is more along the lines of what is expected from state of the art stellar evolution calculations (Heger et al., 2005) and observations (Beck et al., 2012, Mosser et al., 2012, Popov & Turolla, 2012, Noutsos et al., 2013, Cantiello et al., 2014, Deheuvels et al., 2014). We find no qualitative difference between the GW signals from rotating models and we must conclude that a stochastic signal with amplitudes of few cm seems to be the generic 3D core collapse GW signal. This means that moderate to low progenitor rotation will not significantly increase the detectability of GWs from core-collapse supernovae. In fact, it might be that rotation decreases the signal strength and consequently make them harder to detect.

The fact model m15nr, the non-rotating model, has a angular resolution that is two times lower (four versus two degrees) than the two other models makes it difficult to draw strong conclusion about how low-frequency signal changes with increasing rotation. It might be that model m15nr develops an artificially strong spiral SASI mode due to the lower resolution, but it is also possible that rotation quenches the spiral mode in model m15r. Another weakness of the three models is that they all start from a from spherically symmetric progenitor models. It is not realistic to expect starts to be perfectly spherical symmetric objects. It has, in fact, been found that asymmetries in the burning shells of the progenitor can influence the shock dynamics and even help to ensure a successful explosion (Burrows & Hayes, 1996, Fryer et al., 2004, Arnett & Meakin, 2011, Couch & Ott, 2013, Müller & Janka, 2015). In a rotating progenitor such inhomogeneities could lead to a sizable emission of GWs during the collapse and right after core bounce. The long period of quiescence after bounce could be an artifact of the spherical symmetric progenitors.

Bibliography

- Abdikamalov E. B., Ott C. D., Rezzolla L., Dessart L., Dimmelmeier H., Marek A., Janka H.-T., 2010, Phys. Rev. D, 81, 044012
- Abdikamalov E., et al., 2015, ApJ, 808, 70
- Arnett W. D., Meakin C., 2011, ApJ, 733, 78
- Beck P. G., et al., 2012, Nature, 481, 55
- Bethe H. A., 1990, Rev.~Mod.~Phys., 62, 801
- Blanchet L., Damour T., Schaefer G., 1990, MNRAS, 242, 289
- Blondin J. M., Mezzacappa A., 2006, ApJ, 642, 401
- Blondin J. M., Mezzacappa A., 2007, Nature, 445, 58
- Blondin J. M., Shaw S., 2007, ApJ, 656, 366
- Blondin J. M., Mezzacappa A., DeMarino C., 2003, ApJ, 584, 971
- Blondin J. M., Gipson E., Harris S., Mezzacappa A., 2017, ApJ, 835, 170
- Brandt T. D., Burrows A., Ott C. D., Livne E., 2011, ApJ, 728, 8
- Buras R., Rampp M., Janka H.-T., Kifonidis K., 2006a, A&A, 447, 1049
- Buras R., Janka H.-T., Rampp M., Kifonidis K., 2006b, A&A, 457, 281
- Burrows A., 2013, Reviews of Modern Physics, 85, 245
- Burrows A., Hayes J., 1996, Physical Review Letters, 76, 352
- Burrows A., Hayes J., Fryxell B. A., 1995, ApJ, 450, 830
- Cantiello M., Mankovich C., Bildsten L., Christensen-Dalsgaard J., Paxton B., 2014, ApJ, 788, 93
- Cappellaro E., Turatto M., 2001, in Vanbeveren D., ed., Astrophysics and Space Science Library Vol. 264, The Influence of Binaries on Stellar Population Studies. p. 199 ([arXiv:astro-ph/0012455](https://arxiv.org/abs/astro-ph/0012455)), doi:10.1007/978-94-015-9723-4_16

- Chandrasekhar S., 1961, Hydrodynamic and Hydromagnetic Stability. Clarendon, Oxford
- Colella P., Woodward P. R., 1984, *J. Comp. Phys.*, 54, 174
- Colgate S. A., White R. H., 1966, *ApJ*, 143, 626
- Cordero-Carrión I., Cerdá-Durán P., Dimmelmeier H., Jaramillo J. L., Novak J., Gourgoulhon E., 2009, *Phys. Rev. D*, 79, 024017
- Couch S. M., Ott C. D., 2013, *ApJ*, 778, L7
- Couch S. M., Ott C. D., 2015, *ApJ*, 799, 5
- Deheuvels S., et al., 2014, *A&A*, 564, A27
- Dimmelmeier H., Font J. A., Müller E., 2002, *A&A*, 388, 917
- Dimmelmeier H., Novak J., Font J. A., Ibáñez J. M., Müller E., 2005, *Phys. Rev. D*, 71, 064023:1
- Dimmelmeier H., Ott C. D., Janka H.-T., Marek A., Müller E., 2007, *Phys. Rev. Lett.*, 98, 251101:1
- Dimmelmeier H., Ott C. D., Marek A., Janka H.-T., 2008, *Phys. Rev. D*, 78, 064056:1
- Dolence J. C., Burrows A., Murphy J. W., Nordhaus J., 2013, *ApJ*, 765, 110
- Einfeldt B., 1988, *SIAM J. Numer. Anal.*, 25, 294
- Epstein R., 1978, *ApJ*, 223, 1037
- Fernández R., 2010, *ApJ*, 725, 1563
- Fernández R., 2015, *MNRAS*, 452, 2071
- Finn L. S., 1989, in Evans C. R., Finn L. S., Hobill D. W., eds, Frontiers in Numerical Relativity. Cambridge University Press, Cambridge (UK), pp 126–145
- Flanagan É. É., Hughes S. A., 1998, *Phys. Rev. D*, 57, 4535
- Foglizzo T., Scheck L., Janka H.-T., 2006, *ApJ*, 652, 1436
- Foglizzo T., Galletti P., Scheck L., Janka H.-T., 2007, *ApJ*, 654, 1006
- Foglizzo T., et al., 2015, *PASA*, 32, 9
- Fryer C. L., Holz D. E., Hughes S. A., 2004, *ApJ*, 609, 288
- Fryxell B., Arnett D., Müller E., 1991, *ApJ*, 367, 619

- Goldreich P., Kumar P., 1990, ApJ, 363, 694
- Gossan S. E., Sutton P., Stuver A., Zanolin M., Gill K., Ott C. D., 2016, Phys. Rev. D, 93, 042002
- Guilet J., Foglizzo T., 2012, MNRAS, 421, 546
- Hamacher D. W., 2014, Journal of Astronomical History and Heritage, 17, 161
- Hanke F., 2014, PhD thesis, Technische Universität München
- Hanke F., Marek A., Müller B., Janka H.-T., 2012, ApJ, 755, 138
- Hanke F., Müller B., Wongwathanarat A., Marek A., Janka H.-T., 2013, ApJ, 770, 66
- Hayama K., Kuroda T., Kotake K., Takiwaki T., 2015, Phys. Rev. D, 92, 122001
- Heger A., Woosley S. E., Spruit H. C., 2005, ApJ, 626, 350
- Herant M., Benz W., Hix W. R., Fryer C. L., Colgate S. A., 1994, ApJ, 435, 339
- Hild S., Chelkowski S., Freise A., 2008, preprint, ([arXiv:0810.0604](https://arxiv.org/abs/0810.0604))
- Hild S., Chelkowski S., Freise A., Franc J., Morgado N., Flaminio R., DeSalvo R., 2010, Classical and Quantum Gravity, 27, 015003
- Ho P. Y., 1962, Vistas in Astronomy, 5, 127
- Hoyle F., Fowler W. A., 1960, ApJ, 132, 565
- Iwakami W., Kotake K., Ohnishi N., Yamada S., Sawada K., 2008, ApJ, 678, 1207
- Iwakami W., Kotake K., Ohnishi N., Yamada S., Sawada K., 2009, ApJ, 700, 232
- Janka H.-T., 1999, ,
- Janka H.-T., 2012, Annual Review of Nuclear and Particle Science, 62, 407
- Janka H.-T., Müller E., 1996, A&A, 306, 167
- Janka H.-T., Kifonidis K., Rampp M., 2001, in Blaschke D., Glendenning N. K., Sedrakian A., eds, Lecture Notes in Physics, Berlin Springer Verlag Vol. 578, Physics of Neutron Star Interiors. p. 363 ([arXiv:astro-ph/0103015](https://arxiv.org/abs/astro-ph/0103015))
- Janka H.-T., Melson T., Summa A., 2016, preprint, ([arXiv:1602.05576](https://arxiv.org/abs/1602.05576))
- Kageyama A., Sato T., 2004, Geochemistry, Geophysics, Geosystems, 5, n/a
- Kazeroni R., Guilet J., Foglizzo T., 2016, MNRAS, 456, 126

- Kazeroni R., Guilet J., Foglizzo T., 2017, preprint, ([arXiv:1701.07029](https://arxiv.org/abs/1701.07029))
- Kifonidis K., Plewa T., Janka H.-T., Müller E., 2003, A&A, 408, 621
- Kotake K., Iwakami W., Ohnishi N., Yamada S., 2009, ApJ, 697, L133
- Kotake K., Iwakami-Nakano W., Ohnishi N., 2011, ApJ, 736, 124
- Kraichnan R. H., 1967, Physics of Fluids, 10, 1417
- Kuroda T., Takiwaki T., Kotake K., 2014, Phys. Rev. D, 89, 044011
- Kuroda T., Kotake K., Takiwaki T., 2016, ArXiv e-prints, 1605.09215,
- LIGO Laboratory Shoemaker D., 2010, Advanced LIGO anticipated sensitivity curves,
<https://dcc.ligo.org/LIGO-T0900288/public>
- Lattimer J. M., Swesty F. D., 1991, *Nucl. Phys. A*, 535, 331
- Lecoanet D., Quataert E., 2013, MNRAS, 430, 2363
- Lentz E. J., et al., 2015, ApJ, 807, L31
- Liebendörfer M., Whitehouse S. C., Fischer T., 2009, ApJ, 698, 1174
- Logue J., Ott C. D., Heng I. S., Kalmus P., Scargill J. H. C., 2012, Phys. Rev. D, 86, 044023
- Lund T., Marek A., Lunardini C., Janka H., Raffelt G., 2010, Phys. Rev. D, 82, 063007
- Marek A., Dimmelmeier H., Janka H.-T., Müller E., Buras R., 2006, A&A, 445, 273
- Marek A., Janka H., Müller E., 2009, A&A, 496, 475
- Melson T., 2016, PhD thesis, Technische Universität München
- Melson T., Janka H.-T., Marek A., 2015a, ApJ, 801, L24
- Melson T., Janka H.-T., Bollig R., Hanke F., Marek A., Müller B., 2015b, ApJ, 808, L42
- Minkowski R., 1941, PASP, 53, 224
- Mosser B., et al., 2012, A&A, 548, A10
- Müller E., 1982, A&A, 114, 53
- Müller B., 2015, MNRAS, 453, 287
- Müller E., Janka H.-T., 1997, A&A, 317, 140
- Müller B., Janka H.-T., 2014, ApJ, 788, 82

- Müller B., Janka H.-T., 2015, MNRAS, 448, 2141
- Müller E., Fryxell B., Arnett D., 1991, A&A, 251, 505
- Müller B., Janka H., Dimmelmeier H., 2010, ApJS, 189, 104
- Müller E., Janka H.-T., Wongwathanarat A., 2012a, A&A, 537, A63
- Müller B., Janka H.-T., Marek A., 2012b, ApJ, 756, 84
- Müller B., Janka H.-T., Heger A., 2012c, ApJ, 761, 72
- Müller B., Janka H.-T., Marek A., 2013, ApJ, 766, 43
- Murphy J. W., Burrows A., 2008a, ApJS, 179, 209
- Murphy J. W., Burrows A., 2008b, ApJ, 688, 1159
- Murphy J. W., Ott C. D., Burrows A., 2009, ApJ, 707, 1173
- Murphy J. W., Dolence J. C., Burrows A., 2013, ApJ, 771, 52
- Nakamura T., Oohara K., 1989, in Evans, C. R., Finn, L. S., & Hobill, D. W. ed., Frontiers in Numerical Relativity. Cambridge University Press, pp 254–280
- Nordhaus J., Brandt T. D., Burrows A., Almgren A., 2012, MNRAS, 423, 1805
- Nordlund Å., Stein R. F., Asplund M., 2009, Living Reviews in Solar Physics, 6, 2
- Noutsos A., Schnitzeler D. H. F. M., Keane E. F., Kramer M., Johnston S., 2013, MNRAS, 430, 2281
- Ohnishi N., Kotake K., Yamada S., 2006, ApJ, 641, 1018
- Ohnishi N., Iwakami W., Kotake K., Yamada S., Fujioka S., Takabe H., 2008, Journal of Physics Conference Series, 112, 042018
- Oohara K.-i., Nakamura T., Shibata M., 1997, Progress of Theoretical Physics Supplement, 128, 183
- Ott C. D., Ou S., Tohline J. E., Burrows A., 2005, ApJ, 625, L119
- Ott C. D., Dimmelmeier H., Marek A., Janka H.-T., Hawke I., Zink B., Schnetter E., 2007, Phys. Rev. Lett., 98, 261101:1
- Ott C. D., et al., 2012, Phys. Rev. D, 86, 024026
- Plewa T., Müller E., 1999, A&A, 342, 179
- Popov S. B., Turolla R., 2012, Ap&SS, 341, 457

- Quirk J. J., 1994, *Int. J. Num. Meth. in Fluids*, 18, 555
- Rampp M., Janka H.-T., 2002, A&A, 396, 361
- Rampp M., Müller E., Ruffert M., 1998, A&A, 332, 969
- Roberts L. F., Ott C. D., Haas R., O'Connor E. P., Diener P., Schnetter E., 2016, preprint, ([arXiv:1604.07848](https://arxiv.org/abs/1604.07848))
- Sathyaprakash B., et al., 2012, Classical and Quantum Gravity, 29, 124013
- Scheck L., Kifonidis K., Janka H.-T., Müller E., 2006, A&A, 457, 963
- Scheck L., Janka H.-T., Foglizzo T., Kifonidis K., 2008, A&A, 477, 931
- Scheidegger S., Fischer T., Whitehouse S. C., Liebendörfer M., 2008, A&A, 490, 231
- Scheidegger S., Whitehouse S. C., Käppeli R., Liebendörfer M., 2010, Classical and Quantum Gravity, 27, 114101
- Shen C. S., 1969, Nature, 221, 1039
- Shibata M., Sekiguchi Y.-I., 2005, Phys. Rev. D, 71, 024014:1
- Strang G., 1968, SIAM Journal on Numerical Analysis, 5, 506
- Summa A., 2017, In preparation, Private communication
- Takiwaki T., Kotake K., Suwa Y., 2012, ApJ, 749, 98
- Takiwaki T., Kotake K., Suwa Y., 2014, ApJ, 786, 83
- Takiwaki T., Kotake K., Suwa Y., 2016, MNRAS, 461, L112
- Tamborra I., Hanke F., Müller B., Janka H.-T., Raffelt G., 2013, Physical Review Letters, 111, 121104
- Tamborra I., Raffelt G., Hanke F., Janka H.-T., Müller B., 2014a, Phys. Rev. D, 90, 045032
- Tamborra I., Hanke F., Janka H.-T., Müller B., Raffelt G. G., Marek A., 2014b, ApJ, 792, 96
- The LIGO Scientific Collaboration et al., 2015, Classical and Quantum Gravity, 32, 074001
- Thompson C., 2000, ApJ, 534, 915
- Viallet M., Meakin C., Arnett D., Mocák M., 2013, ApJ, 769, 1
- Vranesevic N., et al., 2004, ApJ, 617, L139

- Wilson J. R., 1985, in Centrella J. M., Leblanc J. M., Bowers R. L., eds, Numerical Astrophysics. pp 422–434
- Wongwathanarat A., Hammer N. J., Müller E., 2010a, A&A, 514, A48
- Wongwathanarat A., Janka H., Müller E., 2010b, ApJ, 725, L106
- Wongwathanarat A., Janka H.-T., Müller E., 2013, A&A, 552, A126
- Wongwathanarat A., Müller E., Janka H.-T., 2015, A&A, 577, A48
- Woosley S. E., Heger A., 2007, Phys. Rep., 442, 269
- Woosley S. E., Heger A., Weaver T. A., 2002, *Rev. Mod. Phys.*, 74, 1015
- Yakunin K. N., et al., 2010, Classical and Quantum Gravity, 27, 194005
- Yakunin K. N., et al., 2015, Phys. Rev. D, 92, 084040
- Yamasaki T., Foglizzo T., 2008, ApJ, 679, 607

